Directional Solidification Experiments with the Transparent Model Alloy Neopentyl Glycol-35wt.%(D)Camphor

Trinity College Dublin
Coláiste na Tríonóide, Baile Átha Cliath
The University of Dublin

A thesis submitted to
the Department of Mechanical & Manufacturing Engineering
Trinity College Dublin, the University of Dublin
in partial fulfilment of the requirements for the degree of

Doctor of Philosophy

by

TURLOUGH HUGHES

Supervisors:
Dr. Anthony J. Robinson
Dr. Shaun McFadden

October, 2021

Declaration of Authorship

I declare that this thesis has not been submitted as an exercise for a degree at this or any other university and it is entirely my own work.

I agree to deposit this thesis in the University's open access institutional repository or allow the library to do so on my behalf, subject to Irish Copyright Legislation and Trinity College Library conditions of use and acknowledgement.

I consent to the examiner retaining a copy of the thesis beyond the examining period, should they so wish (EU GDPR May 2018).

Signed: *Turlough Hughes*

Abstract

This thesis describes the development of an experimental facility in combination with image processing and computer vision techniques for the visualisation and characterisation of dendritic growth structures in the transparent model alloy Neopentyl Glycol-35wt.%(D)Camphor. The facility enables the control of the mushy zone growth rate and the imposed temperature gradient during solidification and provides in-situ optical video data of the solidification process. A suite of image processing and computer-vision techniques facilitate quantitative data extraction from the in-situ video data. The first is a front-tracking technique for automated tracking of the solidification front position and growth rates during directional solidification. The technique is validated against manual measurement and compared with the traditional liquidus isotherm speed measurement technique, which is widely used for estimating growth rates in directional solidification. Next, the development of a computer vision algorithm for multiple dendrite tip tracking is described. In combination with a thermally calibrated experimental facility, the tracker provides tip velocity and undercooling data for comparison with similar data obtained in microgravity. The data are compared to the traditional LGK model, and a modified LGK model adapted with a finite diffusional boundary layer theory to account for convection effects. Finally, mechanisms of competitive growth are investigated in the $\langle 111 \rangle$ transparent alloy. Multiple scenarios that obey and disobey the classical Walton-Chalmers rule are described and provide the first examples of competitive crystal growth with associated tip velocity vectors in directionally solidified $\langle 111 \rangle$ crystals.

Publications and Conferences

Journal publications

- T. Hughes, S. McFadden, A.J. Robinson, "A front-tracking measurement technique for in-situ columnar and equiaxed structure growth with controlled solidification," *Meas. Sci. Technol.*, vol. 32, no. 4, p. 045903, 2020.

- T. Hughes, A.J. Robinson, S. McFadden, "Multiple Dendrite Tip Tracking for In-Situ Directional Solidification: Experiments and Comparisons to Theory," *Mater. Today Commun.*, vol. 29, p. 102807, 2021.

- T. Hughes, A.J. Robinson, S. McFadden, "Competitive Growth during Directional Solidification of ⟨111⟩ Columnar Dendrites," *Under Preparation*

Conference papers

- T. Hughes, S. McFadden, A.J. Robinson, "In-situ observation of the effects of gravity direction on directional solidification of the transparent alloy NPG-35wt%-DC," in: A. Roósz, Z. Veres, M. Svéda, G. Karacs (Eds.), *Solidif. Gravity VII.*, Hal, Miskolc-Lillafüred, Ungarn, 2018: pp. 63–68. https://hal.archives-ouvertes.fr/hal-02342140.

- T. Hughes, S. McFadden, A. Robinson, A Controlled, "Low Temperature Experimental Setup to Investigate Casting Microstructures Using Transparent Materials and In-Situ Observation," *34th International Manufacturing Conference*, Sligo IT, August 2017.

Acknowledgements

Thank you to my supervisor, Dr Anthony J. Robinson, and co-supervisor, Dr Shaun McFadden, for your continued support and mentorship. I have learned so much from you both, and I will be eternally grateful for your time and patience in helping me to develop.

Thank you to the European Space Agency and the Irish Space Delegation at Enterprise Ireland for funding this research under the CETSOL-6 programme and through ESA PRODEX. I would also like to thank Dr Laszlo Sturz and Dr Gerhard Zimmermann for offering your expertise and opinion upon request. Thank you, Mr Gerry Byrne and Mr Mick Reilly, who were always available to discuss, plan and organise any changes to my experimental setup. Thank you also to Dr Robin Mooney for your advice in the early days. Thank you Dr. Tim Persoons for kindly sharing your equipment.

Thank you to my friends in the office for regular discussions and interest. Thank you to Mr Richard Ruggieri for inspiring me to take to the water again. Thank you to my close friends who have been there throughout the years, and to my friends in the Tara building who brought much-needed diversity during the final months. Thank you to Caelum, you have been incredible.

Finally, thank you to Mam and Dad and my family for your continued support and love.

Contents

List of Figures

List of Tables

Chapter 1

Introduction

1.1 Background and Context

Solidification is a critical processing route for many materials, particularly for metals and alloys. The micro-macro structures and textures that form during solidification both depend on the solidification process and strongly influence the solidified part's material properties. Approximately 113 million tonnes of metal is cast in over 45000 foundries worldwide each year [1]. In consumer electronics, solidification techniques such as the Czochralski method and zone refining are essential for manufacturing semiconductor grade silicon. For the gas-turbine engine, Bridgman solidified single crystal turbine blades have facilitated elevated operating temperatures and higher fuel efficiencies. In the automotive industry, casting is essential for the economical manufacturing of complex metal geometries such as engine blocks. It follows that the science of solidification, specifically metal solidification, is critical to modern civilisation.

Dendrites are the most regularly observed microstructure feature during metal solidification. From lightweight aluminium alloys to high-temperature nickel-base superalloys, their importance is demonstrated by the fact that every second, approximately 10^{10} metal dendrites are produced globally [2]. The word dendrite derives from the Greek word "$\delta\acute{\epsilon}\nu\rho\delta o\nu$" for "tree", owing to their tree-like, ramified structure. A dendrite grows with a single primary arm, and secondary dendrite arms regularly form behind the primary tip. If secondary dendrite arms grow unobstructed, tertiary dendrite arms may also grow behind the secondary dendrite tip, with successful tertiary

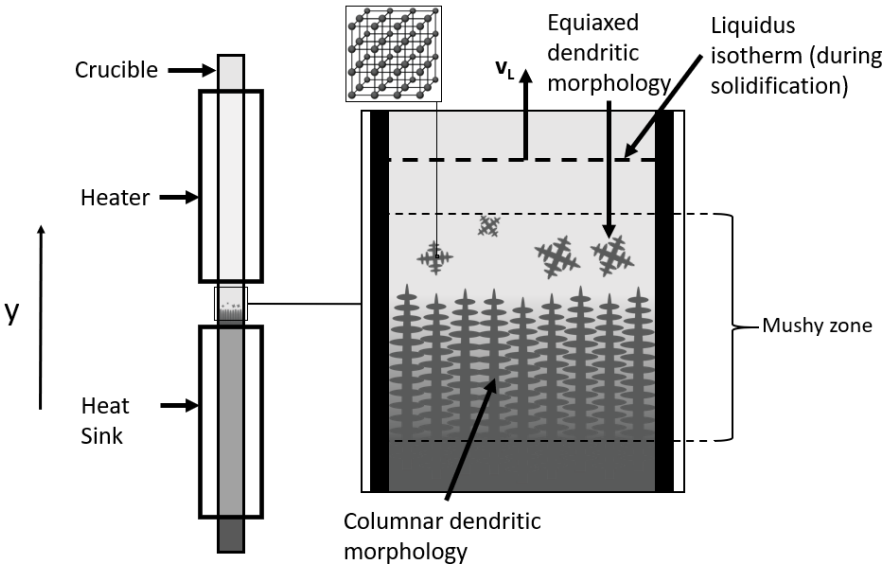

Figure 1.1: Schematic illustration of directional solidification setup showing mushy zone, isotherm speed, and columnar and equiaxed morphologies.

arms typically growing in the same direction as the primary dendrite arm. Consequentially, a single crystal growing in the melt may comprise a colony of dendrites from a single initial nucleus. Hence, the dendrite features (e.g. primary and secondary dendrite arms spacing, average grain size) and the competition between neighbouring crystals produce a diverse range of patterns. Experiments to study the mechanisms and physics of pattern formation during solidification are both crucial for validating theoretical and numerical solidification models and for advancing related technologies such as casting, welding, and additive manufacturing.

1.1.1 Directional Solidification

Controlled directional solidification experiments are routinely employed to study the effect that thermal processing parameters (e.g. temperature gradient, cooling rate, or isotherm speed) have on the micro – macro structure features that form during solidification. Directional solidification may occur due to an imposed or naturally occurring temperature gradient in the liquid melt at the macro-scale and causes preferential growth in the direction opposite to the heat flux direction. Temperature gradients frequently occur in casting, welding, and metal 3D printing due to a temperature difference between the molten liquid metal and the ambient environment. Thus, directional solidification is pertinent to many industrial scenarios.

Figure 1.1 schematically illustrates an experimental setup for directional solidification. Here, a heater and heat sink maintains a temperature difference along the vertical y-direction of a crucible containing the alloy (or metal). The heat sink is set below the alloy's solidus temperature, while the heater is set above the alloy's liquidus temperature. Before directional solidification, the heater and heat sink temperatures are maintained such that material in the crucible's heater and heat sink zones are in fully liquid and fully solid states, respectively. Additionally, as figure 1.1 shows, the binary alloy forms a region called the mushy zone, where solid and liquid coexist. If enough time is provided, the top of the mushy zone aligns with the liquidus isotherm.

At this point, the methods to initiate directional solidification vary. One approach is the Bridgman-Stockbarger technique [3], which involves translating the crucible vertically downwards through the heater and heat sink, causing the liquidus isotherm to advance vertically upwards along the crucible's y-axis. Following an initial transient, the growth rate and liquidus isotherm speed, v_L, match the pulling rate (assuming a constant pulling rate), and directional solidification occurs upwards along the crucible's positive y-direction. In this scenario, thermocouples in the heater and heat sink provide an estimate of the temperature gradient during solidification. Another approach to initiate directional solidification is simultaneously cooling the heater and heat sink, causing the liquidus isotherm to advance directionally upwards through the crucible. If the cooling rates are maintained (and following an initial transient), the growth rate and liquidus isotherm speed eventually match. Here, the liquidus isotherm speed, and hence the growth rate, are provided by $v_L = \dot{T}/G$, where $\dot{T}$ is the cooling rate, and G is the temperature gradient. One advantage of the second approach is that, with a stationary crucible, thermocouples may be inserted in fixed positions on the crucible wall and provide local temperature gradient measurements.

As noted, two crystal morphologies arise in dendritic solidification termed equiaxed and columnar crystals. Figure 1.2 shows how solidification processing parameters of growth rate and temperature gradient typically influence the solidification process, leading to different grain textures in the solid (see also reviews [4–6]). The different textures (and hence the different processing conditions) influence the material proper-

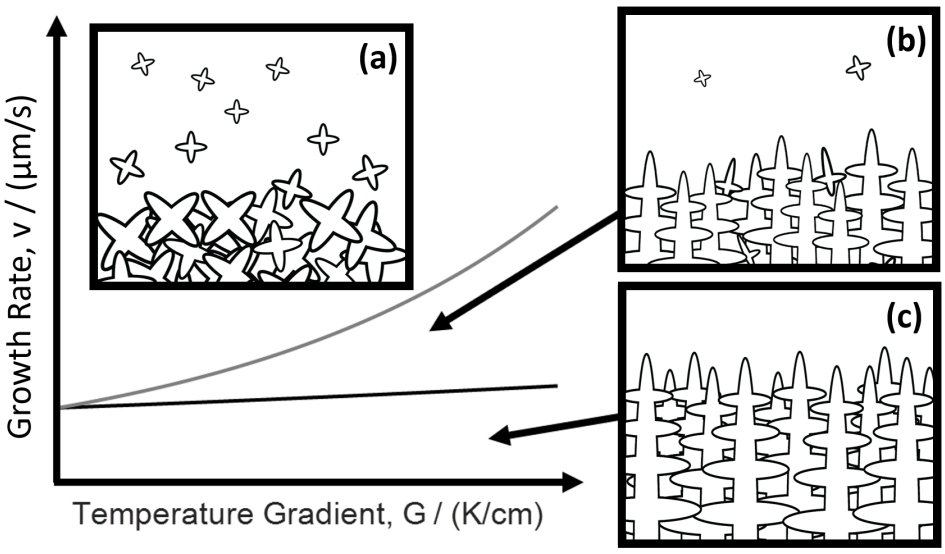

Figure 1.2: Hunt map showing the classical dendritic textures that arise due to different solidification processing conditions; (a) fully equiaxed growth (b) mixed columnar and equiaxed growth and (c) fully columnar growth.

ties of solidified materials. For example, a fine equiaxed texture consists of small randomly oriented equiaxed grains, resulting in isotropic material properties and higher yield strength [7, 8]. A columnar texture comprises elongated grains with a preferred orientation [3, 9, 10], resulting in anisotropic material properties. In this scenario, grain boundaries tend to align parallel to the preferred growth direction and result in improved creep resistance along the solidification direction [11]. The improved creep resistance is particularly beneficial for components of gas-turbine assemblies, which operate under high temperature and axial stress.

1.1.2 In-situ Solidification Research Methods

Due to metals' opaque nature, it was not possible to make an experimental observation of solidification mechanisms such as nucleation, growth and impingement of crystalline grains. Traditionally, solidification research consisted of experiments with controlled solidification processing parameters, followed by *post-mortem* metallographic analysis, i.e. the sectioning, polishing, and viewing of a sample under a microscope after the solidification process has occurred. While this approach has been invaluable, it provides only a single frame of the solidification process. Before the 1960s (with the exception of Papapetrou [12]), in-situ solidification studies were uncommon. One approach is using organic transparent crystalline materials that freeze like metals [13]. In 1965 Jackson

and Hunt proposed the use of transparent crystalline materials that form dendritic structures as analogues for metal solidification [13]. The materials are appropriately referred to as transparent analogues, or transparent model alloys. Figure 1.3 shows an example of in-situ optical micrographs of the solidification process in the transparent analogue material Neopentyl Glycol-35wt.%(D)Camphor. Experiments with transparent alloys have provided essential validation criteria for numerical and theoretical models [14–19] and important insights in mechanisms of solidification, such as fragmentation [20], primary dendrite arm spacing [21,22], and competitive growth [23].

In-situ observation of the solidification process is also possible in metallic systems using x-ray radiographic and tomographic imaging [24–29]. Early work by Mathiesen et al. [30], using x-ray radiography on Al-20wt.%Cu, showed the fragmentation phenomenon during directional solidification. Later, Ruvalcaba et al., [31] showed that local solute-enrichment at tertiary roots causes fragmentation in the same alloy composition. Fragmentation mechanisms have been studied in metallic systems with pulsed ultrasonic [32] and electromagnetic fields [33]. X-ray imaging techniques have been used to observe the CET [34–37], showing also the formation of elongated equiaxed grains [35, 36]. In-situ x-ray tomography provide 3D reconstructions of dendrites and has been used to study grain coarsening mechanisms [38, 39].

X-ray radiography has typically been conducted on thin rectangular geometries (≈100 μm to 200 μm thickness), where sufficient absorption contrast could be achieved between the solid and the liquid melt. However, thin sample thicknesses can affect the dendrite growth and microstructure. Bergeon et al. showed that sample thicknesses comparable to the primary dendrite arm spacing (e.g. 50 μm to 200 μm) alters the dendrite tip geometry and restricts secondary side branching to 2D [40]. Glicksman et al. showed that proximity to the crucible wall, as compared with the thermal diffusion length, alters the dendrite tip kinetics [41, 42]. Hence, bulk solidification experiments are required for validating theoretical models. The latest generation of x-ray radiographic imaging now facilitates in-situ observations in metallic systems on sample thicknesses up to ≈ 1mm, which is less than the typical thermal diffusion length in metallic alloys. On the other hand, experiments with transparent model alloys

facilitate sample thicknesses on the order of centimeters with negligible wall effects. They provide a low-temperature and inexpensive way to study dendritic solidification. Additionally, thermocouples can easily be placed inside the crucible of bulk samples for temperature measurement and thermal characterisation of the sample material's domain. Internal temperature measurements add confidence to temperature-related experimental results (e.g. dendrite tip temperature measurement) and provide useful criteria for numerical model validation.

1.1.3 Image Processing and Computer-Vision Techniques

Experiments with transparent alloys and x-ray imaging techniques have provided, and continue to provide, deeper knowledge and understanding of the solidification process than can be obtained ex-situ. Moreover, they have provided fundamental benchmark data of the physical phenomena that occur during solidification to validate theoretical and numerical models. Video data provided by the in-situ visualisation techniques qualitatively shows mechanisms of solidification. Researchers regularly perform manual measurements of dendrite features to obtain quantitative data from in-situ optical and radiographic imaging. However, for bulk solidification scenarios, manual tracking may become infeasible and much data can remain unquantified. Recently, computer vision techniques have been emerging in solidification research for tracking and measuring fundamental solidification data from the in-situ footage; Liotti et al. used machine learning to pinpoint nucleation events and measure nucleation undercooling for thousands of individual crystals [43]; Sturz et al. and Mathiesen et al. developed techniques to track growth fronts [44, 45]. McFadden et al. and Murphy et al. used thresholding techniques to track equiaxed volume fractions [46, 47]. Ex-situ works have also demonstrated beneficial use cases for computer vision; Miller et al. and Nenchev et al. used normalised cross-correlation and skeletonisation techniques to detect dendrite centers in SEM micrographs automatically [48, 49]. 3D reconstructions are routinely performed using computed tomography [25]. Convolutional neural networks have been used to perform fast image segmentation in Al-Si [50] and Al-Cu [51, 52] alloys, which can be a bottleneck in developing 3D reconstructions via x-ray tomography. Deep learning

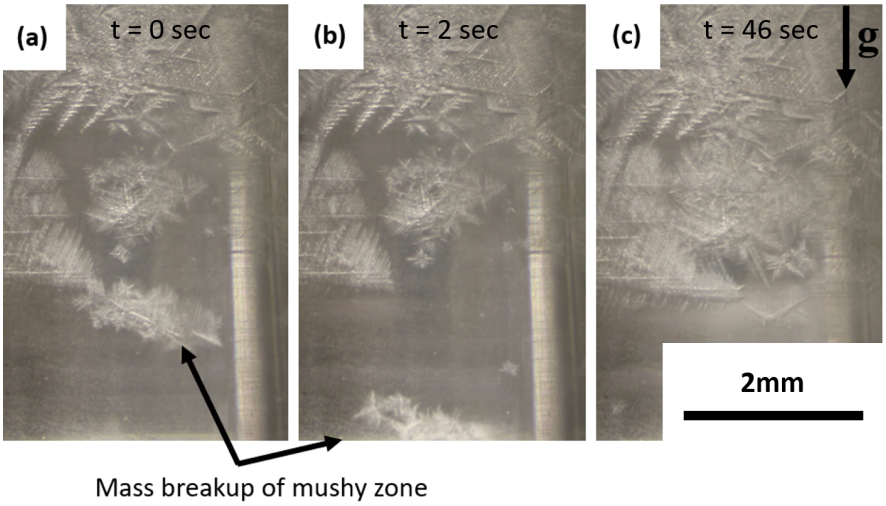

Figure 1.3: Optical image sequence of downward directional solidification shows large clusters of equiaxed crystals fragmenting from the mushy network.

methods are also being used for materials microstructure classification, for example, to classify Ti-6Al-4V [53] and steel [54, 55] microstructures. Computer vision systems provide quantitative data on the solidification processes and help investigators better understand and communicate solidification mechanisms.

1.1.4 Microgravity

Gravity effects on the solidification process have been the subject of many experimental, theoretical and numerical works since the early '80s. Fundamental investigations on solidification theory are complicated by gravity-driven phenomena such as thermosolutal flows, buoyancy and sedimentation. For example, Glicksman et al. showed that dendritic growth is dominated by thermosolutal flow at low undercooling [41, 56, 57].

So far, directional solidification has only been described in the upwards direction. A simple inversion of the solidification direction with respect to the gravity vector demonstrates gravity's influence. Figure 1.2 provided a schematic of the classical grain textures observed during upwards directional solidification. In this scenario, the liquid melt is thermally stable; i.e. the imposed temperature profile and liquid thermal expansion cause a negative density profile along the y-direction, which thermally stabilises the liquid melt. However, for downwards directional solidification, the opposite happens. The imposed temperature gradient destabilises the liquid melt and results in buoyancy-driven flow [58–66]. Figure 1.3 shows a significantly different outcome for

downwards directional solidification with large fragments breaking from the coherent mush producing clusters of equiaxed crystals. Thus, gravity effects are a crucial topic in solidification research.

1.1.5 The CETSOL Project

This work is carried out in the context of the European Space Agency Microgravity Applications Promotion (ESA-MAP) project entitled Columnar-to-Equiaxed Transition during SOLidification (CETSOL). The overarching objective of the CETSOL project is to validate and further develop numerical modelling of grain structure formation in industrially important castings. In particular, to give scientists and industrialists confidence in the reliability of integrated numerical models of casting, which facilitate the optimisation of solidification manufacturing processes.

The CETSOL project includes microgravity and terrestrial experimental campaigns with Al-Si and Al-Cu alloys and NPG-DC transparent model alloys combined with the development and validation of numerical models capable of predicting the position or progression of a CET. The NPG-DC model alloy samples will be examined under microgravity conditions in the Materials Science Glovebox onboard the International Space Station (ISS). As noted in section 1.1.4, the microgravity environment provides diffusive conditions without the complicating effects of buoyancy-driven flow and sedimentation. The ISS experiments with the NPG-DC alloys will comprise a sample volume of 6 x 6 mm square cross-section and 100 mm length. The parameters gained by microgravity experiments will be determined and compared to ground-based experiments and numerical predictions.

The aim of this thesis in the context of the CETSOL project is to provide complementary terrestrial experiments with the NPG-DC alloy system for both the validation of numerical models and for comparison to the microgravity experiments conducted in sounding rocket missions and onboard the ISS. Image processing and computer vision techniques will aid in the data extraction from video footage captured during terrestrial experiments with the transparent model alloy allowing for deeper characterisation of the dendritic growth. The data will be compared with theoretical and numerical

models as well as microgravity experiments.

1.2 Thesis Objectives and Contribution

The overarching aim of this work is to develop an experimental facility in combination with image processing and computer-vision techniques for the visualisation and characterisation of dendritic growth structures in the transparent model alloy Neopentyl Glycol-35wt.%(D)Camphor. In order to achieve this goal, the following objectives are identified:

1. to develop an experimental facility for directional solidification which facilitates in-situ visualisation of the solidification process under controlled cooling rate, temperature gradient and isotherm speed

2. to develop computer vision and image processing techniques for use with the in-situ optical video data for better visualisation and characterisation of micro and macro structure development

3. to provide complementary terrestrial data for microgravity investigations with the NPG-DC system as part of the CETSOL framework

4. to investigate competitive growth mechanisms during directional solidification in the $\langle 111 \rangle$ transparent alloy NPG-35wt.%DC and apply image processing and computer vision techniques to further elucidate competitive growth mechanisms.

Directional solidification experiments with a cylindrical sample volume of 8mm diameter cross-section by 450 mm length will be used to study the dendritic growth with the transparent model alloy NPG-35wt.%DC. The experiments will allow for the visualisation of dendritic forests. At the same time, computer vision and image processing techniques applied to in-situ video data will aid in the characterisation of columnar and equiaxed dendritic growth in the transparent model alloy. The experiments and techniques developed in this work will provide new insights on dendrite growth and competitive grain growth. This work will provide important validation criteria for numerical and theoretical models of solidification to give confidence in the reliability of

integrated numerical models of casting, which facilitate the optimisation of solidification manufacturing processes.

1.3 Thesis Structure

This thesis is structured so that each chapter can be a standalone publication in a journal. Accordingly, the upcoming chapters consist of either a journal publication or work that is under preparation for a journal and a final chapter for conclusions. In general, Chapters 2 - 4 comprise a journal publication structure with traditional sections headings of; Abstract, Introduction, Methodology, Results, Discussion, and Conclusions. The introduction provides a literature review, identifies gaps in the knowledge, and then closes with the chapters' aims and objectives. For the methodology section, Chapter 2 provides a detailed description of the newly developed experimental facility [67]. Chapter 2 lays the foundation for experiments and analysis techniques that are described in Chapters 3 and 4. Hence the methodology sections for Chapters 3 and 4 provide a brief description of the experimental facility (citing [67] for a more detailed description). Chapters 3 and 4 then proceed with a detailed description of novel methodologies pertinent to that chapter, for example, the newly developed computer vision technique for multiple dendrite tip tracking described in Chapter 3. Finally, the results, discussion and conclusions, are provided.

The upcoming contents of the thesis are outlined as follows:

Chapter 2: reports the work entitled, "A front-tracking measurement technique for in-situ columnar and equiaxed structure growth with controlled solidification", Accepted for publication in: *Measurement Science and Technology*. This chapter provides a detailed description and introduction to the experimental facility and describes the development of an automatic image processing technique to track the solidification front position and calculate growth rates. The growth rate measurements using the new technique and the traditional method (liquidus isotherm speed) are benchmarked against manual measurements of position and growth rate. Results show that auto-

matically tracked growth rate compares well throughout experiments with errors less than 2.7%. Contrastingly, isotherm speed was in error up to 19%.

Chapter 3: reports the work entitled, "Multiple dendrite tip tracking for in-situ directional solidification: experiments and comparisons to theory," Accepted for publication in: *Materials Today Communications*. This chapter presents a novel computer vision algorithm for automatically detecting and tracking multiple columnar dendrite tips from in-situ video data of directional solidification. Instead of selecting a few dendrites for manual analysis from video data, the technique facilitates growth rate analysis of dendritic forests. Terrestrial measurements for the dendrite tip velocity and undercooling relationship are thus provided and are compared with the available microgravity data. Comparisons are made to the classical Lipton-Glicksman-Kurz (LGK) model and to a modified LGK model adapted with a finite diffusional boundary layer theory to account for convection effects. The chapter also describes an oscillatory component to the tip velocity between adjacent columnar dendrites. The tip tracking algorithm is beneficial as it allows for the tracking of hundreds of dendrite tips, hence providing statistical and qualitative insights that are otherwise difficult to reconcile using traditional methods.

Chapter 4: reports the work entitled, "Competitive growth during directional solidification of $\langle 111 \rangle$ columnar dendrites", *Under Preparation*. This chapter explores competitive growth mechanisms in the transparent model alloy, NPG-35wt.%DC. The alloy in question grows along $\langle 111 \rangle$ crystallographic directions [68]. Presently, there are no in-situ investigations on competitive growth in $\langle 111 \rangle$ alloys. This chapter compares competitive growth mechanisms for $\langle 111 \rangle$ dendrites to the widely accepted Walton-Chalmers rule and finds multiple scenarios that obey and disobey the Walton-Chalmers rule. Unfavourably oriented crystal colonies at diverging grain boundaries are shown to compete with and outgrow favourably oriented colonies via tertiary branching. It is proposed that the deviation from the Walton-Chalmers rule of competitive growth is probabilistic and likely depends on the initial seeding.

Chapter 5: Summarises the thesis' major findings and contributions to knowledge, with suggestions for future work.

Chapter 2

A Front-Tracking Measurement Technique for In-Situ Columnar and Equiaxed Structure Growth with Controlled Solidification

Abstract

Growth rate is an important consideration in solidification as it influences features of the micro and macrostructure such as morphology and the columnar to equiaxed transition. Thus, accurately quantifying the growth rate is key to understanding the solidification process as well as verifying numerical simulations. In this work, an experimental apparatus has been developed to investigate in-situ directional solidification using a transparent analogue material; neopentyl glycol-35wt%(d)camphor. The facility enables the control of the mushy zone growth rate as well as the imposed temperature gradient during solidification, similar to Bridgman type furnaces. Image processing techniques were developed for automated tracking of position and growth rate of the solidification front using background subtraction on photographic image sequences captured in experiments. Growth rate measurements using this technique and the traditional method (liquidus isotherm speed) have been benchmarked against manual measurements of position and growth rate. Results show that automatically tracked

growth rate compares well throughout experiments with errors less than 2.7%. Contrastingly, isotherm speed was in error up to 19%. Three columnar and two equiaxed morphologies were investigated and solidification fronts were characterised for their growth rates and thermal conditions.

2.1 Introduction

Control of the solidification process, the development of microstructures during solidification, and the impact upon the resulting material properties continue to be an essential yet technologically challenging task for developing high-quality cast, welded and additively manufactured parts. Solidification conditions, such as temperature gradient and cooling rate, directly influence the microstructure and grain texture in the as-cast solid and therefore have a direct effect on the quality and mechanical properties [69, 70].

Directional solidification refers to the case where the solidification occurs along a known or preferred direction. Under laboratory conditions involving cylindrical crucibles, the solidification is controlled by managing the thermal conditions so that the growth direction is aligned with the crucible axis. Different crystal morphologies can arise depending on the process parameters imposed during the solidification process. The different crystal morphologies lead to different crystal textures and properties at the macroscale of the casting. One such texture is called a columnar grain structure (see figure 2.1) where elongated grains (i.e. with high aspect ratio) are aligned in a common direction. Another texture is called an equiaxed grain structure where grains have a lower aspect ratio (typically less than two) and random orientation. Columnar structures have been shown to provide superior creep resistance in metal alloys operating at elevated operating temperatures [11] while fine equiaxed structures provide a higher yield strength as described by the Hall-Petch relationship [7, 8].

A Columnar to Equiaxed Transition (CET) can occur during solidification when transient thermal conditions exist. For example, casting conditions that initially favour columnar growth (high temperature gradient or low growth rate) can change to favour equiaxed growth (low temperature gradient or high growth rate) giving rise to a CET.

Growth rate and temperature gradient are therefore important considerations in studies on CET.

In particular, numerical models that attempt to simulate the thermal conditions for CET require deeper information about the process from experiments [5, 6, 71, 72]. However, the validation of numerical simulations can be problematic due to a lack of detail regarding boundary conditions in the experimental work. Furthermore, traditional metallographic analysis of experimental samples is termed ex-situ or post mortem analysis; that is, the analysis takes place after the sample has been processed and has cooled to room temperature. In-situ analysis of the solidification as it occurs is preferable for model validation. In-situ experiments are, however, difficult to achieve due to the opaque nature of metals in the visible spectrum as well as the opaque ceramic furnaces that are used for metal processing. One approach is to use x-ray technology to observe crystal growth [24, 73–77], but this approach is limited to thin samples and alloys that have sufficiently different x-ray absorption rates to give good image contrast.

Another approach to in-situ analysis is the use of transparent organic materials that solidify in a similar way to metals [13] and which form columnar and equiaxed microstructures. These materials are referred to as transparent model alloys or transparent analogues. Provided that transparent crucibles are used, they facilitate real-time visualisation of solidification processes using optical video microscopy. Experiments with these analogues have advanced knowledge and understanding in solidification research (see reviews [78–80]). One such transparent analogue is the binary system of Neopentyl Glycol and (d)Camphor (NPG-DC). Recently, microgravity experiments with this system provided benchmark data for numerical models independent of the gravity-driven phenomena such as buoyancy-driven flow and sedimentation [47, 81–83]. Future work on NPG-DC alloys is planned onboard the International Space Station for investigating CET [84].

Figure 2.1 shows a schematic of directional solidification for columnar growth (left) and equiaxed growth (right). The schematic shows the liquid zone and the mushy zone (mix of liquid and solid), denoted L and M, respectively. Additionally, for the case of equiaxed growth, figure 2.1 delineates the equiaxed mushy zone into coherent and

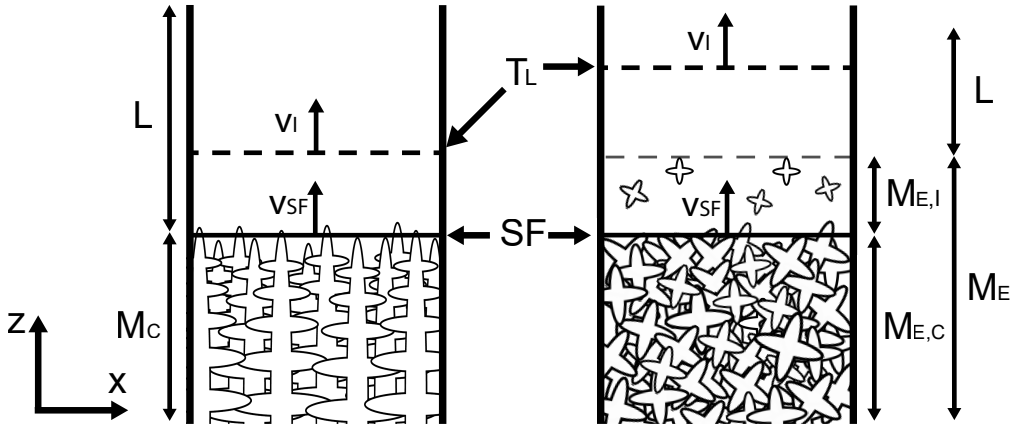

Figure 2.1: Graphical representation of directional solidification defining important positions and regions for columnar growth (left) and equiaxed growth (right). L, Liquid zone; M_C, Columnar mushy zone; M_E, Equiaxed mushy zone; $M_{E,I}$, Incoherent equiaxed mush; $M_{E,C}$, Coherent equiaxed mush; T_L, equilibrium liquidus isotherm; SF, solidification front; v_I, equilibrium liquidus isotherm speed; v_{SF}, growth rate.

incoherent zones, $M_{E,C}$ and $M_{E,I}$, respectively. In equiaxed dendritic solidification, the nucleated equiaxed crystals can move freely in the melt and this is called the incoherent mushy zone. When the free-to-move dendrites sediment and grow to impinge on one another, the dendritic network becomes coherent (i.e. the dendrites' motion becomes restricted). Figure 2.1 shows the solidification front (SF) of interest in this study at the top of the columnar mushy zone (left) and at the top of the coherent equiaxed mushy zone (right). The SF proceeds upwards with a growth rate, v_{SF}. The equilibrium liquidus isotherm, T_L, advances with a velocity, v_I, called the equilibrium liquidus isotherm velocity.

Relationships between growth rate, morphological transitions and dendrite characteristics are well documented for transparent analogues [80, 85, 86]. Figure 2.2 shows how controlling the temperature gradient, and the cooling rate facilitates growth rate control in a static crucible. Two heaters either side of the adiabatic baffle zone (sometimes a heater and heat exchanger) maintain a hot and cold side thus providing a temperature gradient, G (shown in figure 2.2). By subsequently applying a cooling rate equally throughout the baffle zone the solidification front grows upwards and, following an initial transient period, the isotherm speed, v_I, provides an estimate of the growth rate as follows:

$$\frac{\Delta z}{\Delta t} = \left(\frac{\Delta T}{\Delta t}\right)\left(\frac{\Delta z}{\Delta T}\right) \tag{2.1}$$

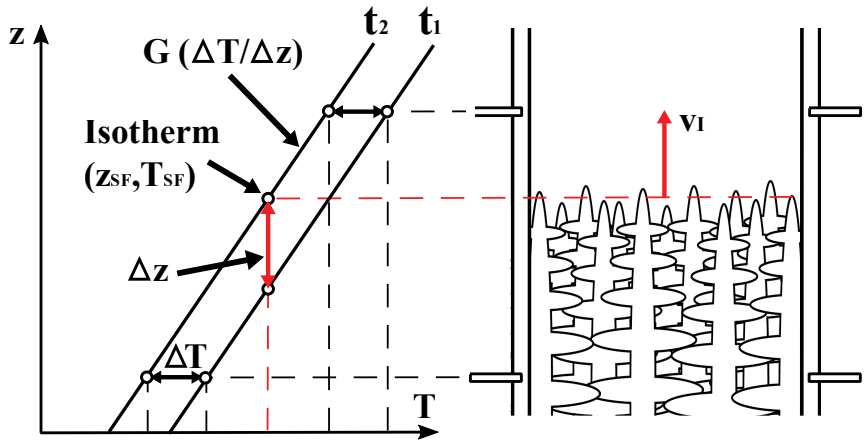

Figure 2.2: Graphical representation of the assumed alignment of the mushy zone. Temperature profiles assumed during isotherm speed measurement at two time instants; t_1 and t_2, and schematic of the adiabatic baffle zone (right) corresponding to time t_2.

$$v_I = -\dot{T}\left(\frac{1}{G}\right) \tag{2.2}$$

Additionally, the temperature profile can be used to give a basic estimate of the position of the mushy zone. Based on equilibrium conditions, the mushy zone may be assumed to exist between the liquidus and solidus or eutectic isotherms, as appropriate. In this case, the bounding isotherms (i.e. the liquidus and solidus) are typically calculated based on the original composition of the alloy. However, under steady growth conditions, even when the liquidus isotherm speed and the growth rate are well-matched, the liquidus isotherm position and the boundary of the mushy zone may not match. This mismatch may arise due to the crystal tips, which define the extent of the mushy zone, growing at temperatures below the equilibrium liquidus temperature (i.e. a tip undercooling must exist). Partitioning of solute at the interface and diffusion into the liquid melt ahead of the dendrite tips causes constitutional undercooling [87]. Misalignment between the growth direction of columnar tips and the heat flow direction typically causes a greater mismatch between liquidus isotherm position and the crystal tips. In the case of an equiaxed mushy zone, nucleation of crystals occurs at some finite level of undercooling deeper within the mushy zone and the resulting coherent equiaxed growth front does not align with the moving liquidus isotherm. If the growth conditions are nonsteady due to transient thermal conditions, then the growth may deviate further from the set conditions. Mota et al. [19] have

shown that after initial pulling in a Bridgman furnace, the growth rate can take 40 minutes to 2 hours to reach a steady state with a succinonitrile and camphor transparent analogue. It is clear that the application of the equilibrium liquidus isotherms to define the extent of the mushy zone can be problematic. This has implications regarding the interpretation of the physics as well as for validating simulations.

An experimental apparatus has been developed in this investigation that implements directional solidification using the NPG-DC transparent analogue in a transparent sapphire crucible. This allows for visualisation and videography of the mushy zone development as well as the grain textures. An image processing technique has been developed to track the position and speed of the solidification front with time, providing an averaged position and velocity of columnar tips in the bulk direction of growth. The image processing technique also tracks the growth rate for fully equiaxed growth by tracking the top of the coherent mushy zone. The results are compared with liquidus isotherm speed measurements and manual reference measurements of position and growth rate. Importantly, the growth rate measurements are obtained with well-defined and accurately quantified experimental boundary conditions. The experiments thus provide accurate thermal input data for simulation research in the form of measured boundary conditions and output data related to the crystal morphology. This data will allow for code validation to take place.

This contribution aims to describe the application of a unique directional solidification test rig that includes thermal instrumentation and control in combination with automatic image processing to track position and calculate growth rates for columnar and equiaxed crystal growth fronts. The objectives are:

- To provide technical details on the development of the new experimental facility and to provide thermal calibration data.

- To describe the development of a new image processing technique for tracking the position and growth rate of the solidification front.

- To benchmark the newly developed automated tracking technique against manually assigned growth rate and front positions.

- To compare the automatically calculated growth rates to the manually assigned growth rates and traditional isotherm speed estimation.

2.2 Description of Materials & Methods

2.2.1 Apparatus

Figure 2.3 shows a technical illustration of the experimental apparatus. It consists of a vertical sapphire tube of 450 mm length, with an inner diameter of 8 mm and an outer diameter of 10mm. Sapphire was chosen as the crucible material because it is optically transparent, allowing visualisation of the top of the mushy zone and, due to its high thermal conductivity (40 W/mK), facilitates heat transfer to and from the material with low (< 1 K) temperature difference across the crucible wall.

A resistively heated coiled nichrome wire is wrapped tightly around the outer tube wall with a layer of thermally conductive silicone to provide adequate thermal contact and electrical isolation. This region acts as the heat source in the upper section of the crucible. Electrical power is supplied to the resistive coil with an Automatik EA-PSI 8360-10 T DC power supply. The power supply is controlled with a dedicated computer (see figure 2.4), which is connected with an EA-IF-U1 interface card. Heat is extracted from the lower section with a 170mm-long tube and shell type heat exchanger. A precision chiller (Julabo A40) in series with a pump supplies chilled water to the tube and shell heat exchanger with initial setpoint temperatures followed by controlled cooling rates ranging 0.2 - 1 K/min.

Figure 2.3 shows the baffle zone between the heater and the chiller. A camera (Canon EOS 1100D, 12 Megapixel sensor) with a variable lens (Navitar 1.4 x – 13 x zoom) mounted perpendicularly to the sample vertical axis records image sequences of the solidification process within the dashed region of the baffle zone shown in figure 2.3. Thermocouples on the wall of the sapphire tube in the baffle zone monitor the temperature and are used to determine the thermal gradient, G, and cooling rate, $\dot{\mathrm{T}}$ in the region.

Temperatures on the wall of the sapphire crucible, T_H, T_{A1}, T_{A2} and T_C all denote

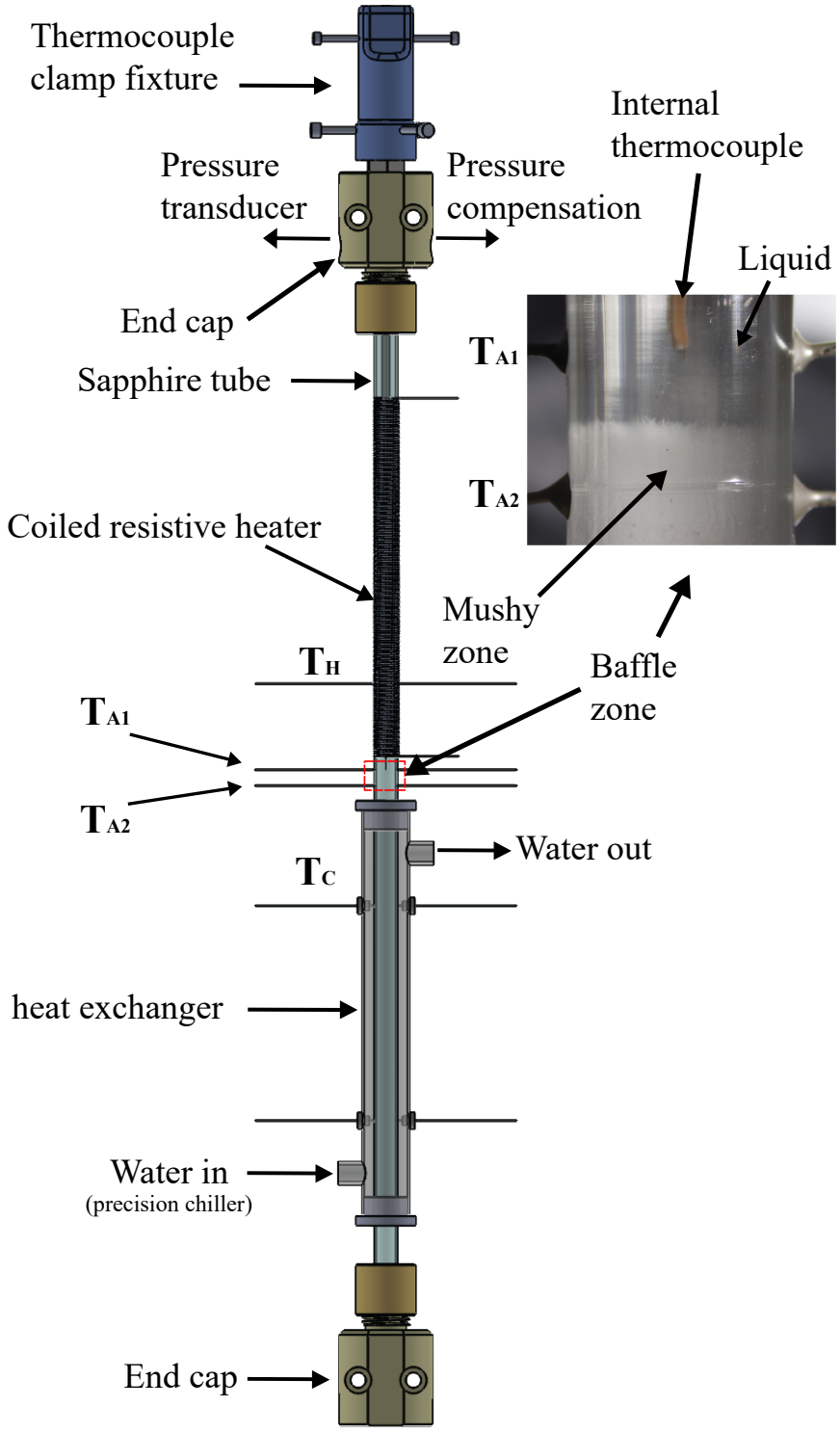

Figure 2.3: Technical illustration of apparatus with highlighted view of an acquired image. In the upper right, the baffle zone is shown up close with solid growing directionally upwards.

the average of two thermocouples at the given height. T_H and T_C are controlled to set the thermal gradient and cooling rate in the baffle zone while thermocouples on the wall of the sapphire tube in the baffle zone, T_{A1} and T_{A2}, monitor the thermal gradient, G, and cooling rate, $\dot{T}$, on the crucible wall in the region where solidification occurs.

End caps at either end of the sapphire crucible, shown in figure 2.3, serve both as fixtures of the test section to an aluminium frame (not shown) as well as providing a pass-through seal to and from the crucible. This facilitates an air-tight connection of a pressure transducer along with conduit piping; one for adding and removing the model alloy and one to allow outflow when filling the crucible. At different heights along the wall of the sapphire tube, pairs of 0.5 mm diameter blind holes have been drilled, diametrically opposed to one another, into which T-type thermocouples have been inserted with a small amount of thermal adhesive for non-invasive wall temperature measurement. Two thermocouples embedded in the wall of the crucible in the cooled region provides the temperature, denoted T_C, indicated in figure 2.3 and 2.4. For internal temperature measurements, an 80 μm diameter T-type thermocouple with Teflon sheath and exposed junction is optionally traversed into the crucible from the top of the rig through an O-ring seal. The internal thermocouple is housed in a 3mm outer diameter stainless steel tube which is used for positioning and extends 30 mm from the end of the tube into the baffle zone. A clamp fixture, shown in figure 2.3, holds the thermocouple in place and allows for accurate positioning of the probe in the baffle zone.

2.2.2 Materials

The transparent model alloy, NPG-35wt.%DC, was prepared from organic crystalline materials, Neopentyl Glycol and (D)Camphor, supplied by Sigma Aldrich. Since NPG is hygroscopic, the sample was prepared in a sealed glovebox under Argon atmosphere with $H_2O < 5ppm$. Liquid NPG-35wt.%DC was then transferred from the glovebox via a high-temperature gas-tight glass syringe and injected into the experimental facility at the lower end cap via a Leur Lok valve. The transparent model alloy under investigation is a hypoeutectic composition with a $\langle 111 \rangle$ dendritic orientation and is a CET former.

2.2.3 Experimental Control

Control of the temperatures of the heater and chiller, T_H and T_C respectively, facilitate the application of nominal temperature gradient, G, and cooling rate $\dot{T}$ in the baffle zone, and hence isotherm speed can be calculated via Eq. 2.2. When the heater and chiller temperatures are decreased at the same rate, the cooling rates $\dot{T}_{A1}$ and $\dot{T}_{A2}$ in the baffle zone reach steady-state after which averaged values for cooling rate, isotherm speed, and temperature gradient are recorded.

Figure 2.4 shows a schematic of the control setup for the experiment. For each experiment, T_H and T_C were initially kept constant at a pre-set value. T_C was kept constant by controlling the coolant temperature of the chiller and subsequently ramped down at a given cooling rate between 0.2 and 1 K/min for the duration of the experiment using the controls on the precision chiller. The power supplied to the electrical heater was modulated with a Proportional and Integral (PI) feedback control loop using the heater temperature, T_H, as the process variable. The feedback control was run with LabView® triggering the power supply using an Automatik EA-IF-U1 interface card to signal the electrical power supply. In this way, T_H could then be ramped down at the same cooling rate as $\dot{T}_C = dT_C/dt$ in order to maintain a constant temperature gradient $G = (T_H - T_C)/z$, with z_{HC} being the axial distance between thermocouples T_H and T_C. Thus, for a fixed G specified by the user, the setpoint T_H for the controller is calculated as:

$$T_H = T_C + Gz_{HC} \tag{2.3}$$

2.2.4 Experimental Procedure

This work investigated directional solidification occurring vertically upward from the cooled solid zone following initiation of a controlled ramp down change of T_C and T_H. To investigate conditions leading to a columnar to equiaxed transition, the cooling rate $\dot{T}$ and hence liquidus isotherm speed, v_I, were varied, and the temperature gradient, G was kept constant for all experiments. In a given test the morphologies were char-

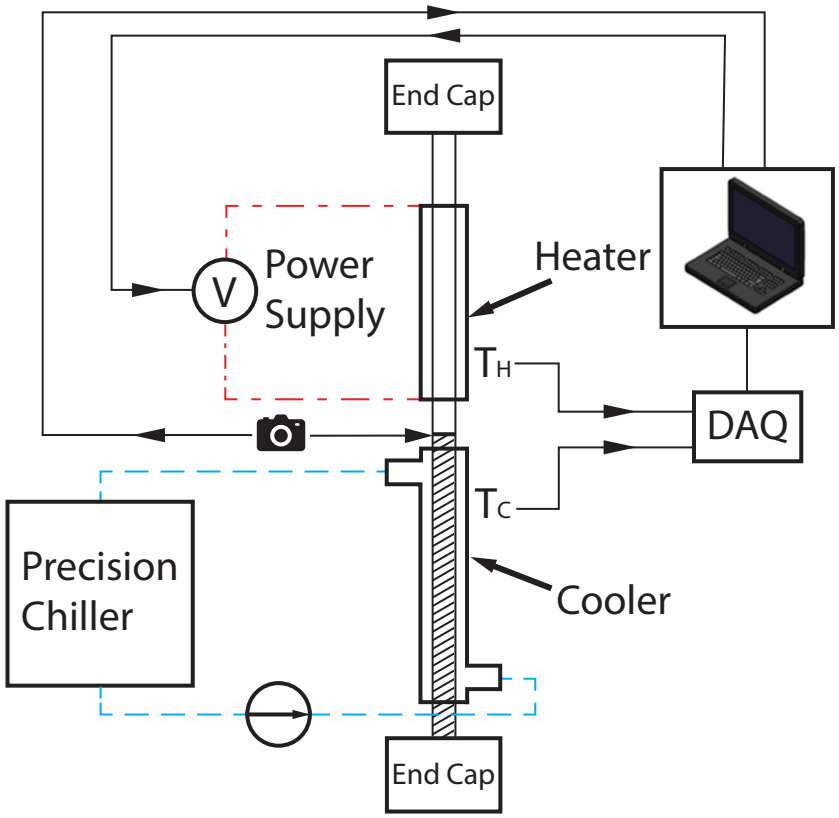

Figure 2.4: Schematic diagram of experimental facility

acterised as being either fully columnar or fully equiaxed after review of the optical camera footage. Subsequent tests were then performed for different values of applied cooling rate $\dot{T}$, and hence isotherm speeds. For the present experiments, the test material above the cooled heat sink region was initially heated such that the material in the heated section and the baffle zone region was in the liquid phase. T_H and T_C were then adjusted such that the solidification front was just below the camera's Field of View (FoV) and was maintained constant for a period of at least 40 minutes to allow the solidification front to reach the liquidus isotherm. At this point in the experiments, ramp down cooling was initiated, and optical imaging was commenced. Image processing techniques to track the solidification front, described in section 2.2.5, confirmed if the growth rate had achieved steady state. As mentioned, T_C was set by controlling the precision chiller. Simultaneously, T_H was computer-controlled to decrease at the identical rate so as to maintain a constant axial temperature gradient, G, in the baffle zone (see Eq. 2.3). The camera clock, being synchronised with the computer clock, facilitated direct visual correlation of the observed solidification morphology with the instantaneous thermal environment. As this was a relatively slow process, the frame

Table 2.1: A list of the thermal processing parameters during experiments

Test Number	Cooling Rates (K/min)	Temp. Gradient (K/cm)	Isotherm Speed ($\mu m/s$)
I	0.2	18	1.9
II	0.4	18	3.7
III	0.6	18	5.6
IV	1.0	18	9.3
IV	1.0	18	9.3

rate of the camera was set to capture images continuously at 0.5 fps. Table 2.1 lists the imposed process parameters implemented for T_H and T_C while tabulated results for temperature gradient, cooling rate and isotherm speed measurement have been determined using thermocouples seated in the wall of the sapphire tube adjacent to the solidification front and in the baffle zone (T_{A1} and T_{A2}). Eq. 2.2 was used to estimate that the isotherm speeds were between 1.9 and 9.3 $\mu m/s$.

2.2.5 Automatic Front Tracking Algorithm

An image processing technique has been developed for automatically tracking position and growth rate of the advancing solidification front using the photographic image sequences captured during the experiments. The technique employs background subtraction where the grayscale pixel intensities of a frame under evaluation deviating significantly from those of the background model are selected for further processing steps. Several background models have been established in the literature for computer vision applications [88–91]. In the current application, the scene is controlled under laboratory conditions, and the camera is static relative to the crucible with limited background motion. Frame differencing background subtraction is used to threshold for any newly formed solid between two input frames. Figure 2.1 shows a schematic of the baffle zone with the solidification front (SF) and reference coordinates. The automatically tracked position and speed at time t_1 are denoted, z_{t1} and $v_{f,t1}$ respectively. The SF and tracked position z_{t1} is located at the top of the coherent mushy zone, also referred to as the coherency point.

The flow chart in figure 2.5 summarises the algorithm used by the tracker to deter-

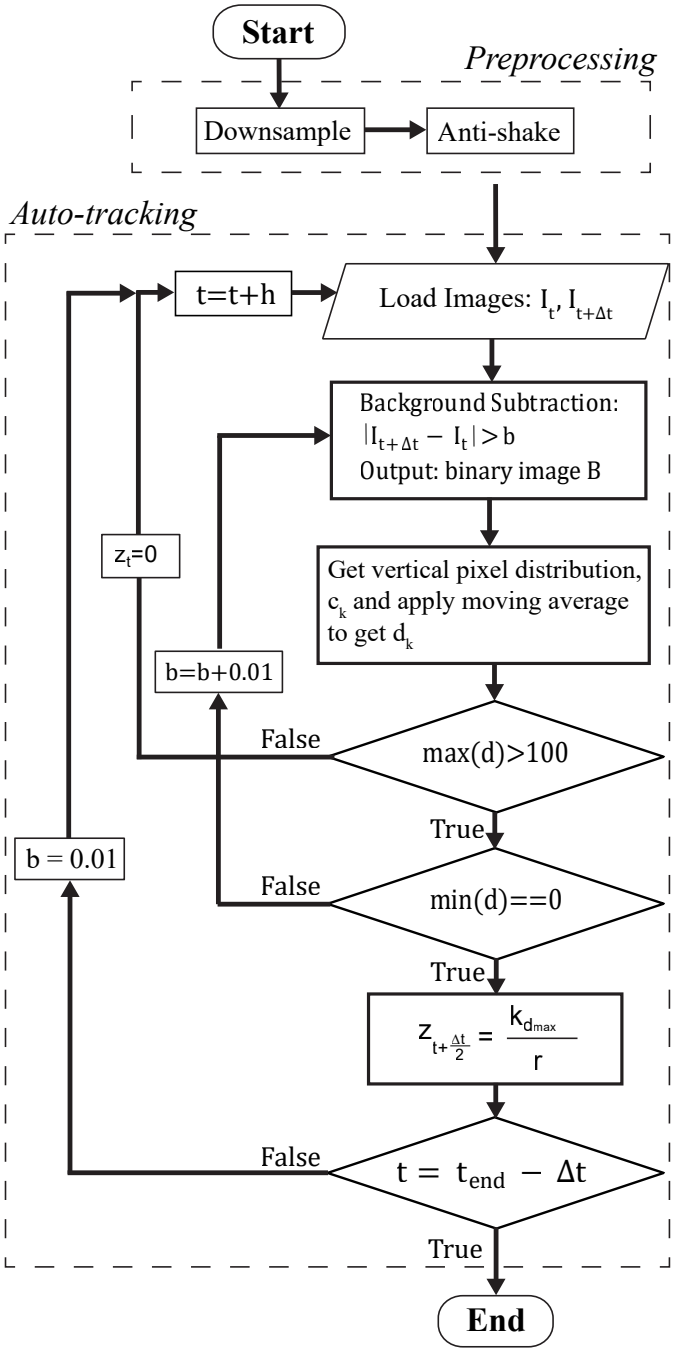

Figure 2.5: Flow chart of auto tracker algorithm

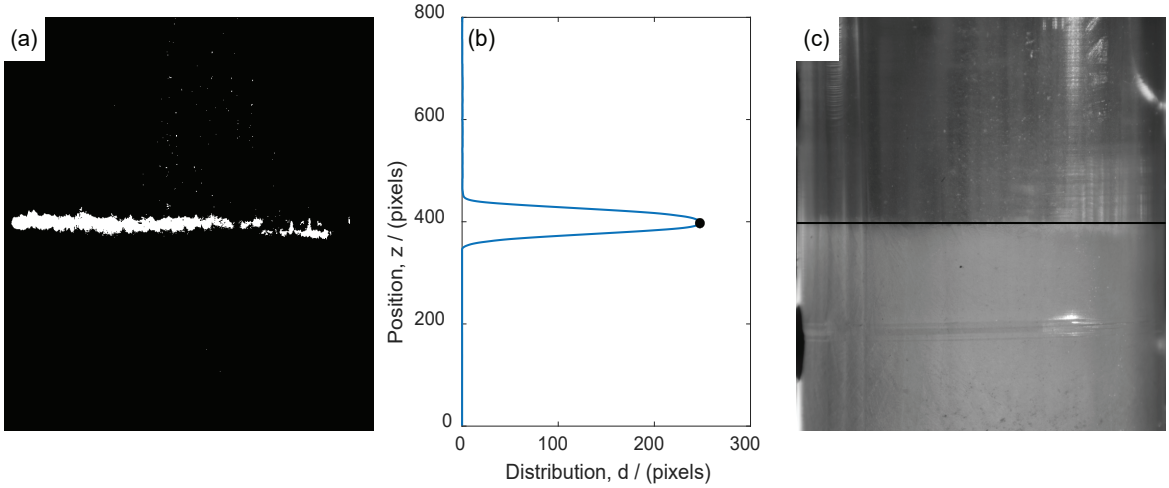

Figure 2.6: Images illustrating steps in the tracker algorithm; (a) 725 x 800 binary image B_{t1} from image subtraction and thresholding, (b) vertical pixel distribution of binary image (after 11 point moving average), and (c) tracker position overlaid onto image in between original input images.

mine the position of the SF. Firstly, high-resolution images are cropped to the width of the sapphire crucible and downsampled by 80% resulting in 6000 x 4000 rgb images being converted to 725 x 800 grayscale images. An anti-shake algorithm is used to preclude any vibrations arising in the microscopic video sequence due to vibrating lab equipment or general lab activity. This is an important step to ensure that the measured growth rate is independent of camera disturbances. To that end, all images in a given sequence are registered to the first image of the sequence. Feature points are detected using the minimum eigenvalue algorithm developed by Shi and Tomasi [92] and matched with the first image in the video sequence to determine any translation or rotation that needs to be applied to the image. Following these pre-processing steps, the tracker algorithm is implemented. First, two sequential grayscale images (725 x 800 pixels) corresponding to times t and $t + \Delta t$ are loaded and denoted I_t and $I_{t+\Delta t}$, respectively. Frame differencing background subtraction is then applied according to Eq. 2.4 as follows:

$$| I_{t+\Delta t} - I_t | > b \tag{2.4}$$

The inequality holds true if, at a given pixel, the absolute value of the difference between the two images is greater than the threshold value, b. Figure 2.6 (a) shows an example of the binary image, B, resulting from the inequality in Eq. 2.4. Summation

of pixels in each row of the binary image is then calculated and smoothed with an unweighted 11 point moving average to provide a vertical distribution of change between the original input images. An example of the resulting smoothed distribution, d_k, is shown in figure 2.6 (b). The index k, where d_k is a maximum, selects the exact vertical pixel location of the solidification front for the image between the two original input images corresponding to time $t_1 = t + \Delta t/2$. Figure 2.6 (c) illustrates the SF position superimposed on the image in between, i.e. I_{t1}.

The position corresponds to the middle row of the block of 725 x 11 pixels with the highest number of pixels passing the threshold. The pixel resolutions for each experiment are measured using ImageJ software and, knowing the diameter of the crucible, original images give a resolution of approximately 2.8 $\mu m/px$ and correspondingly 13.9 $\mu m/px$ for downsampled images.

Depending on the value of the threshold, b, unwanted pixels may appear in the foreground if the threshold is too low. Contrastingly, an insufficient amount of pixels may pass the threshold if the value, b, is too high. As detailed in figure 2.5, the algorithm implements two simple criteria to select the threshold at a given time: (i) if the minimum value of the distribution, d, is not 0 the threshold, b, increments by 0.01 and the algorithm returns to the image subtraction step with an increased threshold. This ensures that a region of at least 11 rows in the foreground mask consists entirely of pixels failing the threshold b; (ii) the maximum value of the smoothed distribution d_k must be greater than 100 to ensure that a prominent peak has been obtained. If the second condition is also satisfied, the location of the maximum value of the smoothed distribution then passes as the position of the solidification front. In the scenario where the second condition is false, the algorithm assigns a placeholder value to the position for that iteration and continues to the next timestep of the video sequence. The position determined directly from the image sequence, z_{t1},is subsequently smoothed using a Savitsky-Golay filter with a window of length $N_k/4$. The resulting filtered data denoted $z_{f,t1}$, then used to determine the tracker growth rate, v_T, using Eq. 2.5.

$$v_T = \frac{z_{f,t1+1} - z_{f,t1-1}}{t_{t1+1} - t_{t1-1}} \tag{2.5}$$

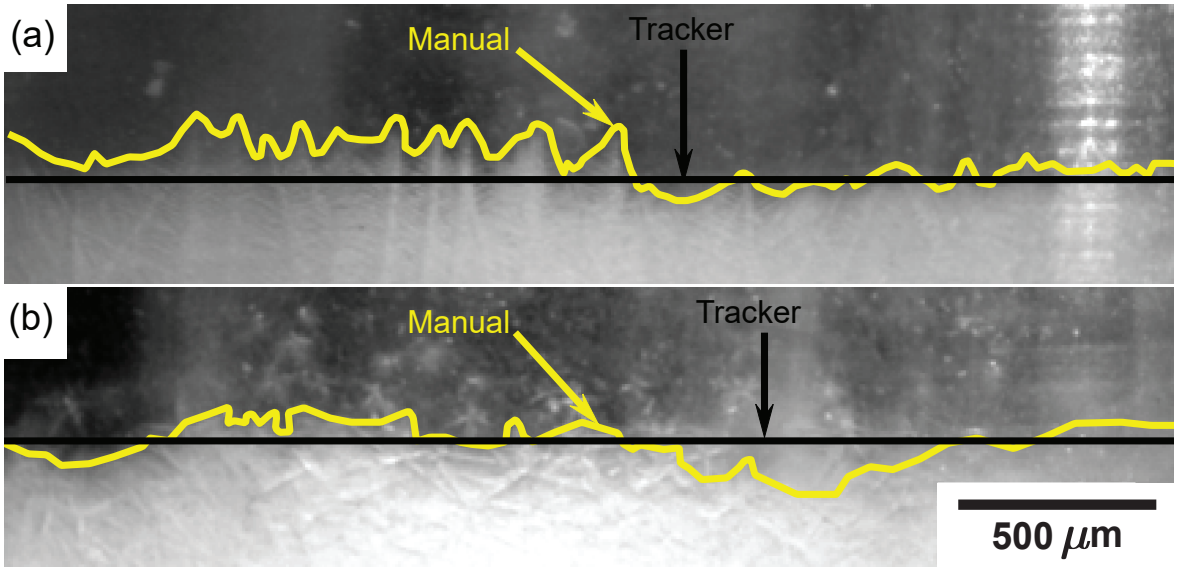

Figure 2.7: Close up of manual trace and tracker position; (a) fully columnar growth, (b) full equiaxed growth.

The tracker algorithm has been implemented in the MATLAB® 2020a environment. Additionally, the anti-shake algorithm has been employed using the MATLAB® implementation of the minimum eigenvalue algorithm and feature matching algorithm.

2.2.6 Reference Position and Growth Rate Measurements

Manual position and growth rate measurements were used as a reference to assess the accuracy of the tracker as well as isotherm speed. A total of 40 images, equally spaced in time throughout each experiment, were selected. For each of the 40 images in a given experiment, the boundary of the top of the coherent mushy zone or the top of the columnar mushy zone was drawn manually. Figure 2.7 shows a close-up example of the manually drawn boundary for (a) fully columnar growth and (b) fully equiaxed growth. The boundary was first defined by a series of manually placed vertices connected by straight lines. A second set of vertices were generated with equal spacing along the length of the boundary and the mean height of the second set of vertices was used for determining the average height. The manual growth rate measurements were then determined by central differencing of the manual position and time data.

Table 2.2: Summary of sensitivity coefficients and standard variances for propagation of uncertainty in thermal measurements.

Measurement	Input	Functional Relationship	Sensitivity Coefficients	Standard Variance
	x_i	$f(x_i)$	$\frac{\delta f}{\delta x_i}$	$u_c^2(y)$
Mean Temp.	T_{z1}, T_{z2}	$T_z = \frac{T_{z1} - T_{z2}}{2}$	$\frac{1}{2}, \frac{1}{2}$	$\frac{1}{N} u_T^2$
Temp. Difference	T_{a1}, T_{a2}	$\Delta T = T_{a2} - T_{a1}$	1,-1	$u_{T_{a1}}^2 + u_{T_{a2}}^2$
Ext. Temp. Gradient	$\Delta T, \Delta z$	$G = \frac{\Delta T}{\Delta z}$	$\frac{1}{\Delta z}, -\frac{\Delta T}{\Delta z^2}$	$\left(\frac{1}{\Delta z}\right)^2 u_{\Delta T}^2 + \left(-\frac{\Delta T}{\Delta z^2}\right)^2 u_{\Delta z}^2$
Isotherm Speed	$G_i, \dot{T}$	$V_I = \frac{\dot{T}}{G}$	$\frac{1}{G}, -\frac{\dot{T}}{G^2}$	$\left(\frac{1}{G_i}\right)^2 u_{G_i}^2 + \left(-\frac{\dot{T}}{G_i^2}\right)^2 u_{T_i}^2$

2.2.7 Thermal Calibration

The propagation of uncertainty in measurement is detailed in this section. Expanded measurement uncertainties have been established with a normal distribution and a coverage factor k = 2. All T-type thermocouples have been calibrated using a reference Platinum RTD which has a standard uncertainty traceable to national standards of 0.025 $°C$ For onvenience, the maximum temperature measurement uncertainty established during calibration of T-type thermocouples has been applied as a suitable uncertainty for all thermocouple measurements. Summation in quadrature of the independent sources of uncertainty has provided a standard uncertainty of $u_T = 0.065°C$ with expanded uncertainty $U_T = 0.13°C$. The propagation of measurement uncertainty has been determined as standard using Eq. 2.6 as follows:

$$u_c(y) = \sqrt{\sum_{i=1}^{N} \left(\frac{\delta f}{\delta x_i}\right)^2 u^2(x_i)} \tag{2.6}$$

where there are N input measurements x_i, each having a standard uncertainty $u(x_i)$ and sensitivity coefficient $\delta f / \delta x_i$. The output measurement is denoted y with combined uncertainty $u_c(y)$. Table 2.2 summarises the sensitivity coefficients and standard variances for each measurement. This includes standard variance for mean temperature measurements by two opposing thermocouples at a given height along the crucible wall (see figure 2.3); the uncertainty for a temperature difference ΔT; the uncertainty of the temperature gradient measurements from thermocouples seated on the wall of the sapphire tube; and uncertainty of liquidus isotherm speed.

The thermal environment of the adiabatic baffle zone has been further characterised using internal temperature measurements. The apparatus in figure 2.3 shows an internal thermocouple which is optionally inserted into the crucible via an O-ring seal (not shown) on the upper end-cap. Axial temperature profiles have been measured by traversing the internal thermocouple along the centerline axis of the adiabatic baffle zone providing temperature and position data. Before taking a temperature profile, the setpoints of the heater and heat exchanger, T_H and T_C, were adjusted to achieve a given temperature gradient and maintained for 40 minutes such that the SF was just below the camera FoV. For each externally applied temperature gradient, the internal thermocouple was traversed to 5 discrete heights in the adiabatic baffle zone, and corresponding positions for the thermocouple bead were determined in ImageJ.

Additionally, a range of internal temperature gradients, G_i,were compared with the temperature gradient measurement on the crucible wall, G_e, for providing calibration data in the form of $G_i = b_0 + b_1(G_e)$, where the intercept and slope are denoted b_0 and b_1, respectively. The linear relationship provides a noninvasive measurement of the temperature gradient in the liquid melt with associated measurement uncertainty during tests. The average cooling rate was determined by a linear regression curve fit of time-temperature data acquired during experiments on the wall of the sapphire tube and is denoted $\dot{T}$. The standard error of the slope of the curve fit yielded a standard uncertainty $u_{\dot{T}}$. Finally, the standard uncertainty of isotherm speed, u_{v_I}, is determined using Eq. 2.7.

$$u_{v_I} = \sqrt{\left(\frac{\delta v}{\delta G} u_{Gi}\right)^2 + \left(\frac{\delta v}{\delta \dot{T}} u_{\dot{T}}\right)^2} \tag{2.7}$$

2.3 Results and Discussion

Figure 2.8 shows the internal temperature profiles acquired for thermal calibration. Linear regression fitting shows the temperature profiles in the adiabatic baffle zone approximate well to a linear model with coefficients of determination in the range of 0.977 to 0.999. A range of internal temperature gradients, G_i, and corresponding temperature gradient measurement on the crucible wall, G_e, provide output and input

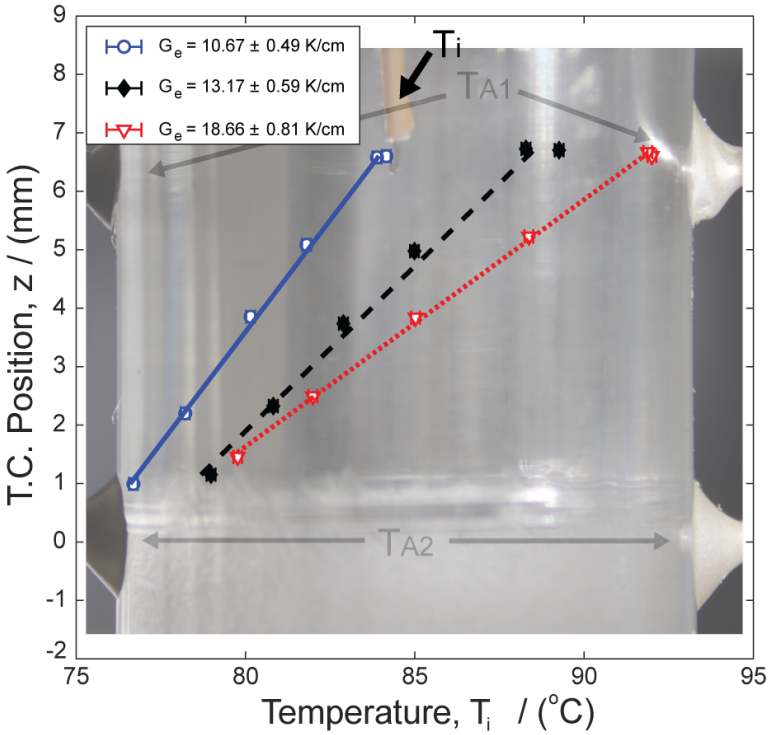

Figure 2.8: Plot of position vs internal temperature for cases of external temperature gradient (details in the legend). Includes overlaid image of the baffle zone with scale and 0 reference corresponding to the z-axis.

variables to the calibration equation, respectively. Figure 2.9 shows the results of the linear regression fit for the internal temperature gradient as a function of external temperature gradient measurement. The calibration curve provided corrected internal temperature gradient measurements with a standard uncertainty, denoted u_{Gi}, of 0.64 K/cm.

Figure 2.10 shows the results of the growth rate and position measurements for two tests using the tracker and manual measurements. The corresponding experimental conditions; cooling rates, thermal gradients and average isotherm speed, are presented in table 2.3. The first row in figure 2.10 shows results for fully columnar growth while the second row show results for a case of fully equiaxed growth. In distinguishing the different growth morphologies, an initially equiaxed crystal is deemed columnar if the length of a primary arm has grown to 4 times that of the other arms. The results show good agreement between the automatic tracking position/speed and the manual reference measurements.

Microscopic videography allowed for the observation of growth morphology and, combined with automatic tracking, temporal measurements of the vertical growth rate.

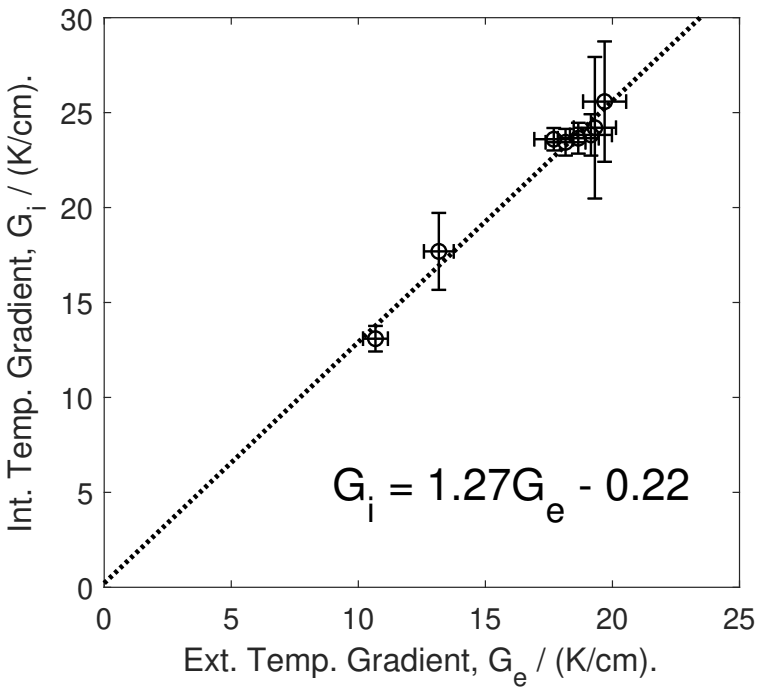

Figure 2.9: Plot of internal vs. external temperature gradient measurements, G_i and G_e, respectively and associated line of best fit by linear regression.

Table 2.3: Experimental results of growth rate measurements (manual reference, v_M, tracker, v_T, and isotherm speed v_I), % difference with respect to reference manual measurement, measured processing conditions and observed macrostructures, denoted S being either, (C) fully columnar or (E) fully equiaxed.

Test	$v_M(\mu m/s)$	$v_T(\mu m/s)$	diff (%)	$v_I(\mu m/s)$	diff (%)	$\dot{T}(K/min)$	$G(K/cm)$	Structure
I	1.16 ± 0.12	1.14 ± 0.15	0.80%	0.96 ± 0.11	16.70%	0.14 ± 0.01	23.46 ± 1.75	C
II	2.31 ± 0.26	2.26 ± 0.27	1.80%	1.96 ± 0.24	15.30%	0.28 ± 0.01	23.53 ± 1.80	C
III	3.47 ± 0.32	3.45 ± 0.26	0.60%	2.88 ± 0.33	16.90%	0.42 ± 0.01	23.57 ± 1.71	C
IV	6.03 ± 1.39	5.88 ± 0.84	2.70%	4.91 ± 0.62	18.70%	0.71 ± 0.01	23.34 ± 1.84	E
V	5.78 ± 1.83	5.75 ± 1.43	0.60%	4.68 ± 0.54	18.90%	0.69 ± 0.02	23.60 ± 1.69	E

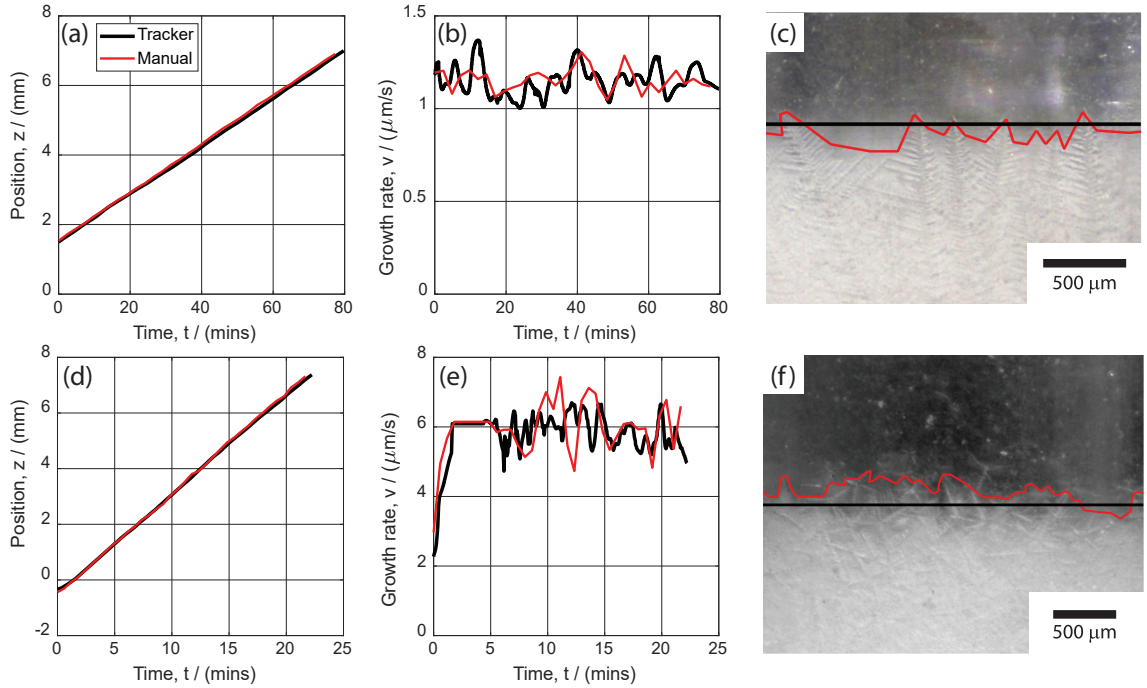

Figure 2.10: Results of tracker and manual measurements for test number I (a - c) and IV (d - f). (a, d) graphs of position measurements, z_T and z_M against time (b, e) graphs of growth rate measurements, v_T and v_M, against time, (c, f) close up images of the solidification front with manual trace and tracker position overlaid

In order to assess the efficacy of different growth rate measurement techniques, the new automatic tracking technique developed here and the traditional isotherm speed measurement technique have been compared with manually measured position/growth rate. The advantages and disadvantages are discussed.

Isotherm speed measurement is useful particularly for ex-situ experiments where liquid melt and the mould walls are opaque. The accuracy of the isotherm speed measurement will depend on the particular experimental setup. When taking isotherm speed measurement, the following is assumed: (i) temperature profile between the thermocouples is linear (ii) cooling rate is uniform in the baffle zone (iii) growth rate is steady. In this work, figure 2.8 shows that the temperature profiles are initially linear within the liquid zone but it should be noted that the temperature profiles were obtained during steady-state conditions in a fully liquid zone. Since cooling rates measured at T_{A1} and T_{A2} are closely matched we assume that cooling in the baffle zone is uniform. Figure 2.10 (b, e) show a steady growth rate for the majority of the period that the solidification front was tracked.

As table 2.3 shows, the isotherm method does not provide accurate temporal mea-

surements and averaged results of the method were between 15.3 to 18.9 % different from the manual reference measurement of growth rate, v_M. All isotherm speed measurements were in fact lower than v_M. One possible cause is that the relationship for the internal temperature gradient as a function of the temperature gradient measured on the crucible wall; $G_i = 1.27G_e - 0.22$, is limited in that it does not account for transient thermal conditions after commencing cooling or the phase change that occurs during experiments; all profiles were obtained by traversing the internal thermocouple along a fully liquid region as it is not possible to traverse the thermocouple through a mushy or solid region.

In contrast, the averaged tracker speed measurements deviated between 0.6 to 2.7 % from the reference. Importantly, temporal speed measurements with the automated tracker compared well for cases of fully columnar and fully equiaxed growth (see figure 2.10 (b, e)), showing robustness of the image processing technique for different morphologies. A key advantage of automatically tracking the growth rate of the solidification front with this technique is it being repeatable and easily implemented over all frames, whereas manual position and hence growth rate measurements for each of the thousands of frames captured during experiments would be impractical, not to mention susceptible to human error.

2.4 Conclusions

An experimental facility and methodology have been developed for investigating in-situ directional solidification of transparent alloys of neopentyl-glycol and (d)camphor. The apparatus, consisting of a transparent sapphire crucible, facilitates optical visualisation of the solidification process in transparent alloys with controlled cooling rate, temperature gradient and isotherm speed, is described in detail and quantifiable experimental uncertainties are provided.

A new image processing technique for in-situ tracking of the position and speed of the solidification front was developed in MATLAB. Growth rates have been measured with the new automatic tracking technique and the traditional isotherm speed technique, and have been compared against manual measurements for five directional

solidification experiments. In all cases, the tracker speed was significantly more reliable than isotherm speed and showed good temporal agreement with manual measurements for cases of fully columnar and fully equiaxed growth. Historically, the isotherm speed measurement technique is accepted as a reasonable approximation for growth rates and is necessarily used for ex-situ experiments, where visual access to the solidification front is not possible. This work, which is capable of assessing the accuracy of the isotherm technique, shows that it can be in error up to 19%, which is significant. In contrast, the new measurement technology developed here compares better than 3% error from manual measurements.

Two growth morphologies were observed for transparent model alloy NPG-35wt%-DC, namely fully columnar, and fully equiaxed. The auto tracked growth rate not only compared well for cases of fully columnar and fully equiaxed growth morphologies but also showed the robustness of the tracker for variation in growth patterns.

The model alloy used in this manuscript has been studied in microgravity conditions on sounding rockets missions [82], and in hypergravity conditions [93] and future work is planned onboard the International Space Station (ISS) with the NPG DC system where buoyancy-driven flow and sedimentation of equiaxed crystals is precluded. Experiments conducted in this manuscript and future work with this experimental facility will serve to provide complementary terrestrial data for future investigations on the ISS. Additionally, by inverting the experimental apparatus, the effect of solidification in the direction of and in opposition to the gravity vector has been investigated [66].

Acknowledgements

This work has been carried out as part of the CETSOL-6 (Columnar-to-Equiaxed Transition in Solidification Processing) funded through the European Space Agency microgravity application programme (contract number: 14313 'CETSOL'(AO-99-117)). Funding was also provided through ESA PRODEX (PEA: 4000110385 CN3) with the support of the Irish Space Delegation at Enterprise Ireland.

Chapter 3

Multiple Dendrite Tip Tracking for In-Situ Directional Solidification: Experiments and Comparisons to Theory

Abstract

Directional solidification experiments of transparent alloy systems typically show multiple dendrites, a forest of dendrites, growing with preferential alignment. At the length scale of centimetres, an experiment could have hundreds of observable dendrites. Analysis of every dendrite would be laborious and practically difficult to implement. Hence, low numbers of dendrites are routinely selected for analysis as they are assumed to be representative of the growth conditions. Hence, many dendrites go without being analysed. Here, a bespoke experimental apparatus with a novel computer vision algorithm is presented that automatically detects and simultaneously tracks multiple columnar dendrite tips from in-situ video data of directional solidification. The benefits of the algorithm are demonstrated with an application to an experimental test case with the transparent alloy system Neopentyl Glycol-35wt.%D-Camphor (NPG-35wt.%DC). Comparisons of dendrite tip velocity and undercooling measurements with microgravity experimental results from the literature showed notable differences. The current

terrestrial data showed similar growth rates but at lower undercoolings (by factors in the range of 0.41 to 0.68) to that measured in the microgravity experiments. Comparisons were made to the classical Lipton-Glicksman-Kurz (LGK) model and to a modified LGK model adapted with a finite diffusional boundary layer theory to account for convection effects. The modified LGK model showed good agreement for boundary layers between 2.5 and 7.0 μm. An oscillatory component to the tip velocity was observed between adjacent columnar dendrites. Video data of columnar dendritic growth augmented with tip velocity vectors are presented. The tip tracking algorithm is beneficial as, with 385 dendrite tips tracked, it provides statistical and qualitative insights that are otherwise difficult to reconcile using traditional methods.

3.1 Introduction

Dendrites are one of the most common crystal growth morphologies found in technologically important alloys. The evolution of dendritic morphologies during solidification play an important role in the quality and material properties of as-cast components. In-situ optical and x-ray radiographic investigations have deepened knowledge and understanding of the fundamental physical phenomena of solidification processes and have provided benchmark data for model validation (see reviews [28, 80, 86, 94]). However, quantitative data extraction from in-situ video sequences is laborious and time-consuming. Moreover, manual tracking of crystals during solidification experiments, which can consist of thousands of frames with hundreds of columnar or equiaxed crystals, makes manual tracking practically difficult. Thus, much information available in the video data can remain unquantified. Several investigators have integrated computer vision and image processing methodologies into their experimental workflows for extracting quantitative data. Examples include the characterisation of nucleation events [43], the measurement of equiaxed volume fractions [46, 47], the tracking of growth fronts [44, 67, 95], the measurement of solute profiles [31, 96–99], and the detection of dendrite centres [48, 49, 100]. While there are methodologies to track equiaxed crystal nucleation, volume fraction and position, there is no equivalent automatic method for columnar dendrite tip tracking within in-situ video data. This manuscript

presents a newly developed computer vision algorithm for automatically detecting and tracking multiple columnar dendrite tips simultaneously using in-situ video data of directional solidification obtained from a bespoke experimental apparatus. The algorithm works by defining a contour of the columnar front for a given frame, similar to the envelope used in mesoscopic modelling and then clustering local maxima of contours into data groups associated with individual dendrites. In this investigation, up to 97 tips have been tracked in a given video sequence and, in total, 385 dendrites were tracked over 6 experiments. The data gathered here will be useful for analytical and numerical model validation.

The Ivantsov solution for steady-state thermal diffusion of an isothermal parabolic dendrite underpins classical dendrite growth theory [101]. Lipton, Glicksman and Kurz [102] coupled Ivantasov's transport solution with marginal stability theory [103], providing a fully determined solution and accounting for constitutional undercooling. The LGK model, which assumes a low Peclet number, was shown to agree well with microgravity experiments (dendritic growth in succinonitrile) [16] and has since been widely accepted. Nevertheless, the LGK diffusion-based solution is not consistent with terrestrial experimental data at low undercooling due to buoyancy-driven convection [16, 41]. Several models have been developed to account for thermosolutal convection [104–109]; however, the well-documented effects of melt convection on dendrite growth [110,111] remains a challenge [86]. Recent microgravity experiments with transparent alloys of Neopentyl-Glycol and (D)Camphor (NPG-DC) provided in-situ data for diffusion-dominated dendritic growth in a transparent binary alloy [44, 83]. In light of the recent microgravity experiments conducted in the NPG-DC system, this contribution aims to provide complementary terrestrial data for the NPG-DC system combined with a new computer vision algorithm for automatic identification and tracking of columnar dendrite tips.

The objectives are as follows:

- to present a new computer vision algorithm for tracking columnar dendrite tip velocities from in-situ footage of directional solidification

- to provide complementary terrestrial data for the columnar dendrite tip velocity

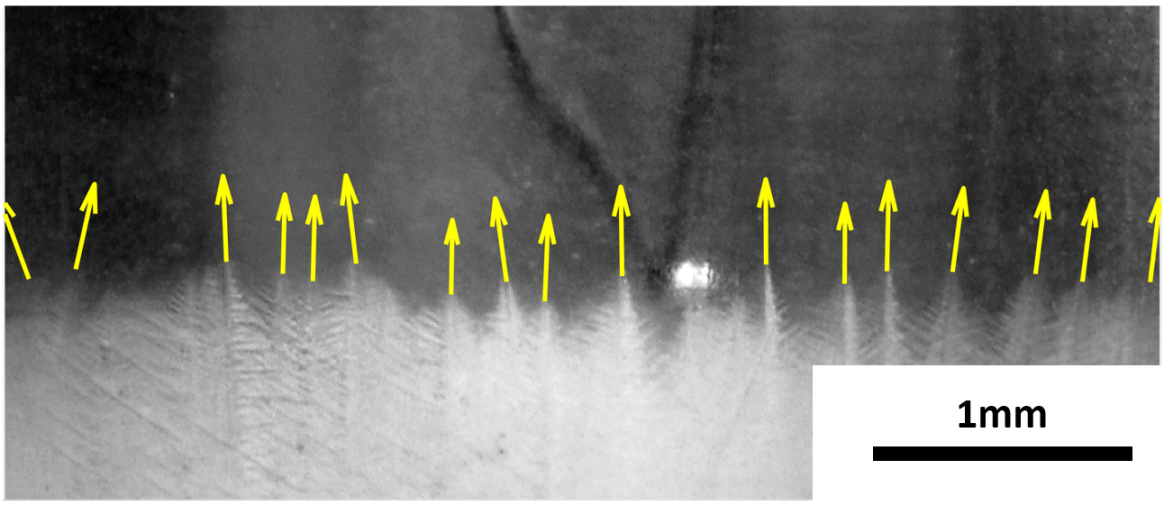

Figure 3.1: An image from an in-situ video sequence of directional solidification showing a representative result from the automatic tracking algorithm (velocity vectors). The columnar front is shown crossing an internal thermocouple used for tip undercooling measurements.

versus undercooling relationship (especially for low undercooling, data which is currently lacking), and

- to compare the terrestrial results of columnar dendrite tip velocity and undercooling with microgravity data and with theoretical models found in the literature.

3.2 Methods

An overview of the experimental apparatus and procedure is provided, followed by detailed descriptions of the tip tracking algorithm. Readers may refer to [67] for more information on the experimental setup, control and measurement. The tip tracking algorithm is used to process the in-situ image and video data to detect and track the position, velocity, and orientation of multiple columnar dendrite tips as shown, by way of example, in figure 3.1.

3.2.1 Apparatus

The experimental apparatus is comprised of a transparent sapphire crucible combined with a thermal regulation system to give hot and cold regions. The thermal regulation facilitates controlled temperature gradient, G, cooling rate, $\dot{T}$ and, hence, liquidus isotherm speed, v_L. Sapphire was chosen as the crucible material because it is optically

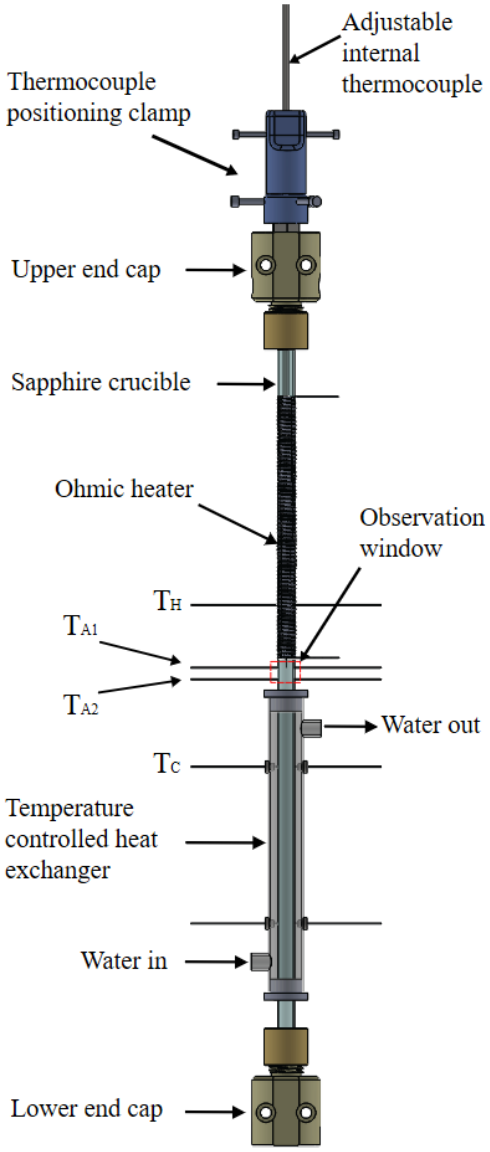

Figure 3.2: Technical illustration of apparatus with the observation window shown in the centre

transparent, allowing optical visualisation of the top of the mushy zone and, due to its high thermal conductivity (40 W/mK), facilitates heat transfer to and from the material with low temperature difference (< 1 K) across the crucible wall.

Figure 3.2 shows a technical illustration of the experimental facility. It consists of a vertical sapphire crucible of 450mm length, with an inner diameter of 8mm and an outer diameter of 10mm. An Ohmic heater in the upper section consists of a coiled nichrome wire connected with a power supply (Automatik EA-PSI-8360-10T DC). The nichrome wire is wrapped tightly around the outer tube wall with a thermally conductive silicone layer to provide adequate thermal contact and electrical isolation. A dedicated computer system controls T_H using a power supply with an EA-IF-U1

interface card and proportional-integral control loop in LabView®. Heat is extracted from the lower section with a 170mm long tube-and-shell type heat exchanger. A Julabo A40 precision chiller in series with a pump supplies chilled water to the heat exchanger with initial controlled setpoints followed by controlled cooling at a rate of T_C within the range of 0.2 to 0.6 K/min being possible. Two thermocouples that pass into the heat exchanger are embedded into the wall of the sapphire crucible. These two thermocouples provide temperature measurements of the crucible wall inside the heat exchanger, the average of which is designated as T_C. T_H is controlled to be ramped down at the same cooling rate as $\dot{T}_C = dT/dt$ in order to maintain a constant temperature gradient $G = (T_H - T_C)/z_{HC}$, with z_{HC} being the axial distance between thermocouples, T_H and T_C. Thus, for a fixed G specified by the user, the setpoint T_H for the controller is calculated as:

$$T_H = T_C + Gz_{HC} \tag{3.1}$$

Pairs of 0.5mm diameter blind holes have been drilled at several heights along the crucible wall into which T-type thermocouples have been inserted with an essential amount of thermal adhesive. Figure 3.2 shows four temperature measurement locations designated as T_H, T_{A1}, T_{A2}, and T_C. Each location has a pair of thermocouples at the given height where the average temperatures of each diametrically-opposed thermocouples pair are used. T_C and T_H are controlled to set the temperature gradient and cooling rate in the baffle zone (as described previously) while T_{A1} and T_{A2} are used to provide the measured temperature gradient, G, and measured cooling rate, $\dot{T}$, in the observation window. An optional temperature probe can be passed vertically downwards into the crucible through an O-ring seal on the upper end-cap. The temperature probe consists of 3mm diameter stainless steel tube housing with an 80 µm T-type thermocouple with Teflon® sheath that extends 30mm from the stainless steel tube.

A Canon EOS 200D camera with a Navitar 3x – 10x zoom lens is mounted with its optical axis orthogonal to the observation window. The synchronisation of the camera and computer clocks facilitates simultaneous measurement of the temperatures

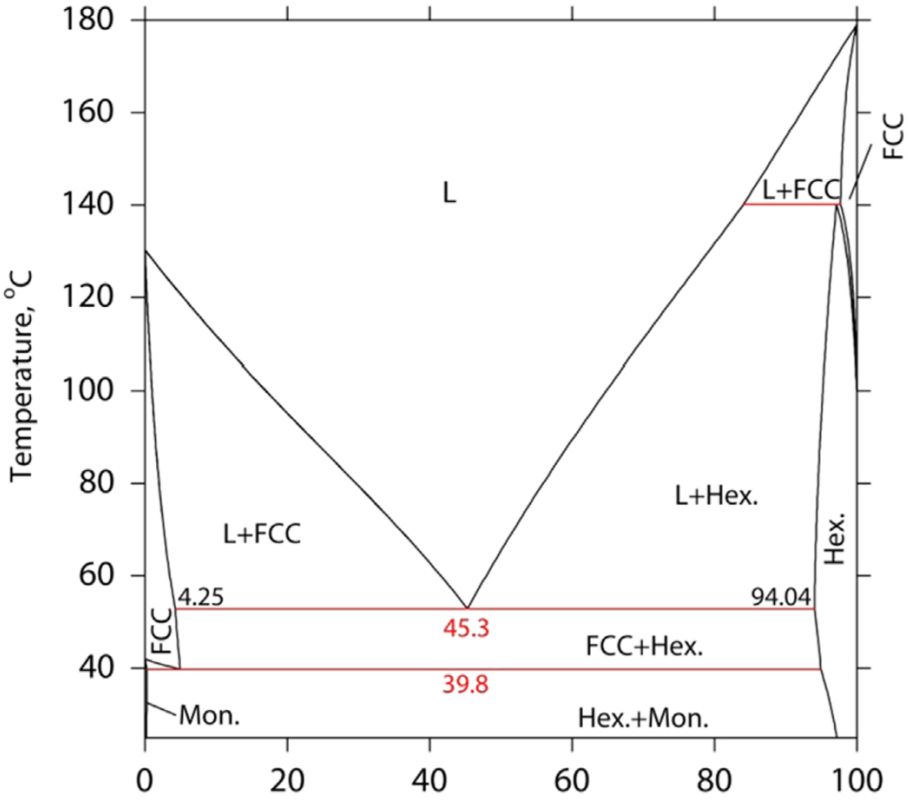

Figure 3.3: Phase diagram of the NPG-DC system [112, 113].

and solidification parameters combined with in-situ microscopic videography of the solidification. As solidification at low undercooling is a relatively slow process, images are captured at a frame rate of 0.5 fps and stored with a lossless png file format.

3.2.2 Materials

The alloy materials, NPG and DC, were supplied by Sigma Aldrich. Figure 3.3 shows the alloy system's phase diagram (from [112,113]); the alloy system has a eutectic composition at C_E=45.3wt.% and is a CET former. The present work investigates columnar growth using a hypoeutectic composition of C_0=35wt.%. As NPG is hygroscopic, the transparent alloy was prepared in a sealed glove box under Argon atmosphere (<5ppm H_2O). The batch consisted of 40.02g of neopentyl glycol, and 21.53g of (d)Camphor weighed using a KERN Analytical balance (0.1mg uncertainty). The materials were heated and mixed in an Erlenmeyer flask with a perforated subaseal® septum on top to contain sublimated materials and provide pressure compensation. The alloy was transferred from the glovebox in a high-temperature gas-tight glass syringe. The sapphire crucible was flushed with dry air, and the liquid NPG-35wt.%DC was injected

through a Leur Lok valve on the lower end-cap (not shown). The crucible was then filled to the upper level of the Ohmic heater with an excess of argon from the glove box filling the remaining volume of the crucible above the heater.

3.2.3 Growth Experiment Procedure

This work investigated directional solidification occurring vertically upward from the cooled solid zone following initiation of a controlled ramp-down of set point temperatures T_C and T_H. To investigate the relationship between columnar dendrite tip velocity and undercooling, a total of six tests were conducted with different isotherm velocities by varying the setpoint cooling rates, $\dot{T}_H$ and $\dot{T}_C$, and temperature gradient, G. In each test, the newly developed computer vision algorithm automatically tracked the columnar dendrite tips and, when dendrites crossed the internal thermocouple, this provided instantaneous measurement of the columnar dendrite tip velocity with undercooling.

For the present experiments, the test material in the crucible above the cooled heat sink region was brought into the liquid phase by increasing the Ohmic heater's temperature to 120^{o}C. To ensure a homogenous initial composition in the liquid melt before any given test, the baffle zone was heated with a heat gun and the Ohmic heater was temporarily turned off to induce convective mixing for a period of 5 minutes. The set points on the thermocouple pairs T_H and T_C were then adjusted such that the solidification front was just below the observation window and maintained for at least 40 minutes to allow the solidification front to reach the liquidus isotherm, just inside the observation window. Two images of the solidification front were routinely captured five minutes apart and compared to confirm that the solidification front position was stationary. The adjustable internal thermocouple was manually traversed vertically downwards to the columnar front and clamped at the solidification front for two minutes to confirm the liquidus temperature recording. The probe was then brought back to the top of the observation window before commencing with directional solidification. At this point in any of the experiments, ramp down cooling was initiated, and optical imaging commenced. Progression of the mean dendrite tip velocity for each test was

Table 3.1: Imposed processing parameters

Test Number	Cooling Rates (K/min)	Temperature Gradient (K/cm)
I	0.16	23.3 ± 1.80
II	0.30	23.58 ± 1.83
III	0.45	23.64 ± 1.83
IV	0.16	16.79 ± 1.80
V	0.30	16.55 ± 1.80
VI	0.45	16.57 ± 1.41

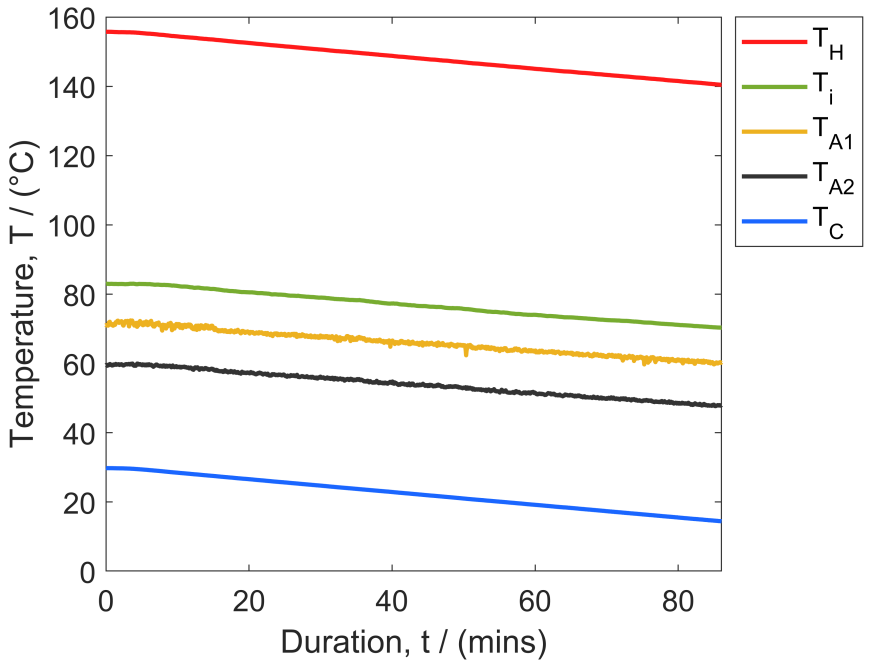

Figure 3.4: Plot of temperature versus time from test number 1 showing representative cooling curves obtained during experiments.

provided by the computer vision algorithm and was used to confirm if the growth rate had achieved a steady state.

Two temperature gradients of 16.6 K/cm and 23.5 K/cm, and three cooling rates of 0.16 K/min, 0.30 K/min and 0.45 K/min were applied during experiments. The range of temperature gradient, G_i, reflects some limitations of the experimental facility; at $G_i < 15K/cm$, the imposed temperature gradient starts to destabilise, whereas $G_i > 24K/cm$ leads to boiling in the heater section. Additionally, a maximum cooling rate of $\dot{T} = 0.45K/min$ was used because equiaxed growth typically dominates at higher cooling rates. The range of cooling rates was selected to study dendrite growth over a range of dendrite tip velocities and undercoolings. Table 3.1 lists the thermal processing

parameters for the six experiments, which provided a corresponding range of isotherm speeds between 1.13 and 4.53 µm/s. The measured cooling rate, $\dot{T}$, being the average of $\dot{T}_{A1}$ and $\dot{T}_{A2}$, was recorded. The internal temperature gradient, G_i, was provided after a calibration correction as detailed in previous work [67]. The calibration correction equation used was $G_i = 1.27G_e - 0.22$, where G_e is the measured temperature gradient on the wall of the sapphire crucible calculated using information from T_{A1} and T_{A2} and based on the spacing between the thermocouples.

3.2.4 Columnar Tip Tracking

The computer vision algorithm works by generating a contour at the top of the mushy zone for a given image of the video sequence (see figure 3.6 (c)). The contours consist of peaks and valleys around the columnar dendrites at the top of the mushy zone, similar to a grain envelope used in mesoscopic solidification modelling. Determination of local maxima from each contour yields a set of points, $\boldsymbol{p}_{ik}(x, y, t_i)$, which includes columnar tip positions. Figure 3.5 summarises the sequence of steps in the columnar tip tracking algorithm. They comprise three main stages (i) pre-processing, (ii) contouring and (iii) tip-data extraction. Each stage is described next.

Pre-processing

At a given time, t, two high-resolution 8-bit grayscale images, denoted I_t and $I_{t+\Delta t}$ (separated by a nominal time Δt), are selected for analysis. To preclude any vibrations arising in the video data, I_t and $I_{t+\Delta t}$ are passed through an antishake algorithm that registers each frame to the first frame in the video sequence I_{t0}. The antishake algorithm detects feature points in a given frame using the MATLAB® implementation of the minimum eigenvalue algorithm developed by Shi and Tomasi [92] and then matches them with feature points in I_{t0} to provide Euclidean image transformations when necessary. Automatic front-tracking (see previous work [67]) provides an average position of the columnar front, y_f. Using y_f, the algorithm crops input images to a height of $y_f \pm h$ and a width of approximately 6mm centred on the crucible vertical axis. The user nominally defines h based on experience or using trial and error for optimum

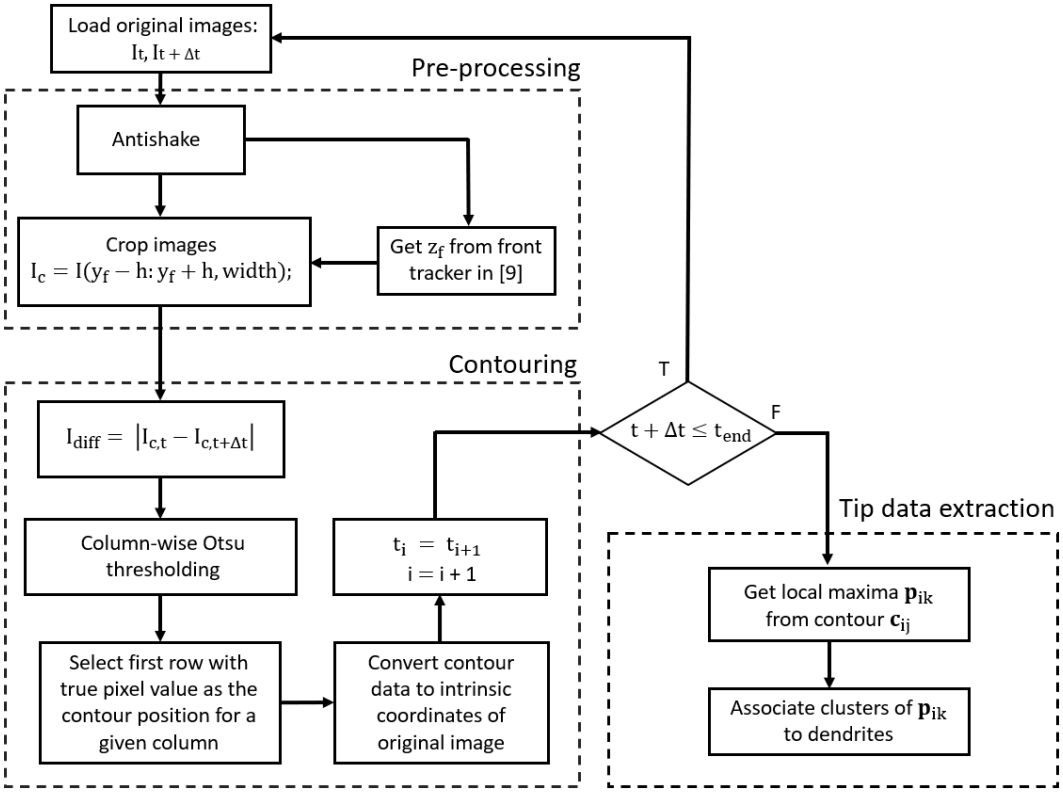

Figure 3.5: Flow chart of columnar tip tracking algorithm

results, typically 5% of the image height (rounded to the nearest integer pixel position). For test No. VI, h was set to 7% to capture the solidification front's broader range. When $y_f \pm h$ exceeds the image domain; the exceeding bound is reassigned at the top or bottom of the image as required. The cropped images, $I_{c,t}$ and $I_{c,t+\Delta t}$, are then passed onto the contouring stage of the algorithm.

Positions $\boldsymbol{p}_{ik}$ use two frames of reference, the intrinsic image coordinates and the world coordinates, which are indicated with subscripts p and w, respectively. The intrinsic image coordinates are defined by discrete pixel indices with column and row numbers corresponding to the x and y positions, respectively. Thus, the pixel position (1,1) is located at the centre of the image's upper-leftmost pixel with the y-axis pointing downwards [114]. A single reference on the first image, $\boldsymbol{p}_{ref,p}$ and known width of the crucible, $w_w = 1 \times 10^{-2} m$ facilitated conversions from intrinsic image coordinates to world coordinates as follows:

$$\boldsymbol{p}_w = \frac{w_w}{w_p}[(x_p - x_{ref,p})\boldsymbol{i} - (y_p - y_{ref,p})\boldsymbol{j}] \tag{3.2}$$

$\boldsymbol{p}_{ref,p}$ was manually selected at the height of T_{A1}, with x position corresponding to

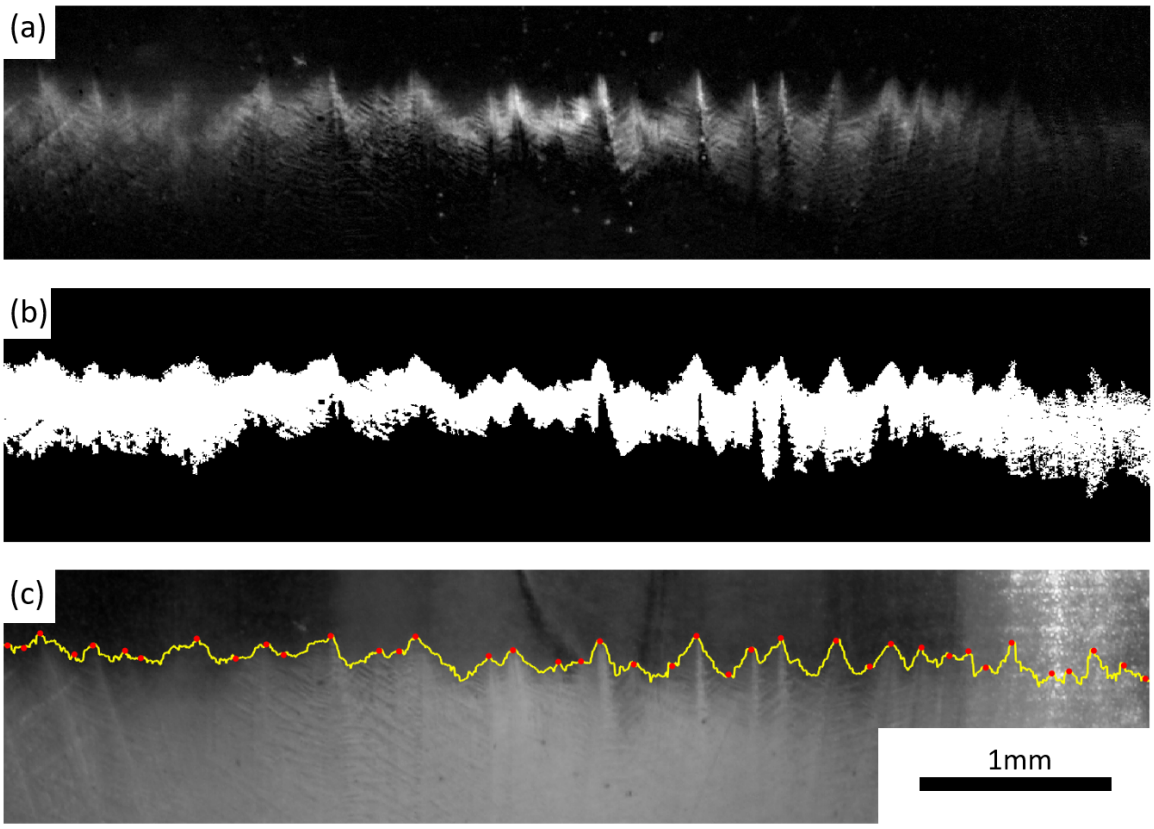

Figure 3.6: Images illustrating steps in the contouring phase of the tip tracking algorithm: (a) absolute difference between two successive images, denoted I_{diff}, (b) binary image output from column-wise Otsu thresholding of I_{diff}, and (c) cropped input image $I_{c,t+\Delta t}$ with resulting contour overlay (yellow) delineating the liquid and mushy zones. Local maxima are shown as red dots.

a 2mm inset from the left wall of the sapphire crucible (in line with the first column of the cropped images). Eq. 3.2 gives the position in the world reference frame from the ratio of the known width, w_w, in the world frame to the pixel width, w_p, in the image frame. Position data are nominally stored as intrinsic coordinates of original input images and converted using Eq. 3.2 as required. For clarity, references to the position are herein described in world coordinates, i.e. with origin corresponding to $\boldsymbol{p}_{ref}$ and the y-axis pointing vertically upwards.

Contouring

Figure 3.6 (a) to (c) illustrate the steps involved in contouring the solidification front. Firstly, background removal by frame differencing equation 3.3 provides an image that highlights newly formed solid between two frames:

$$I_{diff} = | I_{c,t+\Delta t} - I_{c,t} | \tag{3.3}$$

Figure 3.6 (a) shows an example of the resulting 8-bit grayscale image I_{diff} (contrast stretched for visualisation). Taking smaller fixed Δt reduces the presence of unwanted artefacts and improves the detail of the columnar front in I_{diff} for use in contouring.

Column-wise Otsu thresholding of I_{diff} generates a binary image used to determine the solidification front's contour (see figure 3.6 (b)). The Otsu algorithm automatically selects an optimal threshold grey-level for separating input pixels into two classes by minimising the weighted sum of within-class variances [115]. Otsu thresholding works well for input images with a bimodal histogram; however, it is susceptible to noise and non-uniform illumination [116]. As Figure 3.6 (a) shows, pixel intensities in I_{diff} are spatially dependent with dendrites having higher intensity at the centre as compared with the edges. The subroutine implements column-wise Otsu thresholding, ensuring that the threshold captures as much detail of the columnar front as possible. The threshold's output is a binary image representing the newly formed solid between the two input frames. Figure 3.6 (b) shows the resulting binary image with pixels that passed the Otsu threshold shown in white (i.e., with a binary value of 1) and pixels failing the threshold are shown in black (i.e., with a binary value of 0). The algorithm filters white areas in figure 3.6 (b) with less than 2000 connected pixels (8-connected) to remove small defects or spurious features from the threshold. The first pixel in each column of the binary image (figure 3.6 (b)) that passes the threshold defines the location of the contour, c_{ij}, where i indexes over the timesteps of the video sequence and where each timestep has j points, one for each column of the cropped image. Figure 3.6 (c) shows the resulting contour overlaid on $I_{c,t+\Delta t}$. The figure includes the local maxima of the contour, which are used for further processing steps.

Tip-Data Extraction

Local maxima of the contours at a given timestep can indicate tip positions of columnar dendrites. However, the initial data consists of numerous false positives, and further elimination processing is needed. A subroutine extracts and groups the data in $\boldsymbol{p}_{ik}$

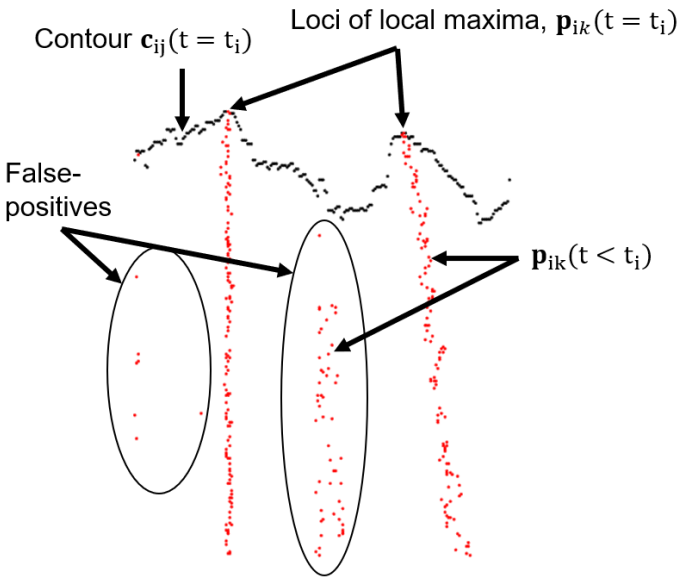

Figure 3.7: Close up view of contour (black) and loci of the local maxima from both the current timestep and a selection of previous timesteps.

into separate clusters associated with each columnar dendrite. Since primary columnar dendrites grow uniaxially, the subroutine classifies data points by approximating straight lines through the locus of tip positions of a given primary columnar dendrite. Figure 3.7 shows a close up of the contour at a time t_i, and loci of the local maxima, $\boldsymbol{p}_{ik}$, from the current timestep (in black) and a selection of previous timesteps (in red). Input points, $\boldsymbol{p}_{ik}$, can consist of over 100 dendrites requiring classification, with up to half of the points being outliers. Classical parameter estimation methods, such as least-squares optimisation, are susceptible to outliers and have insufficient robustness. More robust line-estimation techniques such as the Hough transform or an iterative RANSAC approach were evaluated. However, while both methods were adapted to classify multiple dendrites in $\boldsymbol{p}_{ik}$, most dendrites were only partially classified, and these methods resulted in significant false-positive groupings. A bespoke subroutine has been developed which block processes subsets of $\boldsymbol{p}_{ik}$ with a RANSAC-type algorithm. After associating each subset's points with a dendrite (or not, as the case arises), the subroutine merges overlapping groups related to a single dendrite. Similar to RANSAC, the bespoke subroutine uses as small an initial data set as feasible and enlarges this set with consistent data when possible. Outliers are points falling outside an error threshold, d, where d defines the maximum deviation attributable to noise. Here, we set the threshold to approximately one-tenth of the observed primary dendrite

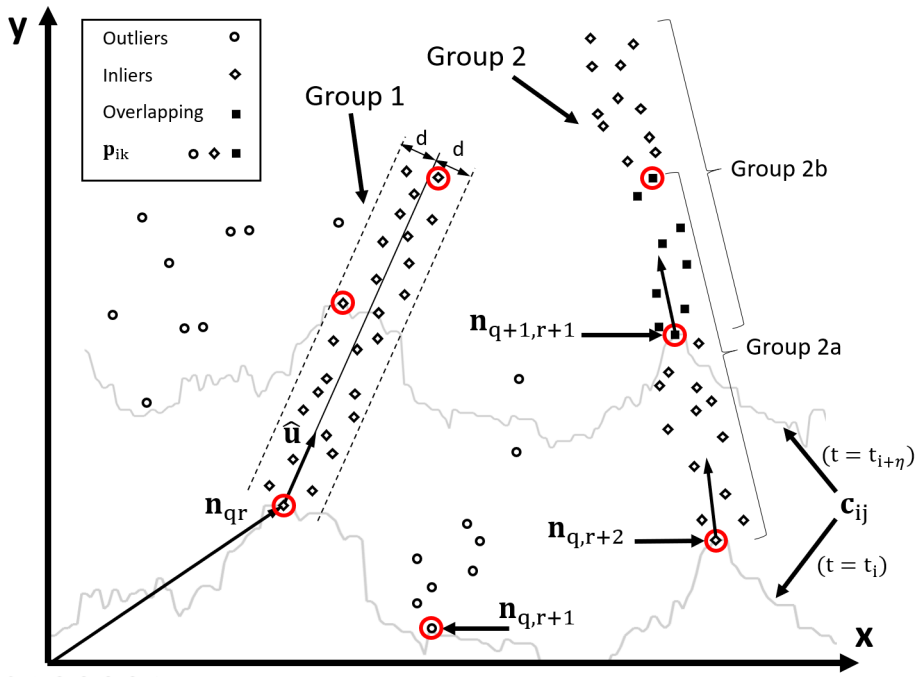

Figure 3.8: Schematic illustration of grouping algorithm showing a subsection of $\boldsymbol{p}_{ik}$ with two contours $\boldsymbol{c}_{ij}$ and 7 Hypothetical Seed Nodes (HSN's). Group 1 shows a hypothetical linear model with direction vector, $\hat{\boldsymbol{u}}(\theta)$, hypothetical seed node $\boldsymbol{n}_{qr}$ and theshold perpendicular distance d for accepting data. θ is optimised to obtain the max number of inliers over the set $\theta \epsilon N[1, 180]$. Subgroups 2a and 2b combine into one compound group as $N_{overlap} < N$.

arm spacing.

The subroutine selects initial nodes from $\boldsymbol{n}_{ik}$ at intervals separated by m timesteps. These nodes provide a hypothetical starting point from which a group of data may be classified as being associated with a dendrite or not. A sample point is then termed a Hypothetical Seed Node (HSN), and denoted, $\boldsymbol{n}_{qr}$ (see figure 3.8) where $\boldsymbol{n}_{qr} = \boldsymbol{p}_{(\eta(i-1)+1,k)}$, i.e., HSNs occur at multiples of η timesteps.

For each HSN, the subroutine operates on a subset of points ahead of the node as defined in Eq. (6). The function f_{qrs} in Eq. (4) returns the sum of inliers for a given hypothetical straight-line model. By iterating through θ, the hypothetical model with the largest number of inliers for a given node is obtained. If a threshold number of points fall within the threshold perpendicular distance, d, from the hypothetical model, the inlier points are then accepted as being associated with a dendrite. The sum of points within a threshold perpendicular distance, d, to a given theoretical straight-line model and HSN is defined as follows:

$$f_{qrs}(x) = \begin{cases} 1, & \text{if } \| (\boldsymbol{p}_{ik} - \boldsymbol{n}_{qr}) \times \hat{\boldsymbol{u}}(\theta_s) \| \leq d \\ 0, & \text{otherwise} \end{cases} \tag{3.4}$$

where $\hat{\boldsymbol{u}}(\theta)$ is a direction vector for a hypothetical straight-line model given by:

$$\hat{\boldsymbol{u}}(\theta) = Cos(\theta_s)\boldsymbol{i} + Sin(\theta_s)\boldsymbol{j} \tag{3.5}$$

The algorithm operates on a subset of points defined relative to the current HSN. Equation 3.5 defines indices i and k for the current HSN ($\boldsymbol{n}_{qr}$) such that all points of $\boldsymbol{p}_{ik}$ are: (i) within a radial distance, r, from $\boldsymbol{n}_{qr}$; (ii) have a greater or equal $\boldsymbol{j}$ component, and (iii) exist for all values of t in the interval $t_i \leq t \leq t_{i+2\eta}$

$$i,k = \{\boldsymbol{n}_{qr}(t) \mid \forall (i \wedge k)(\| \boldsymbol{p}_{ik} - \boldsymbol{n}_{qr} \| \leq r) \wedge (\boldsymbol{p}_{ik} \cdot \boldsymbol{j} \geq \boldsymbol{n}_{qr} \cdot \boldsymbol{j}) \wedge (t_i \leq t \leq t_{i+2\eta})\} \tag{3.6}$$

Figure 3.8 shows seven HSNs (circled in red) and illustrates the subsets of data for the hypothetical nodes $\boldsymbol{n}_q r$, $\boldsymbol{n}_{q+1,r}$, $\boldsymbol{n}_{q,r+1}$, $\boldsymbol{n}_{q+1,r+1}$, and $\boldsymbol{n}_{q+1,r+2}$ which, in combination with $\hat{\boldsymbol{u}}$, define the hypothetical straight-line models. HSNs occur at every η timesteps, while (subject to equation 3.6) subsets of $\boldsymbol{p}_{ik}$ associated with a given HSN spans 2η timesteps providing an overlap between groups. The subroutine crosschecks the accepted data from time-adjacent groups for overlap, thus providing a criterion for merging the groups. Figure 3.8 shows merging of two subgroups, 2a and 2b, where a threshold number of points overlap. Dendrite clusters consisting of 50 points or less are omitted from further processing steps. Position data clusters are sorted according to time, smoothed with a second-order Savitsky-Golay filter with a 50-point window, and linear interpolation of x and y with respect to time is used to fill any missing data points. Finally, dendrite orientation, α, is obtained by orthogonal least squares regression of the x and y coordinates for a given dendrite cluster, while the magnitude of the dendrite tip velocity is determined by

$$v_{i+2,k} = \frac{\| \boldsymbol{p}(t_{i+4}) - \boldsymbol{p}(t_i) \|}{t_{i+4} - t_i} \tag{3.7}$$

In summary, the grouping process works as follows:

(i) Select a seed node, $\boldsymbol{n}$, at time t_i

(ii) Select a subset of points in $\boldsymbol{p}_{ik}$ near the seed node, i.e., points within a radial distance r from $\boldsymbol{n}$, with j components greater than or equal to that of $\boldsymbol{n}$, and over a time interval $t_i \leq t \leq t_{i+2m}$

(iii) Maximise $f(\boldsymbol{n}_{qr}, \theta_s)$ by iterating through $\theta,\ \forall\theta\ \epsilon\ N[1, 180]$.

(iv) Check time-adjacent groups for the merging criterion.

The pre-processing, contouring and tip-data extraction algorithm allows tips to be tracked with their velocity and orientation being measured. Growth vectors are applied to the moving tips within the video data on a frame-by-frame basis, as shown in the supplementary material. These videos give a clear visual reference for the growth rate of each identified dendrite tip. Given that a stationary thermocouple was inserted inside the crucible (and within the observation window) to measure the melt temperature, it was possible to observe the moment that the tips crossed over the thermocouple. Hence, this feature facilitated the instantaneous tip temperature measurement as the solidification front crossed the thermocouple.

3.3 Results

Six directional solidification test scenarios are presented using a transparent alloy NPG-35wt.%DC. The apparatus facilitated directional solidification with a controlled temperature gradient, cooling rate and equilibrium liquidus isotherm speed (for a more detailed description of the apparatus, see [67]). Table 3.1 lists the thermal processing parameters for all six experiments covering a range of isotherm speeds between 1.13 and 4.53 μm/s. In-situ microscopic video sequences of all six test cases were processed with the newly developed computer vision algorithm. To appreciate the advantage of an automatic detection system, a total of 385 columnar dendrite tips were tracked over all six tests. Table 3.2 summarises the processed results for each test, including the total number of tips tracked (N_{total}), the number of tips crossing the internal thermocouple ($N_{crossing}$), the mean tip velocity ($\bar{v}_t$), the mean undercooling ($\Delta\bar{T}$) for tips that

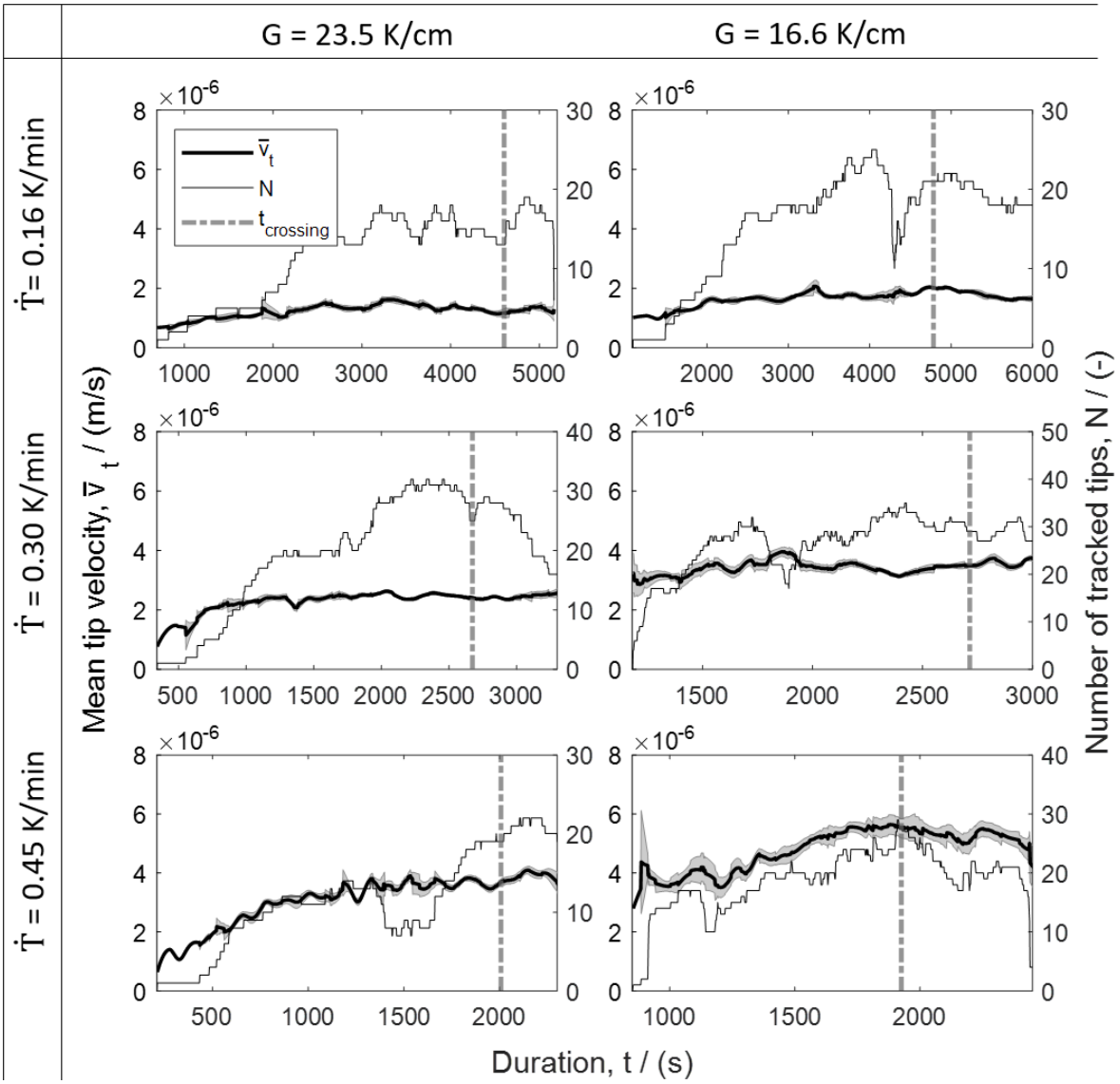

Figure 3.9: Mean dendrite tip velocity, $\bar{v}_t$, and number of tips, N, tracked versus time for tests I to VI. The graphs show mean velocities with two standard errors applied over the interval, The vertical dashed lines indicating average time, $t_{crossing}$, when dendrite tips crossed the internal thermocouple.

crossed the internal thermocouple, and their standard uncertainties ($u_{\bar{v}_t}$ and $u_{\Delta\bar{T}}$).

As mentioned, the NPG-DC eutectic alloy has been in microgravity investigations to study columnar growth structures and columnar to equiaxed transitions [44]. Figure 3.11 shows results of dendrite tip velocity and undercooling from the present work from a total of 95 dendrite tips crossing the internal thermocouple. Test numbers I to III are shown with triangle, circle, and square markers with white marker face colour, while test numbers IV to VI are shown with triangle, circle, and square markers with grey marker face colours. Figure 3.11 also compares the present work with the TRACE experiment conducted in microgravity with otherwise similar processing parameters

Table 3.2: Summary of columnar dendrite tips tracked during each test detailing the average tip velocities and undercoolings, and their associated standard uncertainties.

Test no.	N_{total}	$N_{crossing}$	$\bar{v}_t$	$u_{\bar{v}_t}$	$\Delta\bar{T}$	$u_{\Delta\bar{T}}$
	#	#	$\mu m/s$	$\mu m/s$	K	K
I	47	6	1.18	0.03	0.95	0.04
II	56	21	2.38	0.02	2.29	0.02
III	42	11	3.62	0.09	2.95	0.05
IV	62	14	1.98	0.03	3.43	0.07
V	97	27	3.54	0.05	5.61	0.03
VI	81	16	5.40	0.14	5.53	0.05

(NPG-37.5wt.%DC and G = 16.5 K/cm). Solidification studies on sounding rocket missions are typically performed under transient conditions and higher undercooling to allow appreciable growth during the 4-5 minute microgravity window. Due to relaxed time constraints in terrestrial experimentation, the current test cases cover the low undercooling range to fill this knowledge gap. In addition to the experimental data, figure 3.11 shows the results of the Lipton Glicksman-Kurz(LGK) dendrite model but with the stability parameter, σ^*, adjusted after a data-fitting exercise. As described in the methodology section, the LGK model, which is derived on a solutal diffusion basis, is fitted to the microgravity datasets. Figure 3.9 shows the mean dendrite tip velocity, $\bar{v} \pm k u_{\bar{v}_t}$). The experimental standard deviation of the mean, ($u_{\bar{v}_t}$), is defined by

$$u_{\bar{v}_t} = \sqrt{\frac{1}{N(N-1)} \sum_{i=1}^{N} (\bar{v}_t - v_i)^2} \tag{3.8}$$

and is determined for N dendrite tips tracked at a given time. Expanded uncertainty intervals are provided with a coverage factor of k=1.96 and hence 95% confidence interval. Figure 3.9 shows the progression of the number of tips tracked, N, over time for the six tests. A vertical dashed line indicates the mean time, $\bar{t}_{crossing}$, that dendrite tips crossed the internal thermocouple.

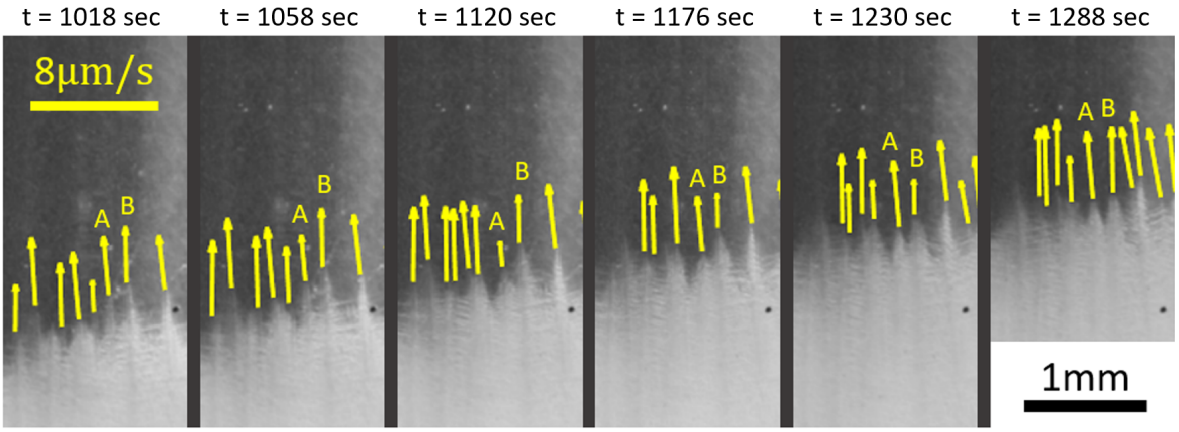

Figure 3.10: Image sequence from test VI shows competitive interplay between two neighbouring dendrites. Tip A slows down falling behind tip B, then B slows down and A speeds up until they are side by side.

3.4 Discussion

Results are presented using a new computer vision algorithm giving the growth rates and undercooling levels of multiple columnar dendrite tips during directional solidification of bulk transparent alloy NPG-35wt.%DC. Six directional solidification tests were conducted with a controlled temperature gradient, cooling rate, and hence isotherm speed. The computer vision algorithm tracked a total of 385 columnar dendrite tips. In the following section, key points are discussed: (i) the performance and general results of the computer vision algorithm, (ii) the comparison of current tip velocity and undercooling data to relevant microgravity data, and (iii) and the comparison of experimental data to theoretical LGK and modified LGK models of dendrite tip velocity.

Figure 3.9 provides a summary overview of all the dendrite tip tracking data with mean dendrite tip velocity, $\bar{v}_t$ ($\pm$2SEM) and the total number of tips tracked, N, at any given time, t. Generally, the tip tracking shows an initial transient phase, with $\bar{v}_t$ tending to increase until quasi-steady growth conditions are attained with $\bar{v}_t$ becoming approximately fixed. Figure 3.11 shows the instantaneous dendrite tip velocity and associated undercooling measured at the moment when the dendrite tips crossed the internal thermocouple, T_i. Figure 3.9 shows the average time that dendrite tips crossed the internal thermocouple, $t_{crossing}$. In all cases, dendrite tip and undercooling measurements were captured during the quasi-steady growth phase. The numbers of

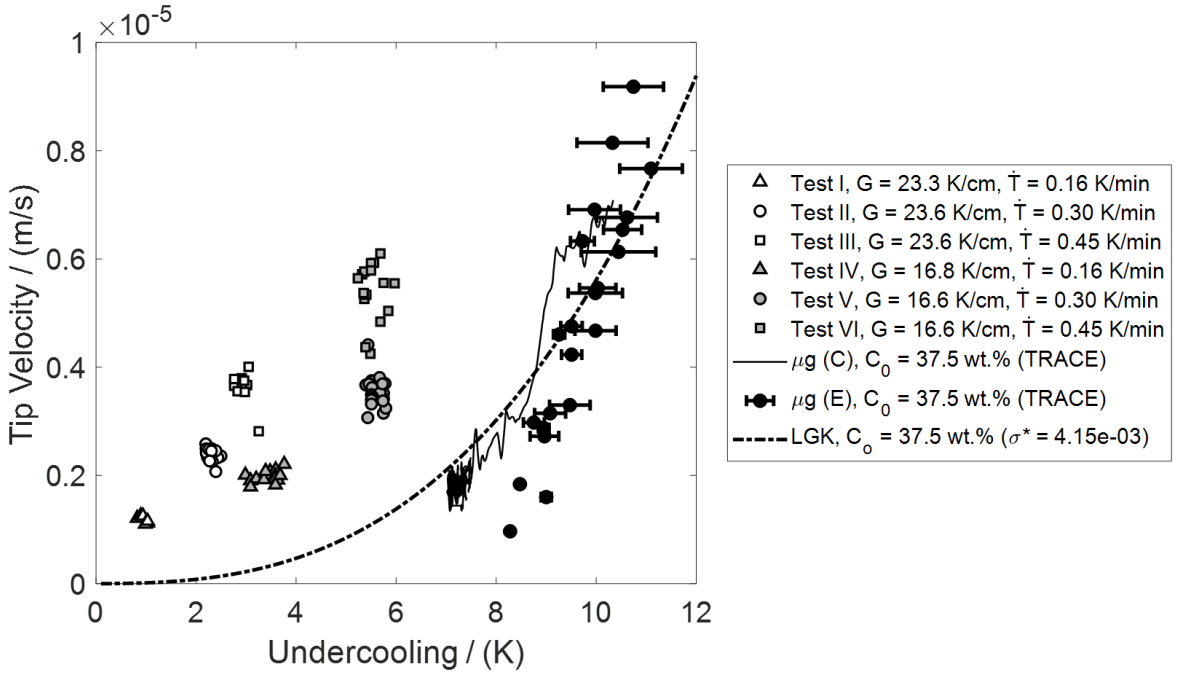

Figure 3.11: Dendrite tip velocity versus undercooling for the present work (test cases I to VI, C_0 = 35wt.%, (Tests I to VI, respectively) compared with measurements from the TRACE microgravity experiment (C_0 = 37.5wt.%, C- columnar, E - equiaxed) and the LGK growth law.

dendrite tips involved at the thermocouple crossing stage in all cases are within the range from 15 to 30 tips. Hence, reasonable statistical information is expected.

Velocity vectors in the in-situ video data (refer to the supplementary materials) show oscillations of individual dendrite tip velocities; in some cases, there is an interplay between neighbouring dendrite tips where one races out ahead, and then the other catches up. In general, the fluctuations in dendrite tip velocity are out of phase. Figure 3.10 clearly shows the interplay between adjacent columnar dendrites (annotated A and B). Initially, dendrite A fell behind (frames 2 - 3) then increased in growth rate (frame 4) while B simultaneously slowed down (frames 4 – 5), allowing dendrite A to catch up to dendrite B. Since there is an imposed temperature gradient, upwards solidification is usually deemed thermally stable. This is because density typically decreases with temperature, and temperature increases in the vertical direction. The effect of gravity on a fluid with its highest density liquid at the solid-liquid interface suppresses thermal convection ahead of the front. The out-of-phase growth oscillation between dendrites is likely due to the solutal interaction and alternating changes in the composition gradient in liquid, G_C, ahead of the tips. The solute, D-camphor, is less dense than NPG, so the

partitioning (rejection) of solute into the liquid causes the density to be lower ahead of the tips and this leads to convection due to solutal instability. Hence, the solidification is thermally stable but solutally unstable, and this could lead to fluctuations in the solute field ahead of the dendrite tips. It has been shown elsewhere [117] that unsteady or oscillatory growth can occur because of changes in the solute field ahead of the dendrite even though thermal conditions are stable. Even though evidence shows that the dendrite growth has periods of acceleration followed by deceleration, the net effect is growth at the average rate as given by $\bar{v}_t$. Since the solutal diffusion length (17.4 μm), is much less than the distance between dendrites A and B (approx. 145 um based on measurement in ImageJ), the interaction which resulted in a significant variation in dendrite tip velocity, was most likely related to thermosolutal flow.

However, figure 3.9 III shows periodic variations in the mean tip velocity in excess of the measurement uncertainty. The periodicity in $\bar{v}_t$ is evidence of competitive growth between neighbouring dendrites; impingement of the faster misaligned tips which are subsequently not being tracked and thus decrease $\bar{v}_t$t. Dendrite tip velocity may decrease on the scale of the solidification front due to solute piling at the dendrite tips. Subsequent thermosolutal convection may replace the solute enriched liquid with a lower composition liquid causing dendrite tip velocity to accelerate again. In test III, the effect could be occurring across the scale of the solidification front, thus affecting the mean tip velocity.

3.4.1 Theoretical Models

The Lipton-Glicksman-Kurz model of dendrite growth is based on the Ivantsov formulation for the solute field around a parabolic dendrite tip. Taking into account the diffusion field around a dendrite tip, the dimensionless supersaturation, $\Omega = \frac{C^* - C_0}{C^*(1-k_0)}$, is defined as:

$$\Omega = Pexp(P)E_1(P) \equiv Iv(P) \tag{3.9}$$

where P is the solutal Péclet number given as $P_c = VR/2D$, and E_1 is the exponential integral function. A solution to this equation requires a stability criterion which is given

by:

$$R = \left\{ \frac{\Gamma}{\sigma^*(mG_C - G)} \right\}^{\frac{1}{2}} \tag{3.10}$$

The solutal gradient in the liquid at the tip interface is given as:

$$G_c = \frac{2P_C C^*(1 - k_0)}{R} \tag{3.11}$$

The LGK model requires an iterative solution to the preceding set of equations, and the undercooling at the tip is taken as the sum of the solutal and curvature undercooling terms. The stability parameter, σ^*, determines the operating point for the dendrite tip. Originally, the LGK model used a general parameter of $1/4\pi^2 = 0.025$; however,experimental evidence is needed to determine the alloy system's actual parameter in question [118]. Sturz and Zimmermann [44] determined the stability parameter for NPG-37.5wt.%DC by fitting the LGK model to microgravity data. New information has come to light on the diffusivity of D-Camphor in NPG [113] (with $D_L = 9.7 \times 10^{-11} m^2/s$). Applying the same fitting exercise as Sturz and Zimmermann but with the updated diffusivity gives a stability parameter of $\sigma^* = 4.15 \times 10^{-3}$.

To account for the effect of fluid flow around a dendrite tip, Cantor and Vogel [104] proposed the existence of a diffusional boundary layer of finite length, δ, around the tip. The approach of assuming a finite boundary later is comprehensively reviewed by McFadden and Browne [108], and adaptation to the LGK model is the new term in the supersaturation equation that accounts for the boundary layer thickness as follows:

$$\Omega = Pe^P \left[E_1(p) - E_1\left(P\left(1 + \frac{2\delta}{R} \right) \right) \right] \tag{3.12}$$

Hence, different boundary layer thickness values can be assumed a priori and included in the version of the LGK model adapted for fluid flow.

Figure 3.11 compares the terrestrial tip velocity and undercooling measurements on binary alloy NPG-35wt.%DC with similar microgravity data from the TRACE campaign [44]. The TRACE experiment used a temperature gradient of 16.5 K/cm, an initial cooling rate of 0.2K/min (columnar growth) followed by a cooling rate of

2K/min to induce a CET. In the TRACE campaign, Sturz et al. compared microgravity results of dendrite tip velocity and undercooling with the theoretical models of Lu-Hunt [119], Burden-Hunt [120], Lipton-Glicksman-Kurz [102, 121] and Kurz-Giovanola-Trivedi [122]. In general, the models were not capable of predicting the experimental results; however, the LGK model (see Figure 3.11) showed good agreement with the experimental data [44]. For this reason, the present work only considers the LGK model given parameter values obtained in the TRACE experiment and with the adaptation for fluid flow (LGK-CV). The boundary layer thickness, δ, is used as a fitting parameter.

Three out of the six tests presented in this manuscript (see Table 3.1 for test no. IV-VI) were conducted at a temperature gradient of 16.5 – 16.8 K/cm, thus providing the best comparison to TRACE (16.5 K/cm with 37.5wt.% composition). Figure 3.11 shows a notable difference in tip velocity and undercooling relationship for the terrestrial case as compared with TRACE. Dendrite tip undercooling in the diffusive microgravity conditions were between 1.48 and 2.42 times that of terrestrial conditions for the same tip velocity (datapoints within 0.05 $\mu m/s$). As mentioned, the solidification conditions are expected to be thermally stable but solutally unstable, i.e. the solute partitioned at the solid-liquid interface is lower density than the bulk liquid, and therefore more buoyant. Hence, even with the positive vertical temperature gradient, convective instabilities can occur even if the liquid's net density decreases with height. The significant difference between the results in this study and TRACE is attributed to buoyancy-driven thermosolutal convection. Glicksman et al. showed similar findings for free dendritic growth in microgravity and terrestrial conditions with the transparent alloy succinonitrile [16, 41]; the authors reported that tip velocity increased by a factor of two at lower undercooling and that the LGK diffusion solution to the dendrite problem was not consistent with the terrestrial experimental data. Additionally, Cantor and Vogel's theoretical modelling indicates that the effect of fluid flow on tip velocity undercooling relationship is more significant for a constitutional dendrite versus a thermal dendrite.

Several models have been developed to account for the effect of thermosolutal flow

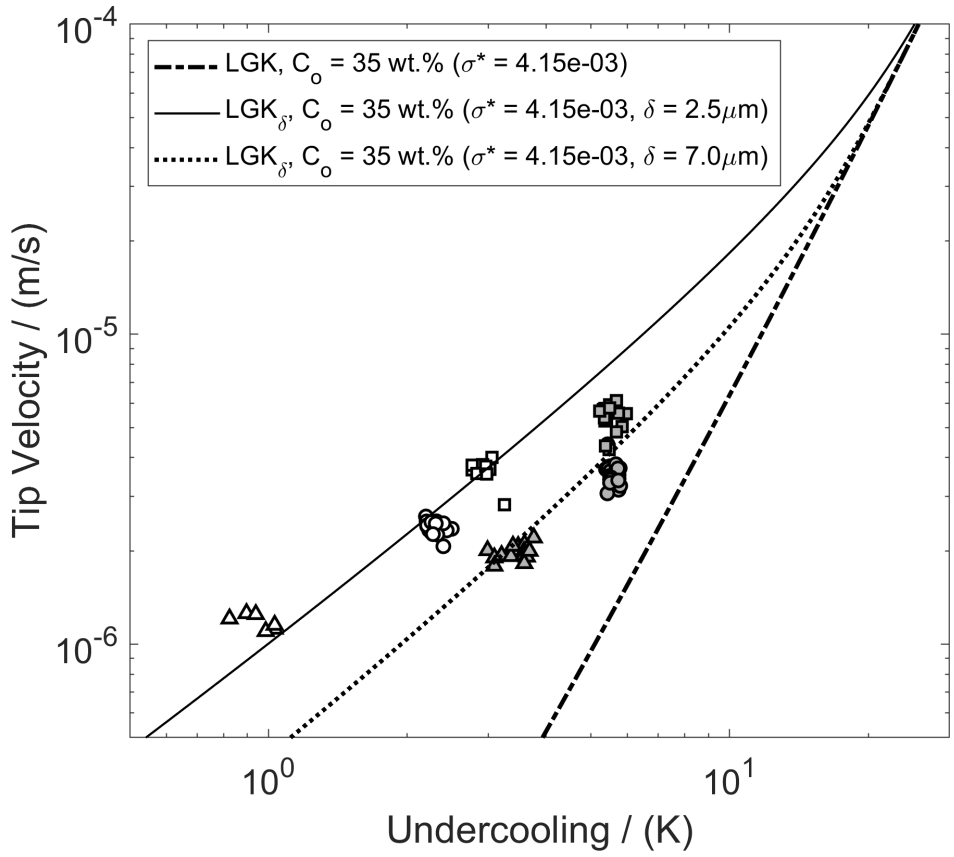

Figure 3.12: Experimental results with comparisons to the LGK model and modified LGK model at two values of δ: 2.5 μm and 7.0 μm.

on dendrite tip velocity. The modified LGK model, which assumes diffusive transport inside a boundary layer of length δ and infinite mixing outside the boundary layer, was applied with finite boundaries of thickness 2.5 and 7 μm. Figure 3.12 shows the LGK model based on $D_L = 9.7 \times 10^{-11} m^2/s$, $C_0 = 35$, and $\sigma^* = 4.15 \times 10^{-3}$, which is representative of microgravity or diffusional conditions. The two corresponding fits with the modified-LGK show good agreement with the terrestrial experimental data where solutal convection is assumed. For comparison purposes, the diffusional solutal lengths with no convection present ($l_s = D_L/v_t$) in the range of 1.0 to 6.0 $\mu m/s$ growth rate would give diffusional solute boundaries of between 17 – 98 μm.

Interestingly, figure 3.12 shows two trends for the dendrite tip velocity as a function of undercooling. At G ≈ 23.5K/cm (open triangle, circle and square markers), the LGK-CV model predicts a boundary layer thickness of 2.5 μm, whereas at G ≈ 16.6 K/cm (triangle, circle and square markers with grey face colour), the LGK-CV model predicts a boundary layer thickness of 7.0 μm. Temperature gradient affects both the mushy zone's depth and permeability, and this likely influences both the fluid flow and

composition fields ahead of the dendrite tips. For example, Wu et al., observed four different flow regimes ahead of the columnar mushy zone corresponding to different mushy zone depths [123]. Buoyancy-driven thermosolutal flow in the solute-enriched mushy-zone, and the resulting flow and compositions field ahead of the dendrite tips, needs to be considered in the context of the mushy zone permeability. Further experiments and numerical modelling are required to fully understand the relationship of temperature gradient on the dendrite tip kinetics.

3.5 Conclusions

A bespoke solidification apparatus and a new experimental procedure has been developed that uses a novel computer vision algorithm to automatically track the position and velocity of multiple columnar dendrites during in-situ observation. In this study, the computer vision algorithm was used to track a total of 385 dendrite tips. A total of 95 dendrite tips were observed to cross an internal thermocouple in the melt; hence, instantaneous measurement of tip velocity and undercooling was provided. The results have been compared with similar microgravity experimental results, and a marked difference is reported between the terrestrial and microgravity data. Comparison was made to the classical LGK growth law based on solute diffusion without convection. At the same growth rates, terrestrial undercoolings were between 0.41 and 0.68 times the predicted growth rates. However, when modifications were made to the theoretical LGK to compensate for the effect of convection, results gave good agreement for finite boundary layers of lengths in the range 2.5 to 7.0 μm. Other effects that were observed and attributed to convection were oscillations of the growth rate (i.e., acceleration-deceleration cycles). Nevertheless, even with undulations of the growth rate, the observed net effect in all cases was growth at an average velocity under thermally steady conditions. The new computer vision algorithm was demonstrated to be highly beneficial since, with 385 dendrite tip tracked, it provides statistical and quantitative data otherwise too laborious to capture manually. In addition to the scaling up of quantitative data analysis, the visual results from the algorithm enhanced the ability to make qualitative observations. For example, velocity vectors shown in videos

for test no. V and VI illustrate the classic Walton-Chalmers predicted behaviour [9], i.e. misaligned dendrites lag the aligned dendrites and have a y-component of velocity close to that of the aligned dendrites. Further work with the computer vision algorithm may provide deeper insights into competitive growth and the Walton-Chalmers model. The results from this study and the application of this new procedure to other scenarios will be of interest to the modelling community who are interested in modelling competitive columnar growth, for example, the work of [124–128].

Acknowledgements

This work was supported by the European Space Agency (ESA) [contract number 4200014313NL/SH, CCN009 to AO-99-117] and by ESA PRODEX [contract number 4000110385 CN 3] as part of the CETSOL Microgravity Application Programme. ESA PRODEX funding is managed by the Irish Space Delegation at Enterprise Ireland. We wish to acknowledge Laszlo Sturz and Gerhard Zimmermann for sharing TRACE experimental data and for fruitful conversations.

Chapter 4

Competitive Growth during Directional Solidification Experiments of $\langle 111 \rangle$ Dendrites

Abstract

Competitive growth is a key topic in directional solidification. However, to the authors' best knowledge, there are no experimental or numerical studies on competitive growth for $\langle 111 \rangle$ dendrites. Compared with classical $\langle 100 \rangle$ dendrites, which can grow in six directions orthogonal to one another, $\langle 111 \rangle$ dendrites can grow in eight directions. Consequentially, secondary arms in $\langle 111 \rangle$ dendrites are more favourably oriented than the corresponding secondary arms in $\langle 100 \rangle$ dendrites and this has implications for the competitive growth mechanism during directional solidification. An experimental apparatus was developed for in-situ directional solidification with a transparent model alloy, Neopentyl Glycol-35wt.% (D)Camphor (NPG-35wt.%DC), which has $\langle 111 \rangle$ dendrite orientation. Seven tests scenarios were investigated with different temperature gradients and isotherm speeds. Each scenario was investigated for its competitive growth behaviour from randomly oriented seed crystals to the final observed macrostructure. Multiple grains were identified in each test with examples of competition at converging and diverging grain boundaries as well as obedience and disobedience with the widely accepted Walton-Chalmers rule for predicting preferential growth orientations.

Unfavourably oriented crystal colonies at diverging grain boundaries competed with and were able to outgrow favourably oriented colonies via tertiary branching. Overgrowth by the unfavourably oriented crystal was linked to the advantageous growth directions of secondary arms in ⟨111⟩ dendrites. A newly developed computer vision algorithm for dendrite tip velocity tracking further elucidated the tertiary branching mechanism that allowed the unfavourably oriented crystal colonies to stabilise along the growth direction. It is proposed that the deviation from the Walton-Chalmers rule of competitive growth is probabilistic and depends on the initial seeding.

4.1 Introduction

Competitive dendritic growth is a key topic in directional solidification as it influences the grain structure or crystallographic texture, and hence the material properties of as-cast parts. Preferred growth directions arise due to temperature gradients at the macro scale, where crystals with differing orientations compete to outgrow one another. Crystal arms that are well-aligned with but growing in the opposite direction to the heat flow have preferential orientation. The Walton-Chalmers rule [9, 10], depicted in figure 4.1, is a well-accepted description of how preferred orientations arise in directional solidification of crystals with ⟨100⟩ morphology [129, 130]. The figure shows three neighbouring colonies of dendrites; colonies A and C with favourable orientations have their growth direction aligned with the direction of heat flux, while colony B has an unfavourable orientation and grows at some offset, α_1, to the preferred direction. Under steady-state conditions, the liquidus isotherm advances with speed v_L and well-aligned dendrites will grow at some distance behind it by matching their growth rate to the liquidus isotherm speed, $v_1 = v_L$. To maintain the required speed, the dendrite tips grow at some finite distance behind the liquidus isotherm where it can experience the required level of undercooling, ΔT_1. To remain competitive, misaligned dendrites have to maintain higher tip growth rates ($v_2 > v_1$) such that their vector component in the favourable direction, v_2', matches the isotherm speed (i.e., $v_2 = v_L/Cos\alpha_1$). To maintain higher growth rates, the misaligned dendrites must grow at a higher undercooling, ΔT_2, which is found at a distance further behind the liquidus isotherm

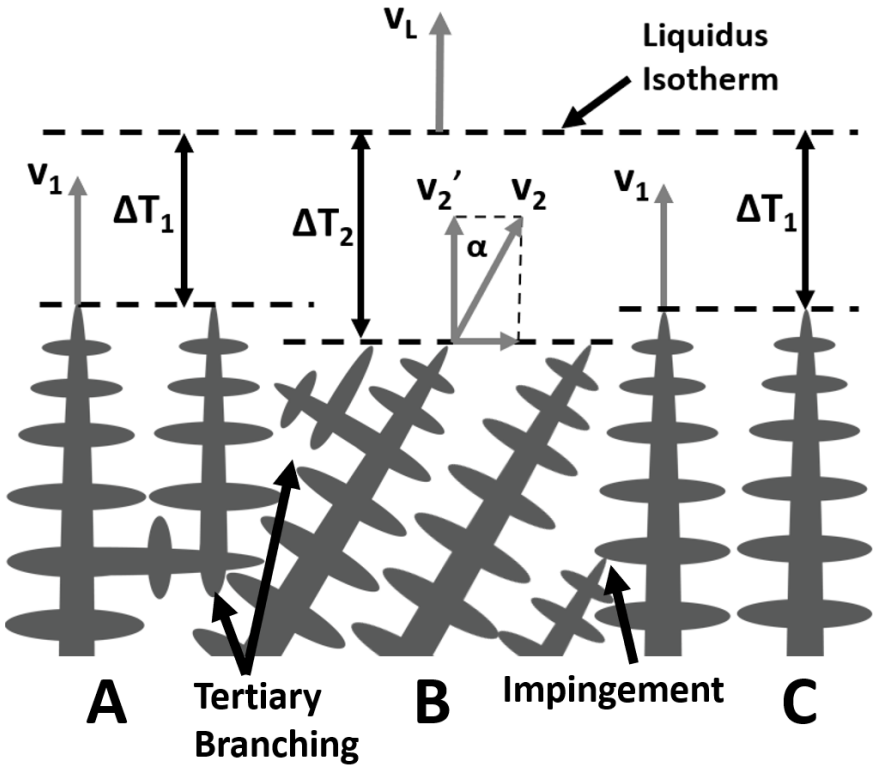

Figure 4.1: Schematic illustration of Walton-Chalmers rule. In order to have a vertical component of velocity equal to its neighbour, the unfavourably oriented dendrite colony (B) lags the favourably oriented colonies (A and C) and grows at greater undercooling and tip velocity. Colony B impinges on colony C at the converging boundary, while colony A tends to outgrow colony B via tertiary branching at the diverging grain boundary.

than the tips of the favourably-orientated dendrites. Consequentially, neighbouring misaligned dendrites lag behind and get outgrown or blocked by their more favourably orientated counterparts. Figure 4.1 shows Colony B's primary dendrite tips impinge on colony C at the grain boundary. At the AB boundary, colonies A and B compete via tertiary branching, and favourably oriented crystals A and C overgrow and eliminate the unfavourably oriented crystal, B. Thus, the Walton-Chalmers model explains the origin of preferred orientation in directional solidification, i.e., the decreased average misalignment [9] and reduced spread of the misalignment [10], which occurs due to competitive growth. The model was later validated by in-situ experiments with the SCN-ACE transparent alloy system [23, 131].

In metal casting, a chill zone typically forms beside the mould wall in contact with the liquid melt with an initially homogenous temperature and composition. The chill zone consists of a thin layer of fine equiaxed dendrites with random orientation. Heat exits through the mould wall as the temperature gradient forms and favourably orien-

tated arms of primary equiaxed dendrites grow directionally in opposition to the heat flux direction via the competitive mechanism described by Walton and Chalmers. After reaching a sufficient aspect ratio (typically greater than two [132]), the crystals are classified as columnar. This process is termed the Equiaxed-to-Columnar Transition (ECT). As solidification continues in the casting, temperature gradients may decrease such that the columnar dendrites lose their competitive advantage, and equiaxed solidification (with no preferential orientation) can replace the columnar structure. The process is termed the Columnar-to-Equiaxed Transition (CET). An increase in liquidus isotherm speed or a decrease in temperature gradient (or both) causes the Columnar-Equiaxed Transition (CET). In the CET scenario, constitutional undercooling in the liquid ahead of the columnar front exceeds the heterogeneous nucleation and free growth undercooling levels. Nucleation and growth of equiaxed crystals occur in sufficient numbers and then block the columnar front. Recent investigations have shown that the CET can be sharp or progressive [133, 134]. In a sharp CET, equiaxed growth occurs in sufficient numbers, and this results in an abrupt transition from aligned columnar crystals to randomly oriented equiaxed crystals with an aspect ratio close to unity. Progressive CETs have an intermediate region where, after partial columnar blocking, the favourably oriented arms of equiaxed crystals that become embedded into the growth structure may proceed to grow competitively and reach elongation factors greater than two [135]. Competitive crystal growth is, therefore, an important mechanism in both ECT and progressive CET. Several reviews of this CET are available [5, 6] and studies are ongoing within this topic [136]. If the growth rate and temperature gradient can be maintained (as in the Bridgman-Stockbarger process), well-aligned columnar structures can be produced consistently.

Dendritic growth in Face Centred Cubic alloys typically occurs along $\langle 100 \rangle$ crystallographic directions. However, atypical growth directions are being observed in technologically important alloys, from lightweight aluminium alloys to Ni-base superalloys [137]. Examples include $\langle 111 \rangle$ growth in Al-Fe [138] and $\langle 110 \rangle$ growth in certain compositions of Al-Zn [139, 140] and Al-Ge [141]. Recently, unexpected $\langle 111 \rangle$ growth in Al-Cu [142–145] was reported. The different growth directions are linked

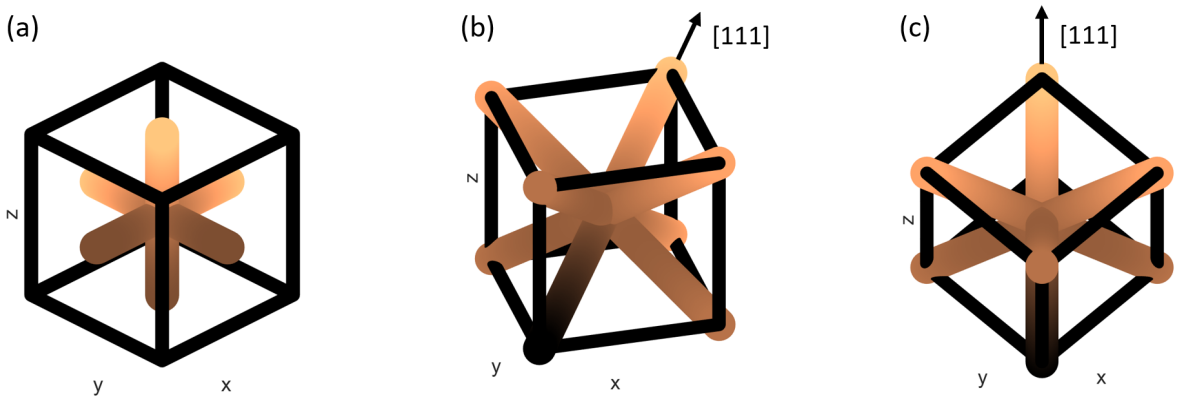

Figure 4.2: Unit cells for ⟨100⟩ and ⟨111⟩ dendrite patterns: (a) Classical ⟨100⟩ pattern with six growth directions (all orthogonal to each other) (b) ⟨111⟩ dendrite pattern with eight growth directions (c) ⟨111⟩ pattern viewed orthogonal to the [111] direction; a primary columnar dendrite aligned with [111] has six secondary dendrite arms; three arms subtend 70.5^o from the primary growth axis, and the other three subtend 109.5^o.

to composition-related changes in the surface-tension anisotropy distribution [139] and are likely to be influenced by the surface attachment kinetics [142]. Since crystals' orientation and hence the growth direction of primary dendrite tips are key in determining the competitive growth, the family of crystallographic directions along which dendrite tips can grow should undoubtedly be an important consideration. Figure 4.2 shows the growth directions arising in ⟨100⟩ and ⟨111⟩ dendrites. Classical ⟨100⟩ dendrites can grow in six directions where secondary or higher-order dendrite arms grow orthogonally to the parent arm. With ⟨111⟩ patterns, dendrite arms can grow in eight directions towards each corner of a unit cell. In this case, secondary or higher-order dendrite arms can grow at either 70.53 or 109.47 degrees from the parent arm. The implications for modelling and theory of pattern formation during solidification are not yet fully understood. However, it will be argued that three secondary dendrite arm directions of the ⟨111⟩ dendrites should have a 19.53 degree angular advantage compared with the secondary arms of ⟨100⟩ dendrites. This difference in secondary arm alignment will be shown to have consequences on the directional solidification of ⟨111⟩ columnar structures - this is a point that has not yet been characterised or realised. The purpose of this study is to investigate the competitive growth mechanisms for ⟨111⟩ growth morphologies. An experimental setup was developed to study macrostructure structure formation during directional solidification using a binary transparent alloy Neopentyl-Glycol-35wt.%(D)-camphor (NPG-35wt.%DC) [67]. The transparent alloy

in question has been shown to solidify with ⟨111⟩ dendritic structures [68] when the alloy composition is higher than 30 wt.%. Optical microscopic imaging allowed for in-situ observation and real-time visualisation of competitive columnar growth in the ⟨111⟩ transparent alloy of NPG-35wt.%DC. The newly developed multiple dendrite tip tracking algorithm, described in Chapter 3, augmented the in-situ footage with velocity vectors on the dendrite tips, which aided in elucidating competitive growth mechanisms. The objectives of the investigation were as follows:

- To investigate competitive crystal growth mechanisms in directionally solidified ⟨111⟩ crystals.
- To apply the recently-developed dendrite tip tracking algorithm to further elucidate on the mechanisms of competitive crystal growth.
- To assess the competitive crystal growth mechanisms in ⟨111⟩ dendritic patterns against the classic Walton-Chalmers mechanism.

Competitive crystal growth mechanisms are of particular interest to the aerospace industry for the manufacture of turbine blade and they are of fundamental interest for further modelling activity [94]. Competitive growth models have been integrated into several numerical models of directional solidification. Hence, the experimental data provided from the study proposed here will be useful for model elucidation and validation.

4.2 Methods

4.2.1 Materials

The transparent model alloy NPG-35wt.%DC was prepared from organic crystalline materials NPG and DC at commercial purity provided by Sigma Aldrich. At the 20 to 30wt.% composition range, the NPG-DC alloy system undergoes a dendrite orientation transition from $\langle 100 \rangle$ to $\langle 111 \rangle$. The present experiments use a hypoeutectic composition of C_0=35wt.%, with $\langle 111 \rangle$ dendrite orientation. The alloy was prepared in a sealed glove box under Argon atmosphere (<5ppm H_2O), as described in section 3.2.2, and liquid NPG-35wt.%DC was then transferred from the glovebox in a high-temperature gas-tight glass syringe.

4.2.2 Apparatus and Processing Conditions

Figure 4.3 shows a schematic overview of the experimental facility used. The apparatus consisted of an optically transparent annular sapphire crucible with temperature controlled hot and cold zones for directional solidification. Setpoint control of temperatures, T_H and T_C, provided controlled temperature gradient, G, cooling rate, $\dot{T}$, and hence isotherm speed, v_L, in the baffle zone. A camera and variable lens (1.4x–13x zoom) mounted perpendicularly to the crucible's vertical axis recorded video sequences of the directional solidification in the baffle zone. For a more detailed description of the experimental apparatus and control, the reader may refer to [67].

The test material in the crucible above the cooler was brought into the liquid phase by increasing the heater's temperature to 120^{o}C. To ensure a homogenous initial composition in the liquid melt before any given test, the baffle zone was heated with a heat gun and the heater was temporarily turned off to induce convective mixing for a period of 5 minutes. The heat gun was then turned off and setpoint temperatures of T_H and T_C were adjusted to prepare the initial temperature gradient and to position the equilibrium liquidus isotherm just inside the camera's field of view. After deactivating the heat gun, equiaxed crystals nucleated in the liquid melt and sedimented on the top of the mushy zone providing initial seed crystals with random orientations. The

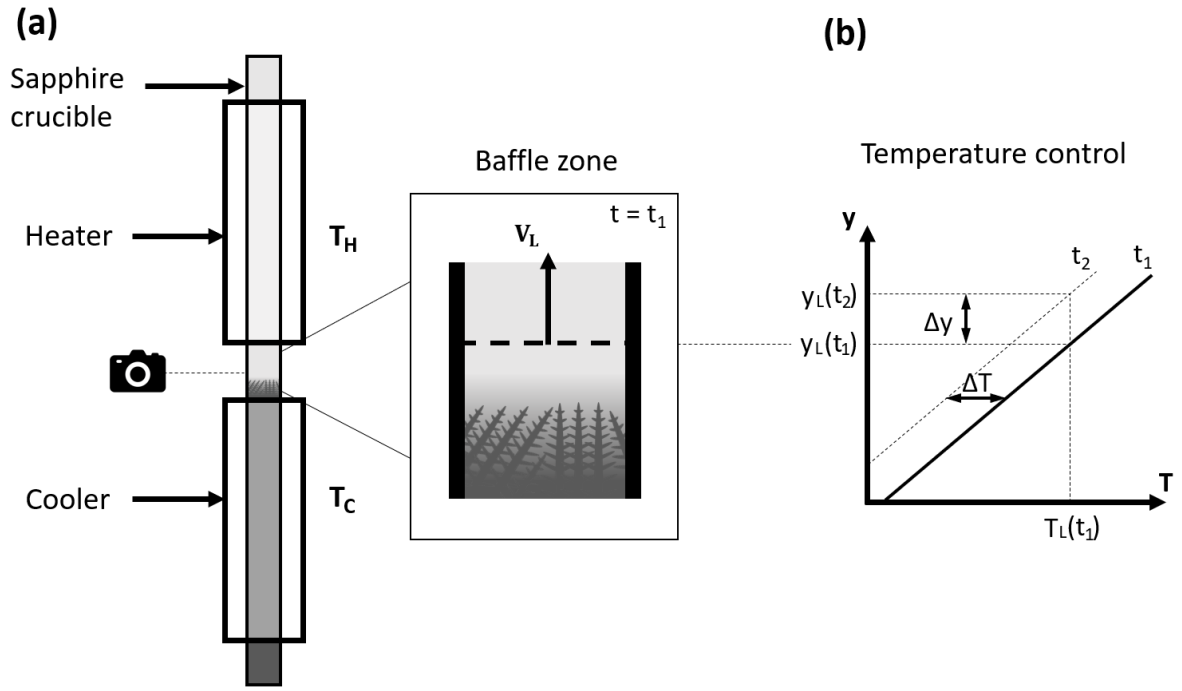

Figure 4.3: Schematic illustration of experimental facility (a) test apparatus and magnified view of the baffle zone (b) graphical illustration of temperature control showing position of the liquidus isotherm y_L at time t_1. Equal cooling rates of the heater and cooler advances the liquidus isotherm with velocity, v_L, where $v_L = (\Delta T/\Delta t)(\Delta y/\Delta T)$, or simply $v_L = \dot{T}/G$.

initial conditions for T_H and T_C were then held for a period of at least 40 minutes and this allowed the solidification front to align with the liquidus isotherm. At that point, ramp down cooling was initiated and optical imaging commenced. The in-situ optical footage was processed with a newly developed computer vision algorithm for automated tracking of columnar dendrite tip velocities. Additionally, a novel image-processing technique, described in the following subsection, was used to provide a detailed post-mortem image of the micro-macro structure.

Table 4.1: A list of solidification processing parameters

Test Scenario	Cooling Rate (K/min)	Temperature Gradient (K/cm)
1	0.16	23.30 ± 1.80
2	0.30	23.58 ± 1.83
3	0.45	23.64 ± 1.83
4	0.16	16.79 ± 1.80
5	0.30	16.55 ± 1.80
6	0.45	16.57 ± 1.41
7	0.15	23.45 ± 1.83

4.2.3 Image Processing and Analysis

Due to the reduced opacity of the solidified structure, especially in the main bulk of the sample, microstructure detail and crystallographic features were difficult to distinguish. Microstructure detail was more discernible at the top of the mushy zone. Hence, a single, in-situ optical image of the solidifying mushy zone lacked underlying microstructure detail. To capture the columnar network development, other investigators have used manual overlay methods of images from the top of the mushy zone captured during solidification [22, 130]. Here, an automatic image processing technique was developed to automate the process to show more detail of the underlying microstructure. Figure 4.4 shows a schematic illustration of the image processing technique. Automatic tracking (as outlined in [67]) was used to provide the average vertical position of the top of the mushy zone, y_f. The image processing technique then automatically cropped a rectangular window from the given input image with the rectangle's upper left corner located at (0, y_w). A window height, h_w, was defined. The first image for any given sequence was selected based on the earliest position data provided by the tracker and subsequent images were selected corresponding to the solidification front advancing by a distance approximately equal to height of the window (within one pixel). For the first and last input images, the size of the cropped window extended to the bottom or top of the respective input image. Vertical concatenation of the cropped images then provided a single output image that facilitated assessment of the underlying microstructure. Figure 4.5 shows an example of a Vertically Concatenated (VC) micrograph from test scenario 5 with manually overlaid lines to assess the misalignment of the dendrites. Dendrites arms greater than 1mm in length were deemed to have sufficient directionality to be considered in the analysis; hence secondary and tertiary arms greater than 1mm were included in the analysis. Average and mean absolute deviation of dendrite misalignment were recorded at 30 evenly spaced vertical positions along the y-axis.

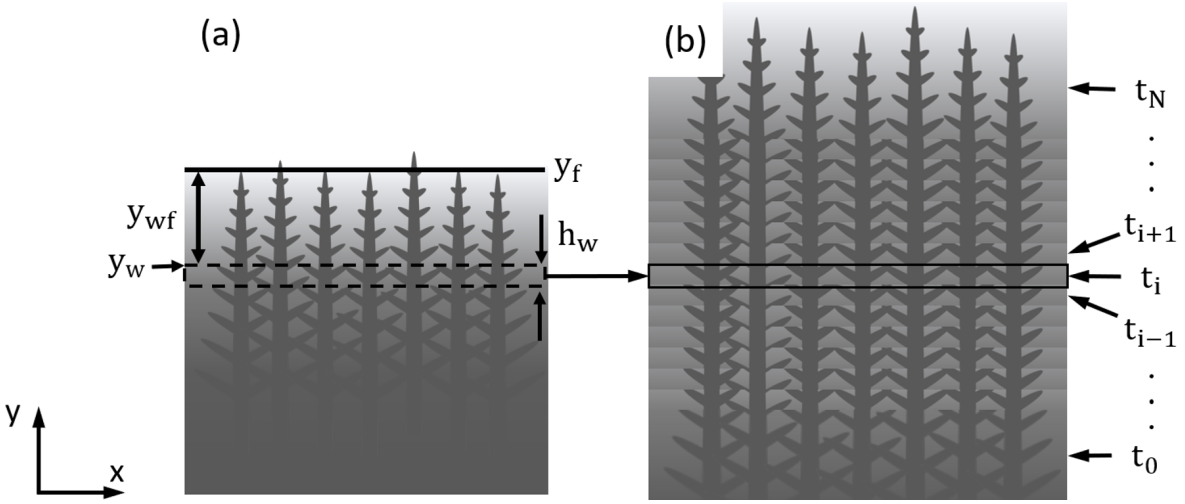

Figure 4.4: Schematic illustration of image processing technique for developing detailed image of the microstructure (a) input image at time t_i with coordinates of the cropped window (b) output image from vertically concatenating windows of the selected input images.

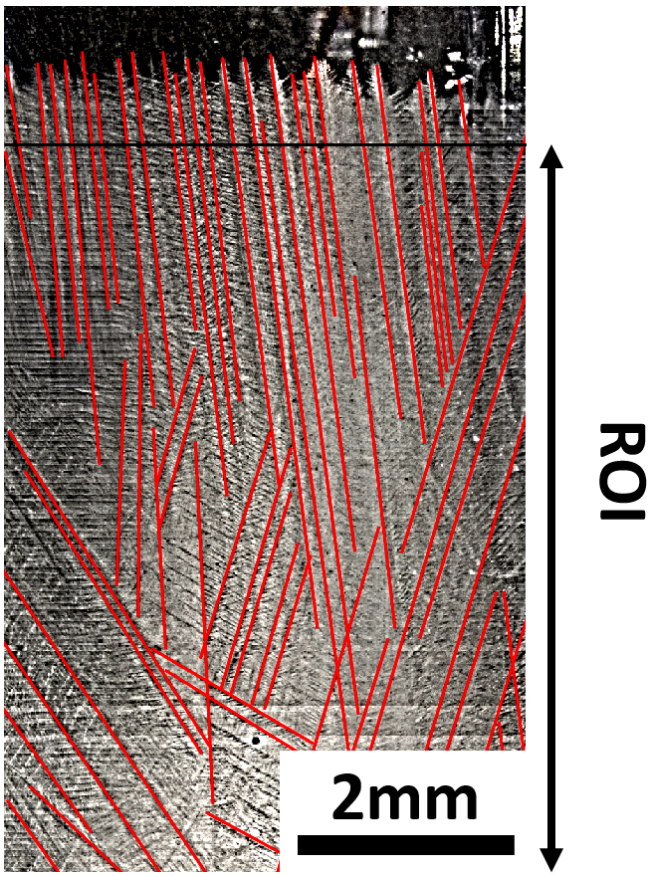

Figure 4.5: Vertically concatenated micrograph of test scenario 5 showing manual assessment of dendrite orientation

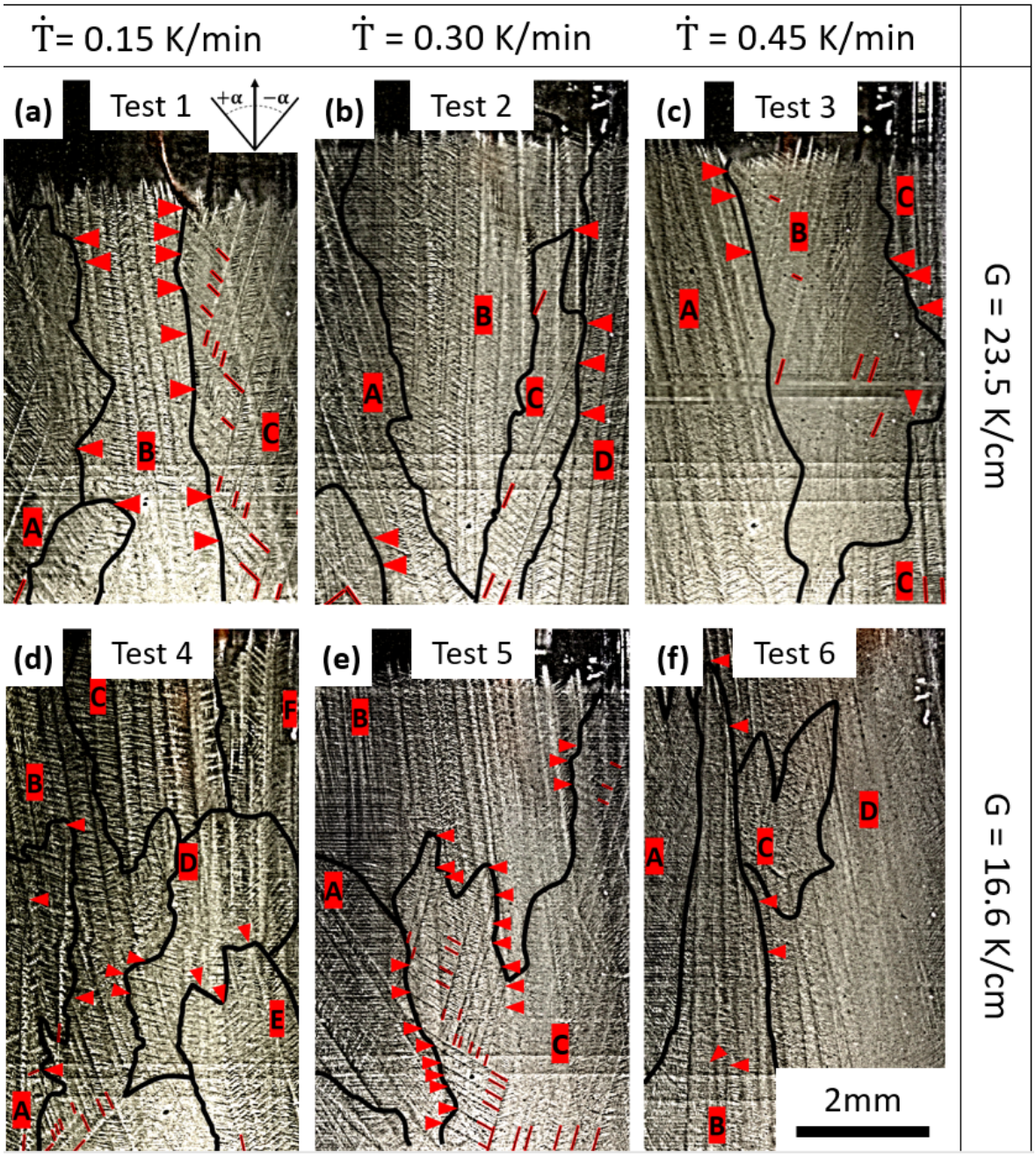

Figure 4.6: VC micrographs showing macro-micro structure for tests 1 – 6, listed as (a) – (f), respectively. Red arrowheads show impingement, while the red/black lines highlight dendrite arm origins and the ladder structure. Grain boundaries are shown with solid black lines.

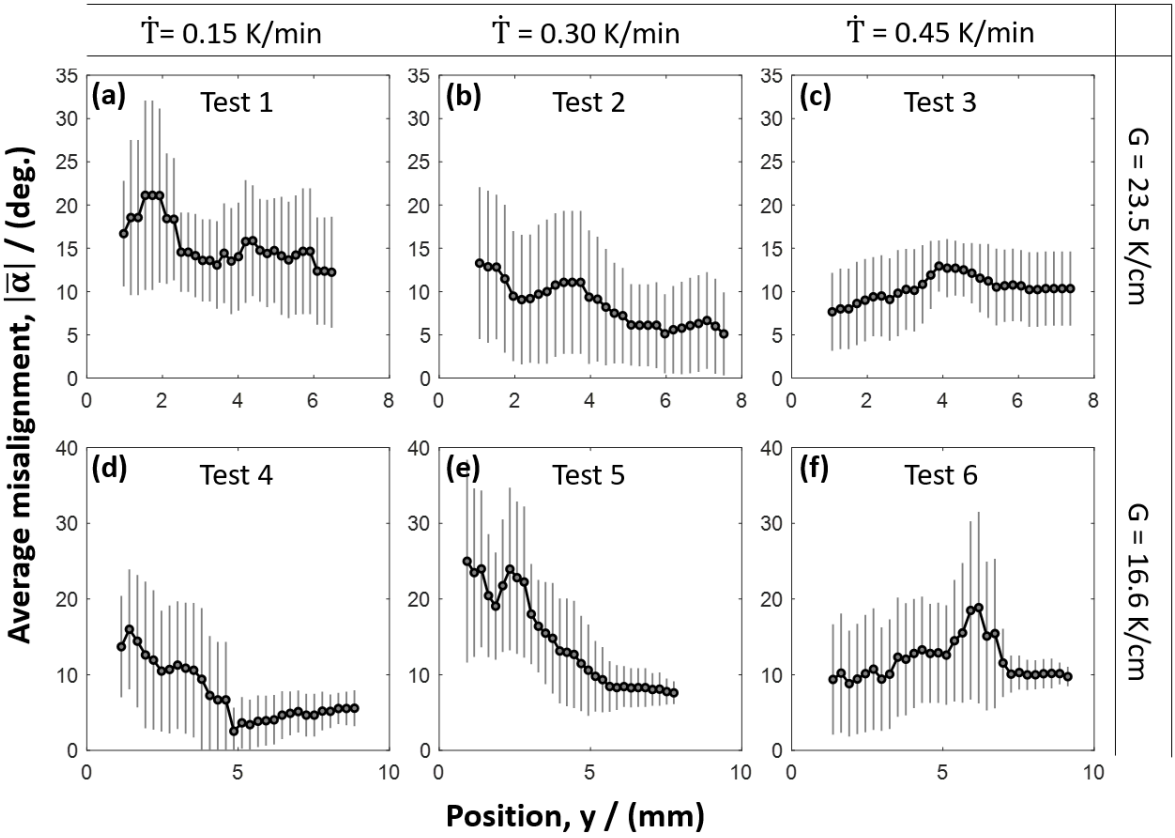

Figure 4.7: Average misalignment ± one mean absolute deviation (as a descriptive statistic), versus y position for test scenarios 1 to 6.

4.3 Results

As mentioned, seven directional solidification tests scenarios were conducted to investigate competitive growth in the ⟨111⟩ transparent alloy NPG-35wt.%DC. Figure 4.6 shows the VC micrographs for test scenarios 1 to 6 with details of the thermal processing conditions on the border, while figure 4.7 shows the graphs of average dendrite misalignment, $|\bar{\alpha}_1|$, versus the vertical position, y. The graphs include intervals of one mean absolute deviation as a descriptive statistic of the spread of dendrite arm misalignment. Additionally, figure 4.8 (a) and (b) shows a VC micrograph and graphed results of $|\bar{\alpha}_1|$ versus y, corresponding to test scenario 7. In general, $|\bar{\alpha}_1|$ decreased with increasing, y, and is evidence that well-oriented crystals can outgrow unfavourably oriented neighbouring crystals in agreement with the Walton-Chalmers rule. In particular, test scenarios 1, 2, 4, and 5 showed obedience to the Walton-Chalmers rule with average misalignment, $|\bar{\alpha}_1|$, shown to decrease with increasing y. Test scenario 3 initially disobeyed then obeyed the Walton-Chalmers rule with average misalignment increasing from 7.6^o to 13^o but then at the 4 mm position decreasing to 10.4^o. Test 6

also showed an increase in $|\bar{\alpha}_1|$ but this is attributed to the presence of an embedded equiaxed grain. Contrastingly, test scenario 7 (figure 4.8) showed a steady increase in average misalignment throughout the recorded growth from 14.3 to 26.5^o. This result is evidence of disobedience with the Walton-Chalmers rule.

While the graphs of average misalignment against the vertical position, shown in figure 4.7 and figure 4.8 (b), provide a macroscopic average of competitive crystal growth, it was necessary to assess competitive crystal growth mechanisms along the individual grain boundaries. The competition occurred between multiple dendritic colonies in all seven test scenarios with examples of both diverging and converging colonies, and examples of obedience and disobedience with the Walton-Chalmers rule. A pair of crystal colonies are deemed diverging when the crystals' primary growth directions point away from each other in the image plane whereas two crystal colonies are deemed converging when the primary growth directions point towards each other in image plane. Figure 4.6 and figure 4.8 (a) show the colonies and grain boundaries identified in each test scenario (annotated A, B, C, etc.). Black contours indicate the grain boundaries between colonies of directionally aligned dendrites and yellow/black arrowheads highlight dendrite impingement points. The list of dendritic colonies for each test scenario, their primary growth direction, α_1 and competitive secondary directions, α_2, are listed in table 4.2. Orientations α_1 and α_2 are provided with respect to the vertical axis (see reference axis and convention in figure 4.6 (a)). Table 4.2 also lists the grain boundaries; the relative orientation of the neighbouring crystals (i.e., whether they were converging or diverging from one another); and whether they displayed obedience or disobedience to the Walton-Chalmers rule. Grain boundaries with orientations greater than 45^o were omitted because the competition was assumed to occur predominantly due to misalignment about the x-axis. Descriptions of the outcomes from each test scenario are provided in the following paragraphs.

Test scenario 1, shown in figures 4.6 (a) and 4.7 (a), showed a small decrease in average misalignment, $|\bar{\alpha}_1|$, from 16.7^o to 12.2^o. Two grain-boundaries formed in this test with converging growth at the AB boundary and diverging growth at the BC boundary. Competition at grain boundary AB obeyed the Walton-Chalmers rule where

the favourably oriented colony, B, tended to outgrow colony A. However, competition at boundary BC disobeyed the Walton-Chalmers rule since the less favourably oriented colony C tended to outgrow colony B by forming a ladder of tertiary branches at the grain boundary. The success of C at the diverging boundary was due to the orientation compared with B, $\alpha_{1,C} = -16^o$ and $\alpha_{1,B} = 7^o$, which allowed secondary arms of C to be more favourably oriented and better able to compete with the secondary arms of crystal colony B. The favourably oriented crystal colony B was consistently overgrown by this mechanism.

Figure 4.6 (b) shows test scenario 2. Most grain boundaries that formed in this scenario obeyed the Walton-Chalmers rule. For example, colony B, with $\alpha_{1,B} = 0^o$, tended to overgrow unfavourably oriented colonies A ($\alpha_{1,A} = 18^o$) and C ($\alpha_{1,C} = -22^o$). Colony C, was less favourably oriented compared with neighbouring colonies B and D ($\alpha_{1,D} = -8^o$); at the diverging boundary between B and C, colony C was overgrown by B. At the converging CD boundary, colony C tended to overgrow the favourably oriented colony D. A higher overgrowth rate by B on C compared with C on D ultimately led to C's elimination. The CD boundary was the only case in test scenario 2 that showed disobedience with the Walton-Chalmers rule. Figure 4.7 (b) shows that test scenario 2 generally obeyed the Walton-Chalmers rule, where misalignment decreased throughout and, in general, the mean absolute deviation also reduced.

Test scenario 3, shown in figures 4.6 (c) and 4.7 (c), shows colony C ($\alpha_{1,C} = 3^o$) with favourable orientation initially overgrown by its neighbour B ($\alpha_{1,B} = -15^o$) causing the average misalignment to increase, but then C begins to overgrow B again. Colony B, diverging from colony A ($\alpha_{1,A} = 13^o$), also tended to outgrow colony A with periodic tertiary branching.

Test scenario 4 showed a decreasing $|\bar{\alpha}_1|$ and a decreasing mean absolute deviation. In general, the trends obeyed the Walton-Chalmers rule, with unfavourably oriented colonies B and E being overgrown. However, colony A with $\alpha_{1,A} = 0^o$, was overgrown by colony B.

Test scenario 5, shown in figures 4.6 and 4.7 (e), shows obedience to the Walton-Chalmers rule with decreased average misalignment and mean absolute deviation show-

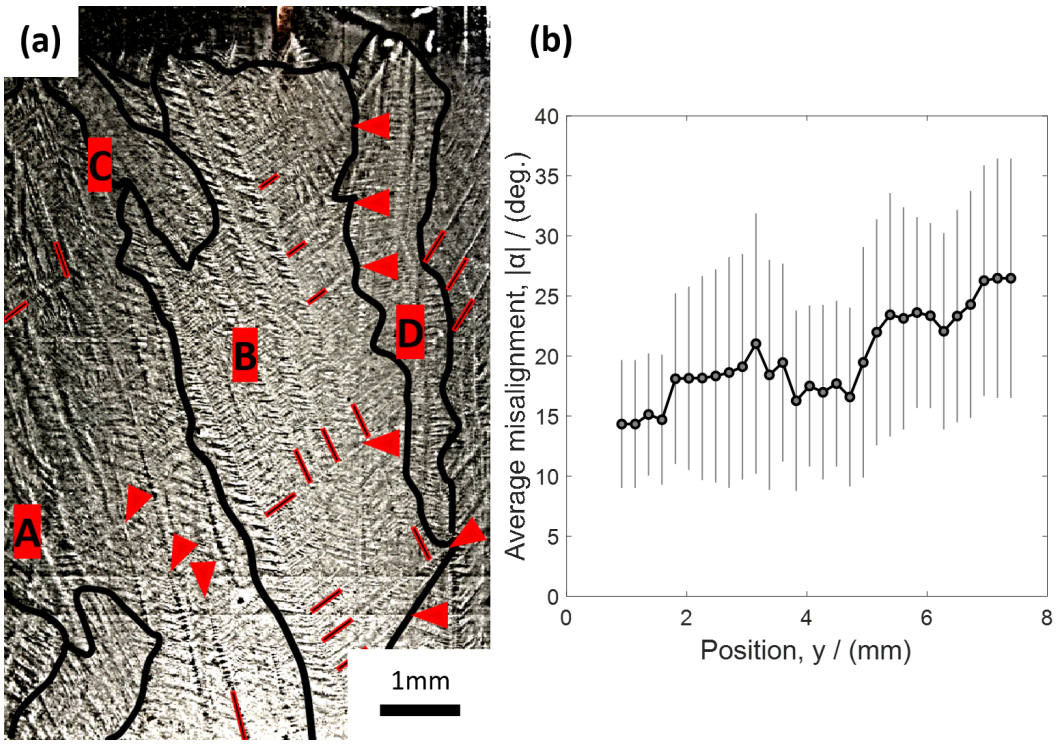

Figure 4.8: Results of test scenario 7 processed with temperature gradient, G = 23.45 ± 1.83 K/cm, and cooling rate $\dot{T}$ = 0.15 K/min (a) vertical concatenation image showing underlying micro – macro structure (b) average dendrite misalignment versus position

ing convergence to a single preferential orientation. A single colony of dendrites, B, with a misalignment of $\alpha_{1,B} = 7^o$ tended to overgrow colonies A and C ($\alpha_{1,A} = 33^o$ and $\alpha_{1,C} = -17^o$). Correspondingly, the graph in figure 4.6 (e) shows an average misorientation converging on 7^o.

In test scenario 6 (figures 4.6 and 4.7 (f)), colony D tended to outgrow its neighbours B and A. An equiaxed crystal (C) nucleated ahead of the columnar front and blocked growth in this area as it settled into and became embedded into the columnar structure. The more favourably oriented arms of the equiaxed crystal ($\alpha_{1,C} = -19^o$) continued to grow and competed with colonies B ($\alpha_{1,B} = -1^o$) and D ($\alpha_{1,D} = 10^o$) but were shortly outgrown by the more favourably oriented colony B. Correspondingly, Figure 4.7 (f) shows the increase in average dendrite misalignment between 5mm and 7mm in the vicinity of the elongated equiaxed grain.

In contrast to the trends observed in tests 1 to 6, test scenario 7, under similar processing conditions as test 1, showed that dendrite alignment did not follow the Walton-Chalmers rule. Figure 4.8 (a) shows the average dendrite misalignment, which tended to increase throughout the experiment. The increase was partly due to the

competitive secondary arms of colony B where $\alpha_{1,B} = 24^o$ and $\alpha_{2,B} = -53^o$, and colony E where $\alpha_{1,E} = 1^o$ and $\alpha_{2,E} = -30^o$, but also colony C which emerged further up with $\alpha_{1,C} = -40^o$. At the diverging BD boundary where $\alpha_{1,B} = 24^o$ and $\alpha_{1,D} = -3^o$, colony D tended to overgrow colony B, but B was largely stabilised due to competitive secondary arms. Consequentially, the average misalignment increased from 14^o to 27^o.

Figure 4.9 shows a close-up image sequence from test 5 in the upper right area of colony D (see figure 4.6 (f)) with a primary growth direction of $\alpha_{1,D} = -19^o$ and primary dendrite tip velocities that ranged from 4.5 to 5 μm/s. The secondary arms with $\alpha_{2,D} = 48$ grew at approximately 7μm/s. A new colony emerged (figure 4.9 (d)) with favourable alignment ($\alpha_1 = -10^o$) with tip velocities between 5 and 5.5 μm/s. Supplementary video data is available on the journal website. The observed trends between the growth vectors and the resulting final grain textures are discussed in greater detail in the next section.

Figure 4.10 shows the development of the grain boundary in test 5 between diverging colonies A and C. Colony C periodically formed tertiary branches and ladder structures with alternating success between arms growing along with the primary [111] and secondary [$1\bar{1}1$] directions. Video evidence (provided as supplementary data on the journal's website) shows that an opening formed between the diverging colonies A and C, and secondary arms grew into the open region. Figure 4.10 (d)-(e), show a tertiary arm extending along the crystals [111] direction was able to break out and block the newer secondary dendrite arms, which were further up the primary trunk. As solidification proceeded, the [111] tertiary arms eventually became primary arms themselves. The secondary arms of the initial primary dendrite did not compete any further as their pathways were blocked by its neighbour's successful tertiary arms.

Table 4.2: Summary of crystal misalignment and observations of obedience or disobedience with the Walton-Chalmers rule at each grain boundary.

			Grain Boundary and comments	
	α_1	α_2	Boundary	Comments
Units	degree	degree		
Test Scenario 1				
Colony A	-20	40	AB	converging obeys
Colony B	7		BC	diverging disobeys
Colony C	-16	44		
Test Scenario 2				
Colony A	18		AB	diverging obeys
Colony B	0		BC	diverging obeys
Colony C	-22		BD	diverging obeys
Colony D	-8		CD	converging disobeys
Test Scenario 3				
Colony A	13		AB	diverging disobeys
Colony B	-15		BC	converging disobeys then obeys
Colony C	3			
Test Scenario 4				
Colony A	0		AB	converging disobeys
Colony B	10		BC	diverging obeys
Colony C	4			
Colony D	1			
Colony E	17			
Colony F	-2			
Test Scenario 5				
Colony A	33		AB	diverging obeys
Colony B	7		BC	converging/diverging obeys
Colony C	-17	58	CD	converging obeys
Colony D	24			
Test Scenario 6				
Colony A	-19		AB	converging disobeys
Colony B	-1		BD	converging disobeys
Colony C	-19			
Colony D	10			
Test Scenario 7				
Colony A	17		AB	converging disobeys
Colony B	24	-53	BD	diverging obeys
Colony C	40			
Colony D	-3			
Colony E	1	-30		

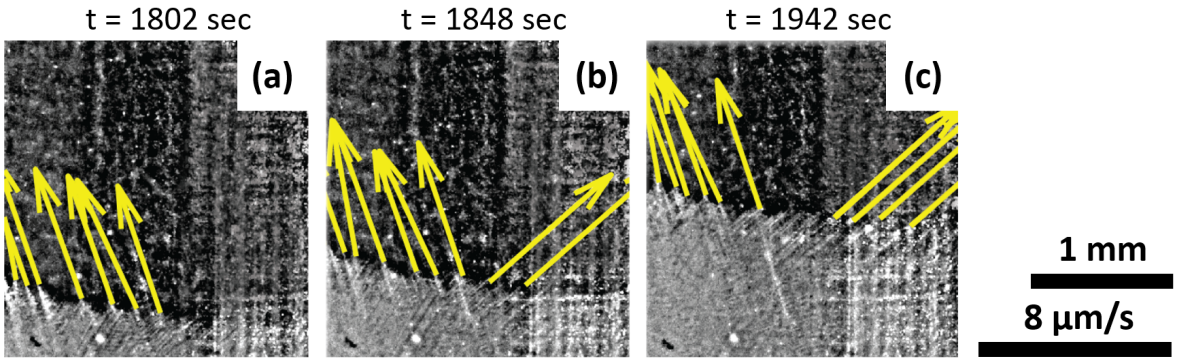

Figure 4.9: Optical image sequence showing dendrite tip tracking on crystal D, test 6. The image sequence shows a colony of secondary dendrite arms from crystal D growing with higher misalignment and tip velocity.

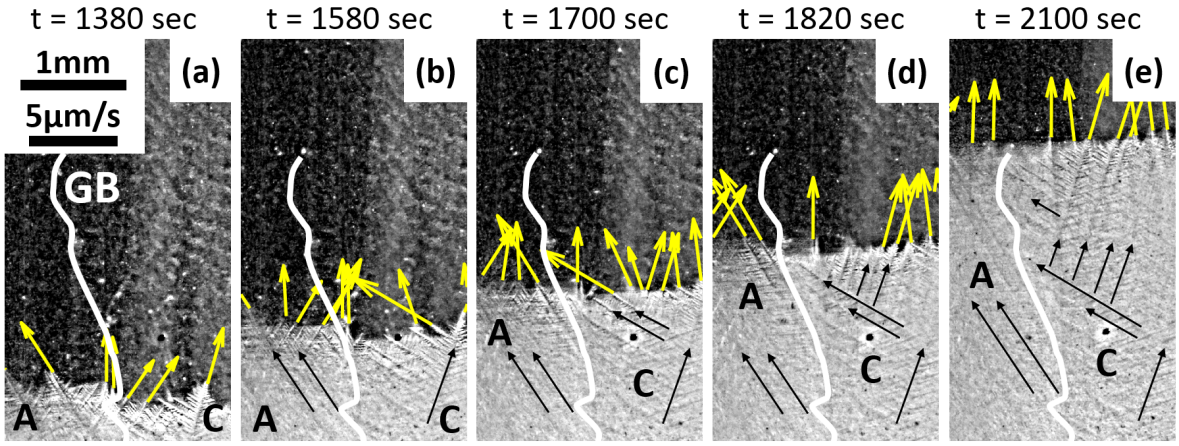

Figure 4.10: Optical image sequence from test 5 with dendrite tip tracking showing grain boundary formation for diverging crystals colonies A and C. Colony C's secondary arms grow into and fill the space between the diverging grains and repeated tertiary branching forms a ladder structure in colony C.

4.4 Discussion

Competitive directional crystal growth mechanisms emanating from randomly oriented seed crystals have been investigated with seven directional solidification tests. Multiple colonies formed in each test scenario with examples of both diverging and converging boundaries, as well as obedience and disobedience with the Walton-Chalmers rule. The analyses were aided by a newly developed computer vision algorithm that provided automatic tracking of the positions and velocity vectors for multiple columnar dendrite tips observed within each experiment. The results indicate that scenarios that disobeyed the classical Walton-Chalmers rule, that is, by the unfavourably orientated crystals tending to overgrow the favourably orientated crystals, occurred due to preferential tertiary branching from the unfavourably orientated crystal colonies.

Tertiary branching occurs in single-crystal directional solidification when the primary growth direction is not aligned with the direction of heat flow [146, 147] or when columnar crystals pass a re-entrant corner in a mould [130]. Gandin et al. [148] examined tertiary branching as a competition mechanism for a divergent bicrystal using the $\langle 100 \rangle$ succinonitrile-acetone system. They demonstrated that with higher misalignment, the unfavourably oriented crystal could compete with a favourably oriented crystal via tertiary branching. However, with reduced misalignment, the unfavourably oriented crystal's secondary arms became suppressed, preventing tertiary branching in the unfavourably oriented crystal and instead allowed successful tertiary branching in the favourably orientated crystal. Wagner et al. also showed the unfavourably orientated crystal stabilising against the favourably orientated crystal by the same mechanism [149]. In all of these examples with $\langle 100 \rangle$ dendrites, the unfavourably orientated crystals were misaligned by more than 33^o. This manuscript highlights multiple instances where the misaligned crystals competed by periodic tertiary branching (see colony C in test scenario 1, colony B in test scenario 3, colony C in test scenario 5, and colony B in test scenario 7). However, in contrast to other examples [148, 149], tertiary branching was favoured in the unfavourably orientated crystals with a misalignment as low as 16^o (colony C, test 1). It is likely that this behaviour is a consequence of the $\langle 111 \rangle$ structure where secondary arms have a 19.5^o advantage compared with the $\langle 100 \rangle$

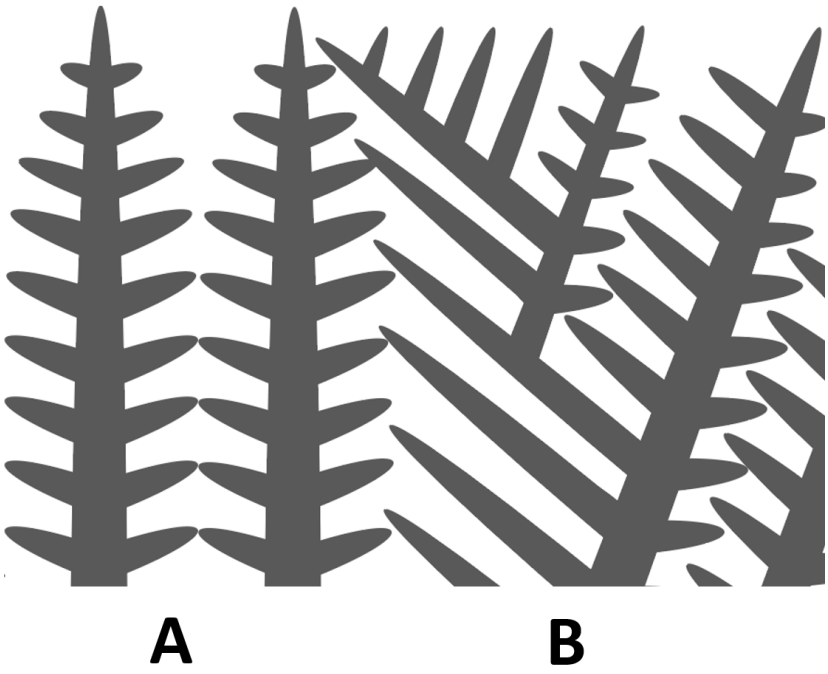

Figure 4.11: Schematic illustration of divergent boundary with ⟨111⟩ dendrites showing competition between favourably oriented colony, A, and unfavourably oriented colony, B, with $\alpha_{1,A} = 0^o$ and $\alpha_{1,B} = -20^o$. Competitive secondary arms and branching by colony B allow it to maintain a grain boundary parallel to the primary growth direction of A.

configuration.

The average misalignment results (figure 4.7 and figure 4.8 (b)) provided a macroscopic average of the competitive crystal growth, where decreasing average and reduction in the variance of the measured misalignment indicates an average agreement with the Walton-Chalmers rule [9, 10]. In this study, the majority of scenarios ultimately tended to agree with the Walton-Chalmers rule by showing either a decrease in the average misalignment or convergence to a single preferential orientation. However, in test scenario 7, the results were significantly different with the average misalignment increasing over the solidification length instead of decreasing and with approximately uniform variance. Moreover, thermal processing conditions of cooling rate and temperature gradient applied in test scenario 7 were the same as test scenario 1. Thus, with similar parameters applied, the different outcomes that were observed were stochastic in nature. The results showed that some pairs of crystal orientations allow the unfavourably oriented crystal to overgrow its favourably oriented neighbour. Hence, depending on the initial seeding, the average misalignment could also increase. The stochastic nature of the outcome is likely dependent on the initial seeding orientations. The crystal colonies' orientation about their primary growth direction could also affect

obedience or disobedience to the Walton-Chalmers rule at individual grain boundaries. Further experiments capable of assessing the 3D crystal orientation are required to fully understand the mechanisms of competition and the outcome in test scenario 7.

4.5 Conclusions

Seven separate scenarios of directional solidification were conducted with controlled cooling rate and temperature gradient; and hence, isotherm speed in order to investigate competitive growth mechanisms in ⟨111⟩ crystals. In-situ footage of the columnar growth was augmented with a bespoke dendrite tip tracking algorithm to provide velocity vectors at the tips of the dendrites; this provided an improved qualitative insight into the mechanisms of competitive growth. This work has provided the first examples of competitive crystal growth with associated tip velocity vectors in directionally solidified ⟨111⟩ crystals. Specific experimental results generally followed the Walton-Chalmers predicted growth behaviour, that is, with a decrease in average misalignment due to favourably oriented crystals outgrowing unfavourably oriented crystal. However, there were instances when the Walton-Chalmers rule was disobeyed since no convergence to a single preferred orientation was demonstrated. In contradiction to the Walton-Chalmers rule, the average misalignment of test scenario 7 increased from 14^o to 28^o over the length of the observed solidification. Moreover, test scenario 1, under the same conditions as test scenario 7 obeyed the Walton-Chalmers rule. It is proposed that the deviation from the Walton-Chalmers rule of competitive growth is probabilistic and likely depends on the initial seeding.

Competition mechanisms at 17 grain-boundaries were detailed in table 4.2 with multiple examples of diverging and converging boundaries provided. Obedience and disobedience to the Walton-Chalmers rule was highlighted with no clear trend to predict whether the rule should be obeyed or not. However, a common observation in all experiments was the ability of secondary and tertiary dendrite arms to compete with the primary arms of neighbouring colonies. In particular, the unfavourably orientated crystals were able to maintain their boundaries with the favourably orientated crystals under divergent neighbouring growth scenarios. Moreover, when the favourably

orientated crystals had some misalignment, the unfavourably oriented crystals could overgrow the favourably orientated crystals parallel to the primary growth direction of the favourably orientated crystals, for example, boundary BC in test scenario 1. A similar mechanism has already been shown in ⟨100⟩ crystals [148, 149]; however, in those scenarios, the unfavourably oriented crystals had at least 33^o misalignment, which allowed secondary arms of those ⟨100⟩ dendrites to achieve sufficiently favourable growth direction and dominate secondary arms of other favourably orientated crystals. In contrast, this manuscript's results showed the same mechanism occurring but with the unfavourably orientated crystals oriented at 16^o. The difference is due to the favourable crystallographic growth direction of secondary arms in ⟨111⟩ dendrites, i.e., the 19.5^o advantage compared with the ⟨100⟩ dendrites. Hence, directional solidification with ⟨111⟩ crystallographic orientations has a higher probability of disobeying the Walton-Chalmers rule than ⟨100⟩ crystals.

It is noted that the Walton-Chalmers rule was initially intended and based on experiments with ⟨100⟩ dendritic growth. While several scenarios showed obedience to the Walton-Chalmers rule, this work contributes to the increasing number of experimentally observed scenarios [149–153] that, in addition to the Walton-Chalmers rule, should be addressed in numerical and theoretical models. The results are novel and provide the first exploration of competitive growth in ⟨111⟩ dendrites, however, further experiments are required to study the selection mechanism in depth. Additionally, further work that compares competitive growth in ⟨100⟩ and ⟨111⟩ dendrites will provide a useful benchmark for validating numerical and theoretical models of competitive growth. It is hoped that the results will add motivation for continued numerical and theoretical modelling of the mechanisms of competitive growth, which are ongoing [126–128, 152–155].

Acknowledgements

This work was supported by the European Space Agency (ESA) [contract number 4200014313NL/SH, CCN009 to AO-99-117] and by ESA PRODEX [contract number 4000110385 CN 3] as part of the CETSOL Microgravity Application Programme. ESA

PRODEX funding is managed by the Irish Space Delegation at Enterprise Ireland.

Chapter 5

Conclusions & Future Work

5.1 Conclusions

The overall aim of this thesis was to develop an experimental facility in combination with image processing and computer-vision techniques for the visualisation and characterisation of dendritic growth structures in the transparent model alloy Neopentyl Glycol-35wt.%(D)Camphor. From this, four objectives were identified and have been addressed throughout Chapters 2 to 4. The objectives of the thesis were as follows:

1. to develop an experimental facility for directional solidification which facilitates in-situ visualisation of the solidification process under controlled cooling rate, temperature gradient and isotherm speed

2. to develop computer vision and image processing techniques for use with the in-situ optical video data for better visualisation and characterisation of micro and macro structure development

3. to provide complementary terrestrial data for microgravity investigations with the NPG-DC system as part of the CETSOL framework

4. to investigate competitive growth mechanisms during directional solidification in the $\langle 111 \rangle$ transparent alloy NPG-35wt.%DC and apply image processing and computer vision techniques to further elucidate competitive growth mechanisms.

Objective 1 was achieved in Chapter 2. An experimental apparatus was developed to investigate in-situ directional solidification using a transparent model alloy, Neopentyl Glycol-35wt.%(D)Camphor. The optical microscopic video data and thermal instrumentation facilitated the characterisation of dendritic structures that formed with controlled directional solidification.

Objective 2 was achieved throughout Chapters 2, 3 and 4. Chapter 2 described the development of an image processing technique for in-situ tracking of the solidification front's position and speed. Historically, isotherm speed has been widely accepted as a reasonable approximation for growth rates and is necessarily used for ex-situ experiments, where visual access to the solidification front is not possible. Growth rates were measured with both the automated front-tracking technique and the traditional isotherm speed technique and were benchmarked against manual growth rate measurements. In all cases, the tracker speed was significantly more reliable than isotherm speed and showed good temporal agreement with manual measurements for cases of fully columnar and fully equiaxed growth. The work showed the isotherm speed to be in error up to 19%, which is significant. In contrast, the front-tracking technique compared better than 3% error from manual measurements. Chapter 3 described a new computer vision algorithm to automatically track the position and velocity of multiple columnar dendrite tips from in-situ video data provided by the experimental facility. The new computer vision algorithm was demonstrated to be highly beneficial since, with 385 dendrite tip tracked, it provided statistical and quantitative data otherwise too laborious to capture manually. In addition to the scaling up of quantitative data analysis, the algorithm's visual results enhanced the ability to make qualitative observations. This was demonstrated in chapter 4, where the multiple dendrite tip tracking helped describe competitive growth mechanisms in neighbouring columnar grains.

Preparations are currently underway within the CETSOL group to upload hypoeutectic NPG-DC samples to the Materials Science Glovebox onboard the International Space Station (ISS). Experiments will be conducted under microgravity conditions for longer durations than could be provided within sounding rocket missions. Hence, the ISS experiments will facilitate microgravity dendritic growth at a smaller undercooling

range without complicating buoyancy-driven phenomena such as thermosolutal flow and sedimentation. In the context of the CETSOL project, objective 3 of this thesis aimed to provide complementary terrestrial experiments with the NPG-DC alloy system for comparison with microgravity experiments conducted both on the ISS and in microgravity sounding rocket missions such as the TRACE campaign. The terrestrial and microgravity experimental results with NPG-DC will provide useful benchmark data for validating numerical and theoretical models of solidification.

Objective 3 was achieved with experimental investigations in Chapter's 2 and 3. Chapter 2 described five directional solidification test scenarios with controlled conditions of cooling rate, temperature gradient and isotherm speed. The experiments produced three scenarios that led to a fully columnar texture and two scenarios that led to a fully equiaxed texture in the transparent model alloy. The reported processing conditions will aid in planning experiments with the NPG-DC system onboard the international space station, where conditions leading to columnar or equiaxed structures will be a primary focus [84]. Chapter 3 described a further six directional solidification scenarios. Each test scenario was predominantly columnar and showed close to steady growth conditions as columnar tips crossed an internal temperature probe with 50 μm diameter wire. A total of 95 dendrite tips were observed to cross an internal thermocouple in the melt and provided instantaneous measurement of the dendrite tip velocity and undercooling. Comparison of results with similar microgravity experimental results [44] showed a marked difference between the terrestrial and microgravity data. A comparison was made to the classical LGK growth law based on solute diffusion without convection. At the same growth rates, terrestrial undercoolings were between 0.41 and 0.68 times the predicted growth rates. However, when modifications were made to the theoretical LGK to compensate for the effect of convection, results gave good agreement for finite boundary layers of lengths in the range 2.5 to 7.0 μm.

Objective 4 was achieved in Chapter 4. This work provided the first examples of competitive crystal growth with associated tip velocity vectors in directionally solidified $\langle 111 \rangle$ crystals. Seven test scenarios were conducted to investigate competitive growth from initially randomly oriented seeding. The change in average misalignment

and spread of the misalignment versus the growth distance provided a macroscopic overview of obedience or disobedience to the Walton-Chalmers rule. Specific experimental results generally followed the Walton-Chalmers predicted growth behaviour, with a decrease in average misalignment due to favourably oriented crystals outgrowing unfavourably oriented crystal. However, test scenario 7 contradicted the Walton-Chalmers rule, where the average misalignment increased from 14^o to 28^o over the length of the observed solidification. Moreover, test scenario 1, under the same conditions as test scenario 7 obeyed the Walton-Chalmers rule. It is proposed that the deviation from the Walton-Chalmers rule of competitive growth is probabilistic and likely depends on the initial seeding.

Obedience and disobedience to the Walton-Chalmers rule was highlighted at grain boundaries with no clear trend to predict whether the rule should be obeyed or not. However, a common observation in all experiments was secondary and tertiary dendrite arms' ability to compete with neighbouring colonies' primary arms. When the favourably orientated crystals had some misalignment, the unfavourably oriented crystals could overgrow the favourably orientated crystals parallel to the favourably oriented crystals' primary growth direction. A similar mechanism in $\langle 100 \rangle$ crystals is described in the literature [148, 149]; however, in those scenarios, the unfavourably oriented crystals had at least 33^o misalignment. In contrast, this manuscript's results showed the same mechanism occurring but with the unfavourably orientated crystals oriented at 16^o. The difference is due to the favourable crystallographic growth direction of secondary arms in $\langle 111 \rangle$ dendrites, i.e., the 19.5^o advantage compared with the $\langle 100 \rangle$ dendrites. Hence, directional solidification with $\langle 111 \rangle$ crystallographic orientations has a higher probability of disobeying the Walton-Chalmers rule than $\langle 100 \rangle$ crystals.

Progress in solidification science requires continuous development of numerical and theoretical models of solidification combined with well-defined and accurately quantified experiments that allow model validation to take place. This thesis presented a newly developed experimental facility and methodology for investigating in-situ directional solidification in transparent model alloys with accurate control of temperature

gradient, cooling rate and isotherm speed, and a well characterised thermal environment. Moreover, the experimental results throughout chapters two, three and four have provided new data which will allow for code verification to take place. The results have been compared with microgravity data available in the literature and provide complementary data for the NPG-DC microgravity experiments planned onboard the ISS. Further progress in solidification science also requires the ability to characterise bulk directional solidification experiments. The newly developed multiple dendrite tip tracking algorithm presented in Chapter three will be useful for the broader solidification community for scaling up quantitative data extraction from in-situ videography of directional solidification and for enabling statistical analysis of dendritic forests. This work has also provided the first known tests of competitive growth in-situ with $\langle 111 \rangle$ dendrites. It was discovered that secondary dendrite arms in $\langle 111 \rangle$ dendrites are more competitive than secondaries of $\langle 100 \rangle$ dendrites and that this is likely due to the 19.5^o advantage of $\langle 111 \rangle$ secondaries. Results of competitive growth in $\langle 111 \rangle$ dendrites highlight an opportunity to further investigate mechanisms of competitive growth in the $\langle 111 \rangle$ dendrite orientation.

5.2 Future Work

- The objective of this work in the context of the CETSOL project was to provide complementary terrestrial data for microgravity investigations with the NPG-DC system. While this work compared terrestrial results with the TRACE campaign (TEXUS-47 sounding rocket mission), further comparisons should be made to future microgravity experiments which are planned for the International Space Station using the same transparent model alloy system. In particular, results of dendrite tip velocity and undercooling.

- The newly developed multiple dendrite tip tracking algorithm should be validated against manually determined dendrite tip position and velocity. The algorithm should also be applied to other in-situ video data of columnar dendritic growth.

- Results in the present work showed that tip velocity versus undercooling changes

significantly for a different temperature gradient. Further experimental work is needed to establish the trend. Future work should investigate the effect of imposed temperature gradient on dendrite growth.

- Mechanisms of competitive growth should be studied further using two nominally orientated $\langle 111 \rangle$ dendrites. Dendrites with approximately nominal orientation could be obtained using stingers as in the work of Glicksman et al. [78, 156]. Here, a stinger would require freedom for axial rotation and angular displacement to correct for small possible misalignment in a given seeded crystals. The same study should be implemented with $\langle 100 \rangle$ dendrites using NPG-20wt.%DC. This would provide valuable insights into mechanisms of competitive growth as well as important benchmark data for theoretical and numerical models on competitive growth.

- Preliminary absorption fluorescence spectra indicated that 240 – 250 nm UV radiation fluoresces liquid NPG-35wt.%DC. Further work should examine the possibility of fluorescing the liquid alloy to visualise thermosolutal flow or potentially measure composition fields for experiments with rectangular sample geometry.

- Further experimental investigations should compare upwards and downwards directional solidification extending the work of [66]. The work highlighted the effect of the solidification direction with respect to gravity on mechanisms of micro- to macro-structure formation.

Bibliography

[1] S. Wetzel, "Census of World Casting Production," *Modern Casting*, vol. 9, no. 12, p. 22, 2019.

[2] W. Kurz, D. J. Fisher, and R. Trivedi, "Progress in modelling solidification microstructures in metals and alloys: dendrites and cells from 1700 to 2000," *International Materials Reviews*, vol. 64, pp. 311–354, 8 2019.

[3] P. W. Bridgman, "Certain Physical Properties of Single Crystals of Tungsten, Antimony, Bismuth, Tellurium, Cadmium, Zinc, and Tin," *Proceedings of the American Academy of Arts and Sciences*, vol. 60, no. 6, pp. 305–383, 1925.

[4] J. Hutt and D. StJohn, "The origins of the equiaxed zone -Review of theoretical and experimental work," *International Journal of Cast Metals Research*, vol. 11, pp. 13–22, 7 1998.

[5] J. A. Spittle, "Columnar to equiaxed grain transition in as solidified alloys," *International Materials Reviews*, vol. 51, no. 4, pp. 247–269, 2006.

[6] W. U. Mirihanage, H. Dai, H. Dong, and D. J. Browne, "Computational modeling of columnar to equiaxed transition in alloy solidification," *Advanced Engineering Materials*, vol. 15, no. 4, pp. 216–229, 2013.

[7] E. O. Hall, "The deformation and ageing of mild steel: III Discussion of results," *Proceedings of the Physical Society. Section B*, vol. 64, no. 9, pp. 747–753, 1951.

[8] N. J. Petch, "The Cleavage Strength of Polycrystals," *Journal of the Iron and Steel Institute*, vol. 178, pp. 25 – 28, 1953.

[9] D. Walton and B. Chalmers, "The Origin of the Preferred Orientation in the Columnar Zone of Ingots," *Transactions of the Metallurgical Society of AIME, Vol. 215*, vol. 215, no. June, pp. 3–13, 1959.

[10] B. Chalmers, *Principles of solidification*. New York, N.Y., Wiley, 1964.

[11] F. Versnyder and M. Shank, "The development of columnar grain and single crystal high temperature materials through directional solidification," *Materials Science and Engineering*, vol. 6, no. 4, pp. 214–247, 1970.

[12] A. Papapetrou, "Untersuchungen über dendritisches Wachstum von Kristallen," *Zeitschrift für Kristallographie-Crystalline Materials*, vol. 92, no. 1, pp. 89–130, 1935.

[13] K. A. Jackson and J. D. Hunt, "Transparent compounds that freeze like metals," *Acta Metallurgica*, vol. 13, no. 11, pp. 1212–1215, 1965.

[14] C. Y. Wang and C. Beckermann, "Equiaxed dendritic solidification with convection: Part I. Multiscale/multiphase modeling," *Metallurgical and Materials Transactions A: Physical Metallurgy and Materials Science*, vol. 27, no. 9, pp. 2754–2764, 1996.

[15] C. A. Gandin and M. Rappaz, "A coupled finite element-cellular automaton model for the prediction of dendritic grain structures in solidification processes," *Acta Metallurgica Et Materialia*, vol. 42, no. 7, pp. 2233–2246, 1994.

[16] M. E. Glicksman, M. B. Koss, L. T. Bushnell, J. C. Lacombe, and E. A. Winsa, "Dendritic Growth of Succinonitrile in Terrestrial and Micro gravity Conditions as a Test of Theory," *ISIJ International*, vol. 35, no. 6, pp. 604–610, 1995.

[17] A. Viardin, L. Sturz, G. Zimmermann, and M. Apel, "Phase-field modeling of the columnar-to-equiaxed transition in neopentylglycol-camphor alloy solidification," *Journal of Physics: Conference Series*, vol. 327, p. 012004, 12 2011.

[18] A. J. Melendez and C. Beckermann, "Measurements of dendrite tip growth and sidebranching in succinonitrile-acetone alloys," *Journal of Crystal Growth*, vol. 340, no. 1, pp. 175–189, 2012.

[19] F. L. Mota, N. Bergeon, D. Tourret, A. Karma, R. Trivedi, and B. Billia, "Initial transient behavior in directional solidification of a bulk transparent model alloy in a cylinder," *Acta Materialia*, vol. 85, pp. 362–377, 2015.

[20] T. Sato, W. Kurz, and K. Ikawa, "Experiments on Dendrite Branch Detachment in the Succinonitrile-Camphor Alloy.," 1987.

[21] G. L. Ding, W. D. Huang, X. Huang, X. Lin, and Y. H. Zhou, "On primary dendritic spacing during unidirectional solidification," *Acta Materialia*, vol. 44, no. 9, pp. 3705–3709, 1996.

[22] D. Ma, "Development of dendrite array growth during alternately changing solidification condition," *Journal of Crystal Growth*, vol. 260, pp. 580–589, 1 2004.

[23] H. Esaka, H. Daimon, Y. Natsume, K. Ohsasa, and M. Tamura, "Growth Direction of Cellular and Dendritic Interface in a Constrained Growth Condition," *Materials Transactions*, vol. 43, no. 6, pp. 1312–1317, 2002.

[24] R. H. Mathiesen, L. Arnberg, F. Mo, T. Weitkamp, and A. Snigirev, "Time resolved X-ray imaging of dendritic growth in binary alloys," *Physical Review Letters*, vol. 83, no. 24, pp. 5062–5065, 1999.

[25] O. Ludwig, M. Dimichiel, L. Salvo, M. Suéry, and P. Falus, "In-situ three-dimensional microstructural investigation of solidification of an Al-Cu alloy by ultrafast x-ray microtomography," *Metallurgical and Materials Transactions A*, vol. 36, no. 6, pp. 1515–1523, 2005.

[26] M. A. Salgado-Ordorica, J. L. Desbiolles, and M. Rappaz, "Study of the twinned dendrite tip shape I: Phase-field modeling," *Acta Materialia*, vol. 59, no. 13, pp. 5074–5084, 2011.

[27] J. Friedli, J. L. Fife, P. Di Napoli, and M. Rappaz, "Dendritic growth morphologies in Al-Zn alloys - Part I: X-ray tomographic microscopy," *Metallurgical and Materials Transactions A: Physical Metallurgy and Materials Science*, vol. 44, no. 12, pp. 5522–5531, 2013.

[28] D. J. Browne, F. García-Moreno, H. Nguyen-Thi, G. Zimmermann, F. Kargl, R. H. Mathiesen, A. Griesche, and O. Minster, "Overview of In Situ X-ray Studies of Light Alloy Solidification in Microgravity," *Journal of Minerals, Metals and Materials Society*, pp. 581–590, 2017.

[29] Y. Wang, S. Jia, M. Wei, L. Peng, Y. Wu, and X. Liu, "Research progress on solidification structure of alloys by synchrotron X-ray radiography: A review," *Journal of Magnesium and Alloys*, vol. 8, no. 2, pp. 396–413, 2020.

[30] R. H. Mathiesen, L. Arnberg, K. Ramsøskar, T. Weitkamp, C. Rau, and A. Snigirev, "Time-resolved X-ray imaging of aluminum alloy solidification processes," *Metallurgical and Materials Transactions B: Process Metallurgy and Materials Processing Science*, vol. 33, no. 4, pp. 613–623, 2002.

[31] D. Ruvalcaba, R. H. Mathiesen, D. G. Eskin, L. Arnberg, and L. Katgerman, "In situ observations of dendritic fragmentation due to local solute-enrichment during directional solidification of an aluminum alloy," *Acta Materialia*, vol. 55, no. 13, pp. 4287–4292, 2007.

[32] B. Wang, D. Tan, T. L. Lee, J. C. Khong, F. Wang, D. Eskin, T. Connolley, K. Fezzaa, and J. Mi, "Ultrafast synchrotron X-ray imaging studies of microstructure fragmentation in solidification under ultrasound," *Acta Materialia*, vol. 144, pp. 505–515, 2018.

[33] E. Liotti, A. Lui, R. Vincent, S. Kumar, Z. Guo, T. Connolley, I. P. Dolbnya, M. Hart, L. Arnberg, R. H. Mathiesen, and P. S. Grant, "A synchrotron X-ray radiography study of dendrite fragmentation induced by a pulsed electromagnetic field in an Al-15Cu alloy," *Acta Materialia*, vol. 70, pp. 228–239, 2014.

[34] R. H. Mathiesen, L. Arnberg, P. Bleuet, and A. Somogyi, "Crystal fragmentation and columnar-to-equiaxed transitions in Al-Cu studied by synchrotron X-ray video microscopy," *Metallurgical and Materials Transactions A*, vol. 37, no. 8, pp. 2515–2524, 2006.

[35] H. Nguyen-Thi, G. Reinhart, N. Mangelinck-Noël, H. Jung, B. Billia, T. Schenk, J. Gastaldi, J. Härtwig, and J. Baruchel, "In-Situ and Real-Time Investigation of Columnar-to-Equiaxed Transition in Metallic Alloy," *Metallurgical and Materials Transactions A*, vol. 38, no. 7, pp. 1458–1464, 2007.

[36] Q. Dong, J. Zhang, J. Dong, H. Xie, Z. Li, Y. Dai, Y. Liu, and B. Sun, "In situ observation of columnar-to-equiaxed transition in directional solidification using synchrotron X-radiation imaging technique," *Materials Science and Engineering: A*, vol. 530, pp. 271–276, 2011.

[37] G. Reinhart, H. Nguyen-Thi, N. Mangelinck-Noël, B. Billia, T. Schenk, and J. Baruchel, "CET during the solidification of refined Al-3.5wt%Ni alloys and characterization of the subsequent grain structure," *IOP Conference Series: Materials Science and Engineering*, vol. 27, no. 1, 2011.

[38] N. Limodin, L. Salvo, E. Boller, M. Suéry, M. Felberbaum, S. Gailliègue, and K. Madi, "In situ and real-time 3-D microtomography investigation of dendritic solidification in an Al–10wt.% Cu alloy," *Acta Materialia*, vol. 57, no. 7, pp. 2300–2310, 2009.

[39] J. L. Fife, J. W. Gibbs, E. B. Gulsoy, C.-L. Park, K. Thornton, and P. W. Voorhees, "The dynamics of interfaces during coarsening in solid–liquid systems," *Acta Materialia*, vol. 70, pp. 66–78, 2014.

[40] N. Bergeon, R. Trivedi, B. Billia, B. Echebarria, A. Karma, S. Liu, C. Weiss, and N. Mangelinck, "Necessity of investigating microstructure formation during directional solidification of transparent alloys in 3D," *Advances in Space Research*, vol. 36, no. 1, pp. 80–85, 2005.

[41] L. A. Tennenhouse, M. B. Koss, J. C. LaCombe, and M. E. Glicksman, "Use of microgravity to interpret dendritic growth kinetics at small supercoolings," *Journal of Crystal Growth*, vol. 174, no. 1-4, pp. 82–89, 1997.

[42] V. Pines, A. Chait, and M. Zlatkowski, "Dynamic scaling in dendritic growth: significance of the initial nucleus size," *Journal of Crystal Growth*, vol. 182, no. 1, pp. 219–226, 1997.

[43] E. Liotti, C. Arteta, A. Zisserman, A. Lui, V. Lempitsky, and P. S. Grant, "Crystal nucleation in metallic alloys using x-ray radiography and machine learning," *Science Advances*, vol. 4, no. 4, pp. 1–9, 2018.

[44] L. Sturz and G. Zimmermann, "In-situ and real-time investigation of the columnar-equiaxed transition in the transparent alloy system neopentylglycol-camphor onboard the sounding rocket TEXUS-47," *Journal of Physics: Conference Series*, vol. 327, no. 1, pp. 1–9, 2011.

[45] R. H. Mathiesen, L. Arnberg, H. Nguyen-Thi, and B. Billia, "In Situ X-Ray Video Microscopy as a Tool in Solidification Science," *JOM*, vol. 64, no. 1, pp. 76–82, 2012.

[46] A. Murphy, W. Mirihanage, D. Browne, and R. Mathiesen, "Equiaxed dendritic solidification and grain refiner potency characterised through in situ X-radiography," *Acta Materialia*, vol. 95, pp. 83–89, 8 2015.

[47] S. McFadden, R. P. Mooney, L. Sturz, and G. Zimmermann, "A Nucleation Progenitor Function approach to polycrystalline equiaxed solidification modelling with application to a microgravity transparent alloy experiment observed in-situ," *Acta Materialia*, vol. 148, pp. 289–299, 2018.

[48] J. Miller, M. Strangwood, S. Steinbach, and N. Warnken, "Skeletonisation to Find the Centre of Dendrites Traced from a 2D Microstructural Image," *Proceedings of the 5th Decennial International Conference on Solidification Processing*, no. August, pp. 2–5, 2017.

[49] B. Nenchev, J. Strickland, K. Tassenberg, S. Perry, S. Gill, and H. Dong, "Automatic recognition of dendritic solidification structures: DenMap," *Journal of Imaging*, vol. 6, no. 4, pp. 1–12, 2020.

[50] T. Strohmann, K. Bugelnig, E. Breitbarth, F. Wilde, T. Steffens, H. Germann, and G. Requena, "Semantic segmentation of synchrotron tomography of multiphase Al-Si alloys using a convolutional neural network with a pixel-wise weighted loss function," *Scientific Reports*, vol. 9, no. 1, p. 19611, 2019.

[51] N. Wang, Y. Tang, Y. Wu, Y. Zhang, Y. Dai, J. Zhang, R. Zhang, Y. Xu, and B. Sun, "Dynamic evolution of microstructure morphology in thin-sample solidification: Deep learning assisted synchrotron X-ray radiography," *Materials Characterization*, vol. 181, p. 111451, 2021.

[52] C. Shashank Kaira, X. Yang, V. De Andrade, F. De Carlo, W. Scullin, D. Gursoy, and N. Chawla, "Automated correlative segmentation of large Transmission X-ray Microscopy (TXM) tomograms using deep learning," *Materials Characterization*, vol. 142, pp. 203–210, 2018.

[53] A. Baskaran, G. Kane, K. Biggs, R. Hull, and D. Lewis, "Adaptive characterization of microstructure dataset using a two stage machine learning approach," *Computational Materials Science*, vol. 177, no. February, p. 109593, 2020.

[54] J. Masci, U. Meier, D. C. Ciresan, J. Schmidhuber, and G. Fricout, "Steel defect classification with Max-Pooling Convolutional Neural Networks," *The 2012 International Joint Conference on Neural Networks (IJCNN)*, pp. 1–6, 2012.

[55] S. M. Azimi, D. Britz, M. Engstler, M. Fritz, and F. Mücklich, "Advanced Steel Microstructural Classification by Deep Learning Methods," *Scientific Reports*, vol. 8, no. 1, p. 2128, 2018.

[56] M. E. Glicksman, M. B. Koss, and E. A. Winsa, "Dendritic Growth Velocities in Microgravity," *Physical Review Letters*, vol. 73, no. 4, pp. 573–576, 1994.

[57] M. B. Koss, J. C. LaCombe, L. A. Tennenhouse, M. E. Glicksman, and E. A. Winsa, "Dendritic growth tip velocities and radii of curvature in microgravity,"

Metallurgical and Materials Transactions A: Physical Metallurgy and Materials Science, vol. 30, no. 12, pp. 3177–3190, 1999.

[58] M. H. Burden and J. D. Hunt, "Some observations on primary dendrite spacings," *Metal Science*, vol. 10, no. 5, pp. 156–158, 1976.

[59] J. E. Spinelli, D. M. Rosa, I. L. Ferreira, and A. Garcia, "Influence of melt convection on dendritic spacings of downward unsteady-state directionally solidified Al-Cu alloys," *Materials Science and Engineering A*, vol. 383, no. 2, pp. 271–282, 2004.

[60] J. E. Spinelli, I. L. Ferreira, and A. Garcia, "Influence of melt convection on the columnar to equiaxed transition and microstructure of downward unsteady-state directionally solidified Sn-Pb alloys," *Journal of Alloys and Compounds*, vol. 384, no. 1-2, pp. 217–226, 2004.

[61] J. E. Spinelli, M. D. Peres, and A. Garcia, "Thermosolutal convective effects on dendritic array spacings in downward transient directional solidification of Al-Si alloys," *Journal of Alloys and Compounds*, vol. 403, no. 1-2, pp. 228–238, 2005.

[62] J. E. Spinelli, O. F. L. Rocha, and A. Garcia, "The influence of melt convection on dendritic spacing of downward unsteady-state directionally solidified Sn-Pb alloys," *Materials Research*, vol. 9, no. 1, pp. 51–57, 2006.

[63] F. Wang, D. Ma, J. Zhang, L. Liu, S. Bogner, and A. Bührig-Polaczek, "Effect of local cooling rates on the microstructures of single crystal CMSX-6 superalloy: A comparative assessment of the Bridgman and the downward directional solidification processes," *Journal of Alloys and Compounds*, vol. 616, pp. 102–109, 2014.

[64] F. Wang, D. Ma, J. Zhang, and A. Bührig-Polaczek, "Investigation of segregation and density profiles in the mushy zone of CMSX-4 superalloys solidified during downward and upward directional solidification processes," *Journal of Alloys and Compounds*, vol. 620, pp. 24–30, 2015.

[65] C. Brito, F. Bertelli, M. A. Castanho, P. R. Goulart, N. Cheung, J. E. Spinelli, and A. Garcia, "Upward and downward unsteady-state directional solidification of a hypoeutectic Al-3wt.%Mg alloy," *Ciencia e Tecnologia dos Materiais*, vol. 29, pp. e65–e70, 1 2017.

[66] T. Hughes, S. McFadden, and A. Robinson, "In-situ observation of the effects of gravity direction on directional solidification of the transparent alloy NPG-35wt%-DC," in *Solidification and Gravity VII.* (A. Roósz, Z. Veres, M. Svéda, and G. Karacs, eds.), (Miskolc-Lillafüred, Ungarn), pp. 63–68, Hal, 2018.

[67] T. Hughes, S. McFadden, and A. J. Robinson, "A front-tracking measurement technique for in-situ columnar and equiaxed structure growth with controlled solidification," *Measurement Science and Technology*, vol. 32, no. 4, p. 045903, 2020.

[68] L. Sturz, M. Hamacher, J. Eiken, G. Zimmermann, V. Access, and E. L. Sturzaccess-technologyde, "Multiple Equiaxed Dendrite Interaction Investigated on MASER-13," *Proc. of the 23rd ESA Symposium on European Rocket and Balloon Programmes and Related Research*, vol. 23, 2017.

[69] W. R. Osório, P. R. Goulart, G. A. Santos, C. M. Neto, and A. Garcia, "Effect of dendritic arm spacing on mechanical properties and corrosion resistance of Al 9 wt pct Si and Zn 27 wt pct Al alloys," *Metallurgical and Materials Transactions A: Physical Metallurgy and Materials Science*, vol. 37, no. 8, pp. 2525–2538, 2006.

[70] P. R. Goulart, J. E. Spinelli, W. R. Osório, and A. Garcia, "Mechanical properties as a function of microstructure and solidification thermal variables of Al-Si castings," *Materials Science and Engineering A*, vol. 421, no. 1-2, pp. 245–253, 2006.

[71] R. P. Mooney, S. McFadden, M. Rebow, and D. J. Browne, "A front tracking model for transient solidification of Al-7wt%Si in a Bridgman furnace," *Transactions of the Indian Institute of Metals*, vol. 65, no. 6, pp. 527–530, 2012.

[72] S. Battaglioli, A. J. Robinson, and S. McFadden, "Axisymmetric front tracking model for the investigation of grain structure evolution during directional solidification," *International Journal of Heat and Mass Transfer*, vol. 115, pp. 592–605, 2017.

[73] H. Yasuda, I. Ohnaka, K. Kawasaki, A. Sugiyama, T. Ohmichi, J. Iwane, and K. Umetani, "Direct observation of stray crystal formation in unidirectional solidification of Sn-Bi alloy by X-ray imaging," *Journal of Crystal Growth*, vol. 262, no. 1-4, pp. 645–652, 2004.

[74] R. H. Mathiesen and L. Arnberg, "X-ray radiography observations of columnar dendritic growth and constitutional undercooling in an Al-30wt%Cu alloy," *Acta Materialia*, vol. 53, no. 4, pp. 947–956, 2005.

[75] G. Reinhart, N. Mangelinck-Noël, H. Nguyen-Thi, T. Schenk, J. Gastaldi, B. Billia, P. Pino, J. Härtwig, and J. Baruchel, "Investigation of columnar-equiaxed transition and equiaxed growth of aluminium based alloys by X-ray radiography," *Materials Science and Engineering A*, vol. 413-414, pp. 384–388, 2005.

[76] T. Schenk, H. N. Thi, J. Gastaldi, G. Reinhart, V. Cristiglio, N. Mangelinck-Noël, H. Klein, J. Härtwig, B. Grushko, B. Billia, and J. Baruchel, "Application of synchrotron X-ray imaging to the study of directional solidification of aluminium-based alloys," *Journal of Crystal Growth*, vol. 275, no. 1-2, pp. 201–208, 2005.

[77] G. Reinhart, A. Buffet, H. Nguyen-Thi, B. Billia, H. Jung, N. Mangelinck-Noël, N. Bergeon, T. Schenk, J. Härtwig, and J. Baruchel, "In-situ and real-time analysis of the formation of strains and microstructure defects during solidification of Al-3.5 Wt Pct Ni alloys," *Metallurgical and Materials Transactions A: Physical Metallurgy and Materials Science*, vol. 39 A, no. 4, pp. 865–874, 2008.

[78] S. C. Huang and M. E. Glicksman, "Fundamentals of dendritic solidification. I - Steady-state tip growth. II - Development of sidebranch structure," *Acta Metallurgica*, vol. 29, no. 1, pp. 717–734, 1981.

[79] W. Huang and L. Wang, "Solidification researches using transparent model materials - A review," *Science China Technological Sciences*, vol. 55, no. 2, pp. 377–386, 2012.

[80] H. Nguyen-thi, "In situ observation of solidification patterns in diffusive conditions," *Acta Materialia*, vol. 108, pp. 325–346, 2016.

[81] M. Ahmadein, M. Wu, L. Sturz, G. Zimmermann, and A. Ludwig, "Numerical investigation of solidification and CET of the transparent alloy NPG-37.5 wt.% DC in microgravity "TRACE" experiment," *IOP Conference Series: Materials Science and Engineering*, vol. 117, no. 1, pp. 68 – 74, 2016.

[82] R. P. Mooney, L. Sturz, G. Zimmermann, and S. McFadden, "Thermal characterisation with modelling for a microgravity experiment into polycrystalline equiaxed dendritic solidification with in-situ observation," *International Journal of Thermal Sciences*, vol. 125, no. April 2017, pp. 283–292, 2018.

[83] L. Sturz, M. Hamacher, and G. Zimmermann, "In-situ observation of equiaxed dendritic growth and interaction in microgravity," in *6th Decennial International Conference on Solidification Processing* (Z. Fan, ed.), (Old Windsor), pp. 300–303, Brunel University London Press, 2017.

[84] A. Ludwig, J. Mogeritsch, M. Kolbe, G. Zimmermann, L. Sturz, N. Bergeon, B. Billia, G. Faivre, S. Akamatsu, S. Bottin-Rousseau, and D. Voss, "Advanced solidification studies on transparent alloy systems: A new european solidification insert for material science glovebox on board the international space station," *Jom*, vol. 64, no. 9, pp. 1097–1101, 2012.

[85] W. J. Boettinger, S. R. Coriell, A. L. Greer, A. Karma, W. Kurz, M. Rappaz, and R. Trivedi, "Solidification Microstructures: Recent Developments, Future Directions," *Acta Materialia*, vol. 48, pp. 43–70, 2000.

[86] M. Asta, C. Beckermann, A. Karma, W. Kurz, R. Napolitano, M. Plapp, G. Purdy, M. Rappaz, and R. Trivedi, "Solidification microstructures and solid-

state parallels: Recent developments, future directions," *Acta Materialia*, vol. 57, no. 4, pp. 941–971, 2009.

[87] T. Bower, H. Brody, and M. Fleming, "Measurements of Solute Redistribution in Dendritic Solidification," *Transaction of the Metallurgical Society of AIME*, vol. 236, pp. 624–633, 1966.

[88] M. Piccardi, "Background subtraction techniques in surface analysis," *IEEE Int. Conf. on Systems, Man and Cybernetics*, pp. 3099–3104, 2004.

[89] S.-C. S. Cheung and C. Kamath, "Robust techniques for background subtraction in urban traffic video," *Proc. SPIE-Int. Soc. Opt. Eng*, p. 881–892, 2003.

[90] J. E. Santoyo-Morales and R. Hasimoto-Beltran, "Video Background subtraction in complex environments," *Journal of Applied Research and Technology*, vol. 12, no. 3, pp. 527–537, 2014.

[91] Y. Benezeth, P.-M. Jodoin, B. Emile, H. Laurent, C. Rosenberger, Y. Benezeth, P.-m. Jodoin, B. Emile, H. Laurent, and C. Rosenberger, "Comparative study of background subtraction algorithms," *Journal of Electronic Imaging*, vol. 19, no. 3, pp. 1–11, 2010.

[92] J. Shi and C. Tomasi, "Good Features to Track," *Proceedings of IEEE Conference on Computer Vision and Pattern Recognition*, pp. 593–600, 1994.

[93] G. Zimmermann, M. Hamacher, and L. Sturz, "Effect of zero, normal and hypergravity on columnar dendritic solidification and the columnar-to-equiaxed transition in Neopentylglycol-(D)Camphor alloy," *Journal of Crystal Growth*, vol. 512, pp. 47–60, 4 2019.

[94] W. Kurz, M. Rappaz, and R. Trivedi, "Progress in modelling solidification microstructures in metals and alloys. Part II: dendrites from 2001 to 2018," *International Materials Reviews*, vol. 66, no. 1, pp. 30–76, 2021.

[95] G. Zimmermann, M. Hamacher, L. Sturz, V. Access, and E. G. Zimmermannaccess-technologyde, "Columnar-to-equiaxed transition in the

transparent alloy system NPG-DC observed in the low-gravity and normal gravity experiment TRACE-3," *Proc. of the 23rd ESA Symposium on European Rocket and Balloon Programmes and Related Research*, vol. 23, 2017.

[96] J. Mihailovic and C. Beckermann, "Development of a two-dimensional liquid species concentration measurement technique based on absorptiometry," *Experimental Thermal and Fluid Science*, vol. 10, no. 1, pp. 113–123, 1995.

[97] A. Buffet, H. Nguyen Thi, A. Bogno, T. Schenk, N. Mangelinck-Noël, G. Reinhart, N. Bergeon, B. Billia, and J. Baruchel, "Measurement of solute profiles by means of synchrotron X-ray radiography during directional solidification of Al - 4 wt% Cu alloys," *Materials Science Forum*, vol. 649, no. January 2014, pp. 331–336, 2010.

[98] A. Bogno, H. Nguyen-Thi, A. Buffet, G. Reinhart, B. Billia, N. Mangelinck-Noël, N. Bergeon, J. Baruchel, and T. Schenk, "Analysis by synchrotron X-ray radiography of convection effects on the dynamic evolution of the solid-liquid interface and on solute distribution during the initial transient of solidification," *Acta Materialia*, vol. 59, no. 11, pp. 4356–4365, 2011.

[99] M. Becker, S. Klein, and F. Kargl, "In-situ solute measurements with a laboratory polychromatic microfocus X-ray source during equiaxed solidification of an Al-Ge alloy," *Scripta Materialia*, vol. 124, pp. 34–37, 2016.

[100] F. L. Mota, K. Ji, T. Lyons, L. L. Strutzenberg, R. Trivedi, A. Karma, and N. Bergeon, "In situ observation of growth dynamics in DECLIC Directional Solidification Insert onboard ISS: DSI-R flight campaign," in *Proceedings of the 70th International Astronautical Congress*, (Washington, United States), 2019.

[101] G. P. Ivantsov, "The temperature field around a spherical, cylindrical, or pointed crystal growing in a cooling solution," in *Dokl. Akad. Nauk SSSR*, vol. 58, pp. 567–569, 1947.

[102] J. Lipton, M. E. Glicksman, and W. Kurz, "Dendritic growth into undercooled alloy metals," *Materials Science and Engineering*, vol. 65, no. 1, pp. 57–63, 1984.

[103] J. S. Langer and J. Müller-Krumbhaar, "Stability effects in dendritic crystal growth," *Journal of Crystal Growth*, vol. 42, no. C, pp. 11–14, 1977.

[104] B. Cantor and A. Vogel, "Dendritic solidification and fluid flow," *Journal of Crystal Growth*, vol. 41, no. 1, pp. 109–123, 1977.

[105] R. Ananth and W. N. Gill, "Self-consistent theory of dendritic growth with convection," *Journal of Crystal Growth*, vol. 108, no. 1-2, pp. 173–189, 1991.

[106] D. Canright and S. H. Davis, "Buoyancy effects of a growing, isolated dendrite," *Journal of Crystal Growth*, vol. 114, no. 1-2, pp. 153–185, 1991.

[107] Q. Li and C. Beckermann, "Modeling of free dendritic growth of succinonitrile-acetone alloys with thermosolutal melt convection," *Journal of Crystal Growth*, vol. 236, no. 1-3, pp. 482–498, 2002.

[108] S. McFadden and D. J. Browne, "A generalised version of an Ivantsov-based dendrite growth model incorporating a facility for solute measurement ahead of the tip," *Computational Materials Science*, vol. 55, pp. 245–254, 2012.

[109] C. A. Gandin, G. Guillemot, B. Appolaire, and N. T. Niane, "Boundary layer correlation for dendrite tip growth with fluid flow," *Materials Science and Engineering A*, vol. 342, no. 1-2, pp. 44–50, 2003.

[110] M. E. Glicksman and S.-C. Huang, "Convection and diffusion effects during dendritic solidification," in *17th Aerospace Sciences Meeting*, p. 29, 1979.

[111] M. E. Glicksman, S. R. Coriell, and G. B. McFadden, "Interaction of flows with the crystal-melt interface," *Ann. Rev. Fluid Mech.*, vol. 18, pp. 307–333, 1986.

[112] V. T. Witusiewicz, L. Sturz, U. Hecht, and S. Rex, "Thermodynamic description and unidirectional solidification of eutectic organic alloys: III. Binary systems neopentylglycol-(D)camphor and amino-methyl-propanediol-(D)camphor," *Acta Materialia*, vol. 52, no. 19, pp. 5519–5527, 2004.

[113] V. Witusiewicz, L. Sturz, U. Hecht, and S. Rex, "Lamellar coupled growth in the neopentylglycol-(D)camphor eutectic," *Journal of Crystal Growth*, vol. 386, pp. 69–75, 1 2014.

[114] MATLAB R2020b, "Image Coordinate Systems," 2021.

[115] N. Otsu, "A Threshold Selection Method from Gray-Level Histograms," *IEEE Transactions on Systems, Man, and Cybernetics*, vol. 9, no. 1, pp. 62 – 66, 1979.

[116] Z. Jun and H. Jinglu, "Image segmentation based on 2D Otsu method with histogram analysis," *Proceedings - International Conference on Computer Science and Software Engineering, CSSE 2008*, vol. 6, no. 1, pp. 105–108, 2008.

[117] W. U. Mirihanage, K. V. Falch, D. Casari, S. McFadden, D. J. Browne, I. Snigireva, A. Snigirev, Y. J. Li, and R. H. Mathiesen, "Non-steady 3D dendrite tip growth under diffusive and weakly convective conditions," *Materialia*, vol. 5, no. November 2018, 2019.

[118] R. Trivedi and W. Kurz, "Dendritic Growth," *International Materials Reviews*, vol. 39, no. 2, pp. 49–73, 1994.

[119] J. D. Hunt and S.-Z. Lu, "Numerical modeling of cellular/dendritic array growth: spacing and structure predictions," *Metallurgical and Materials Transactions A*, vol. 27, no. 3, pp. 611–623, 1996.

[120] M. H. Burden and J. D. Hunt, "Cellular and dendritic growth. II," *Journal of Crystal Growth*, vol. 22, no. 2, pp. 109–116, 1974.

[121] J. Lipton, M. E. Glicksman, and W. Kurz, "Equiaxed dendrite growth in alloys at small supercooling," *Metallurgical Transactions A*, vol. 18, no. 2, pp. 341–345, 1987.

[122] W. Kurz, B. Giovanola, and R. Trivedi, "Theory of microstructural development during rapid solidification," *Acta Metallurgica*, vol. 34, no. 5, pp. 823–830, 1986.

[123] M. Wu, M. Stefan-Kharicha, A. Kharicha, and A. Ludwig, "Flow-solidification interaction: A numerical study on solidification of NH4Cl – 70 wt.%H2O solution

in a water-cooled mould with a large sample thickness," *International Journal of Heat and Mass Transfer*, vol. 164, p. 120566, 2021.

[124] T. Takaki, M. Ohno, Y. Shibuta, S. Sakane, T. Shimokawabe, and T. Aoki, "Two-dimensional phase-field study of competitive grain growth during directional solidification of polycrystalline binary alloy," *Journal of Crystal Growth*, vol. 442, pp. 14–24, 2016.

[125] T. Takaki, S. Sakane, M. Ohno, Y. Shibuta, T. Shimokawabe, and T. Aoki, "Large-scale phase-field studies of three-dimensional dendrite competitive growth at the converging grain boundary during directional solidification of a bicrystal binary alloy," *ISIJ International*, vol. 56, no. 8, pp. 1427–1435, 2016.

[126] T. Takaki, S. Sakane, M. Ohno, Y. Shibuta, T. Aoki, and C. A. Gandin, "Competitive grain growth during directional solidification of a polycrystalline binary alloy: Three-dimensional large-scale phase-field study," *Materialia*, vol. 1, pp. 104–113, 9 2018.

[127] D. Tourret and A. Karma, "Growth competition of columnar dendritic grains: A phase-field study," *Acta Materialia*, 2015.

[128] D. Tourret, Y. Song, A. J. Clarke, and A. Karma, "Grain growth competition during thin-sample directional solidification of dendritic microstructures: A phase-field study," *Acta Materialia*, vol. 122, pp. 220–235, 2017.

[129] M. Rappaz and C. A. Gandin, "Probabilistic modelling of microstructure formation in solidification processes," *Acta Metallurgica Et Materialia*, vol. 41, no. 2, pp. 345–360, 1993.

[130] M. Rappaz, C.-A. Gandin, J.-L. Desbiolles, and P. Thevoz, "Prediction of grain structure in various solidification processes," *Metallurgical and Materials Transactions A*, vol. 27A, no. March, pp. 695–705, 1996.

[131] H. Esaka, "PhD Thesis," tech. rep., Ecole Polytechnique Federale de Lausanne, Switzerland, 1986.

[132] J. D. Hunt, "Steady state columnar and equiaxed growth of dendrites and eutectic," *Materials Science and Engineering*, vol. 65, no. 1, pp. 75–83, 1984.

[133] D. R. Liu, N. Mangelinck-Noël, C. A. Gandin, G. Zimmermann, L. Sturz, H. Nguyen Thi, and B. Billia, "Structures in directionally solidified Al-7 wt.% Si alloys: Benchmark experiments under microgravity," *Acta Materialia*, vol. 64, pp. 253–265, 2014.

[134] Y. Z. Li, N. Mangelinck-Noël, G. Zimmermann, L. Sturz, and H. Nguyen-Thi, "Effect of solidification conditions and surface pores on the microstructure and columnar-to-equiaxed transition in solidification under microgravity," *Journal of Alloys and Compounds*, vol. 749, pp. 344–354, 2018.

[135] L. Sturz, M. Wu, G. Zimmermann, A. Ludwig, and M. Ahmadein, "Benchmark experiments and numerical modelling of the columnar-equiaxed dendritic growth in the transparent alloy Neopentylglycol-(d)Camphor," *IOP Conference Series: Materials Science and Engineering*, vol. 84, p. 012086, 6 2015.

[136] G. Zimmermann, L. Sturz, Y. Z. Li, H. Nguyen-Thi, N. Mangelinck-Noël, R. Fleurisson, G. Guillemot, C.-A. Gandin, S. McFadden, R. P. Mooney, P. W. Voorhees, A. Roosz, C. Beckermann, A. Karma, N. Warnken, E. Perchaat, G. U. Grun, M. Grohn, I. Poitrault, D. Toth, and W. Sillekens, "Columnar and equiaxed solidification within the framework of the ESA MAP project CETSOL," in *Solidification and Gravity VII.* (A. Roósz, Z. Veres, M. Svéda, and G. Karacs, eds.), (Miskolc-Lillafüred, Ungarn), pp. 17–26, Hal, 2018.

[137] Y. Mori, H. Harada, T. Yokokawa, T. Kobayashi, and S. Suzuki, "Directionally-solidified dendrite morphology with eight secondary arms in an FCC ordered phase alloy," *Journal of Crystal Growth*, vol. 500, no. August, pp. 15–22, 2018.

[138] J. Chen, U. Dahlborg, C. M. Bao, M. Calvo-Dahlborg, and H. Henein, "Microstructure evolution of atomized Al-0.61 wt pct Fe and Al-1.90 wt pct Fe alloys," *Metallurgical and Materials Transactions B: Process Metallurgy and Materials Processing Science*, vol. 42, no. 3, pp. 557–567, 2011.

[139] T. Haxhimali, A. Karma, F. Gonzales, and M. Rappaz, "Orientation selection in dendritic evolution," *Nature Materials*, vol. 5, no. 8, pp. 660–664, 2006.

[140] F. Gonzales and M. Rappaz, "Dendrite growth directions in aluminum-zinc alloys," *Metallurgical and Materials Transactions A: Physical Metallurgy and Materials Science*, vol. 37, no. 9, pp. 2797–2806, 2006.

[141] M. Becker, J. A. Dantzig, M. Kolbe, S. T. Wiese, and F. Kargl, "Dendrite orientation transition in Al–Ge alloys," *Acta Materialia*, vol. 165, pp. 666–677, 2019.

[142] M. Bedel, G. Reinhart, C. A. Gandin, A. A. Bogno, H. Nguyen-Thi, and H. Henein, "Evolution of the dendritic morphology with the solidification velocity in rapidly solidified Al-4.5wt.%Cu droplets," *IOP Conference Series: Materials Science and Engineering*, vol. 84, no. 1, 2015.

[143] M. Bedel, G. Reinhart, A.-A. Bogno, C.-A. Gandin, S. Jacomet, E. Boller, H. Nguyen-Thi, and H. Henein, "Characterization of dendrite morphologies in rapidly solidified Al–4.5wt.%Cu droplets," *Acta Materialia*, vol. 89, pp. 234–246, 2015.

[144] M. Bedel, G. Reinhart, A. A. Bogno, H. Nguyen-Thi, E. Boller, C. A. Gandin, and H. Henein, "Dendrite growth morphologies in rapidly solidified Al-4.5wt.%Cu droplets," *IOP Conference Series: Materials Science and Engineering*, vol. 117, no. 1, 2016.

[145] H. Henein, A. A. Bogno, W. Hearn, and J. Valloton, "Metastable Dendrite Morphologies in Aluminum Alloys," *Journal of Phase Equilibria and Diffusion*, vol. 41, no. 6, pp. 784–792, 2020.

[146] M. Rappaz and E. Blank, "Simulation of oriented dendritic microstructures using the concept of dendritic lattice," *Journal of Crystal Growth*, vol. 74, no. 1, pp. 67–76, 1986.

[147] H. Esaka, W. Kurz, and R. Trivedi, "Evolution of primary dendrite spacing in succinonitrile acetone alloys," *Solidification Processing, The Institute of Metals, London*, vol. 1, pp. 198–201, 1987.

[148] C. A. Gandin, M. Eshelman, and R. Trivedi, "Orientation dependence of primary dendrite spacing," *Metallurgical and Materials Transactions A: Physical Metallurgy and Materials Science*, vol. 27, no. 9, pp. 2727–2739, 1996.

[149] A. Wagner, B. A. Shollock, and M. McLean, "Grain structure development in directional solidification of nickel-base superalloys," *Materials Science and Engineering A*, vol. 374, no. 1-2, pp. 270–279, 2004.

[150] N. D'souza, M. G. Ardakani, M. McLean, and B. A. Shollock, "Directional and single-crystal solidification of Ni-base superalloys: Part I. The role of curved isotherms on grain selection," *Metallurgical and Materials Transactions A: Physical Metallurgy and Materials Science*, vol. 31, no. 11, pp. 2877–2886, 2000.

[151] H. Yu, J. Li, X. Lin, L. Wang, and W. Huang, "Anomalous overgrowth of converging dendrites during directional solidification," *Journal of Crystal Growth*, vol. 402, pp. 210–214, 2014.

[152] Y. Z. Zhou, A. Volek, and N. R. Green, "Mechanism of competitive grain growth in directional solidification of a nickel-base superalloy," *Acta Materialia*, vol. 56, no. 11, pp. 2631–2637, 2008.

[153] X. B. Meng, Q. Lu, X. L. Zhang, J. G. Li, Z. Q. Chen, Y. H. Wang, Y. Z. Zhou, T. Jin, X. F. Sun, and Z. Q. Hu, "Mechanism of competitive growth during directional solidification of a nickel-base superalloy in a three-dimensional reference frame," *Acta Materialia*, vol. 60, pp. 3965–3975, 2012.

[154] T. Takaki, S. Sakane, M. Ohno, and Y. Shibuta, "Competitive growth during directional solidification of a binary alloy with natural convection: Two–dimensional phase–field study," *Modelling Simul. Mater. Sci. Eng.*, 2019.

[155] J. Lee, M. Ohno, Y. Shibuta, and T. Takaki, "Uniquely selected primary dendrite arm spacing during competitive growth of columnar grains in Al–Cu alloy," *Journal of Crystal Growth*, vol. 558, no. January, p. 126014, 2021.

[156] M. E. Glicksman, R. J. Schaefer, and J. D. Ayers, "Dendritic growth-A test of theory," *Metallurgical Transactions A*, vol. 7, no. 11, pp. 1747–1759, 1976.

Appendix A

Solidification processing conditions leading to the Columnar-to-Equiaxed Transition

Prior to work carried out in Chapter 2, a series of directional solidification tests were conducted to investigate the conditions of growth rate and temperature gradient leading to the Columnar-to-Equiaxed Transition. However, due to accidental damage to the sapphire crucible, a new sapphire crucible was obtained and positions of thermocouples on the wall of the sapphire crucible were modified to include temperature measurements at two vertical positions in the baffle zone.

For the present work, figure A.1 shows a technical illustration of the experimental setup. Temperature in the adiabatic baffle zone was recorded at a single vertical position. The vertical temperature gradient was measured by, $G = (T_{HB} - T_A)/1.7$ K/cm, while cooling rate was obtained from the average cooling rates of $\dot{T}_{HB}$ and $\dot{T}_A$. The same experimental procedure detailed in section 2.2.3 was used. A total of 23 tests were conducted at different cooling rates and temperature gradients. Hence, different isotherm speeds were investigated. The growth rate was measured with the front-tracker decribed in Chapter 2. The textures were identified from in-situ optical video footage of the solidification process, and categorised as either; (a) fully columnar, (b) mixed columnar and equiaxed or (c) fully equiaxed (see figure A.2. In determining the different growth textures, equiaxed grains reaching elongation factors greater than

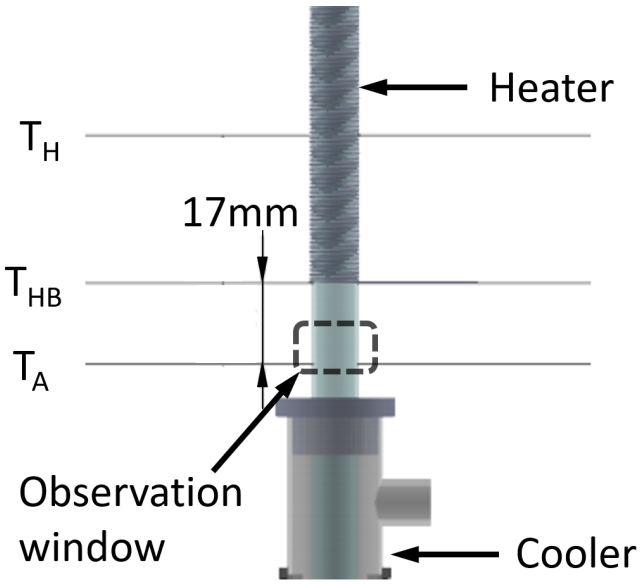

Figure A.1: Technical illustration of baffle zone.

two, were deemed columnar.

- A growth rate vs temperature gradient map has been developed identifying conditions for fully columnar, mixed columnar & equiaxed, and fully equiaxed growth.
- Experimental results can be used for validation of numerical models of solidification for CET prediction.

Table A.1: Solidification processing parameters (based on measurements at T_{HB} and T_A)

Cooling Rate (K/min)	Temperature Gradient (K/cm)	Growth Rate ($\mu m/s$)	Texture (-)
0.41	9.17±0.34	7.52±0.30	E
0.78	9.17±0.34	14.17±0.56	E
1.51	9.23±0.42	27.20±1.50	E
0.39	11.89±0.45	5.44±0.21	E
0.77	12.31±0.33	10.43±0.30	E
1.42	12.32±0.39	19.23±0.73	E
0.43	15.31±0.38	4.73±0.15	E
0.81	15.35±0.40	8.80±0.30	E
1.35	15.63±0.45	14.44±0.49	E
0.66	18.48±0.34	5.95±0.17	E
1.51	18.68±0.27	13.51±0.24	E
0.35	21.29±0.35	2.74±0.05	E
0.68	21.17±0.56	5.37±0.14	E
0.18	8.73±0.40	3.41±0.17	M
0.17	12.02±0.46	2.38±0.10	M
0.44	18.48±0.35	3.95±0.08	M
0.08	8.84±0.39	1.55±0.07	C
0.08	12.26±0.38	1.11±0.04	C
0.05	15.12±0.41	0.55±0.02	C
0.15	15.06±0.43	1.69±0.06	C
0.08	18.14±0.34	0.70±0.02	C
0.17	18.48±0.28	1.57±0.03	C
0.15	20.85±0.42	1.21±0.03	C

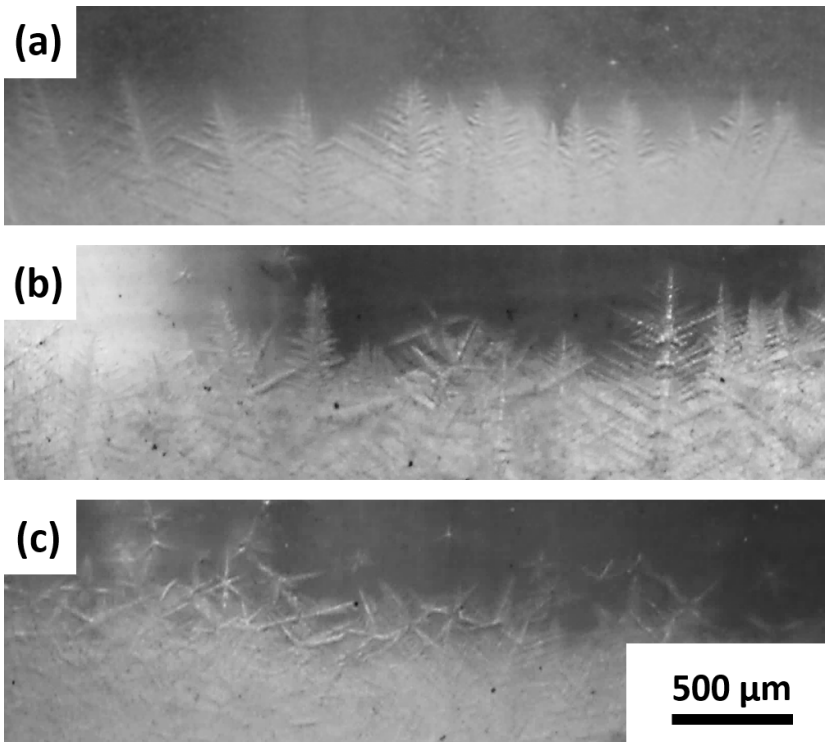

Figure A.2: Cropped optical micrographs showing examples of (a) fully columnar (b) mixed columnar and equiaxed, and (c) fully equiaxed textures.

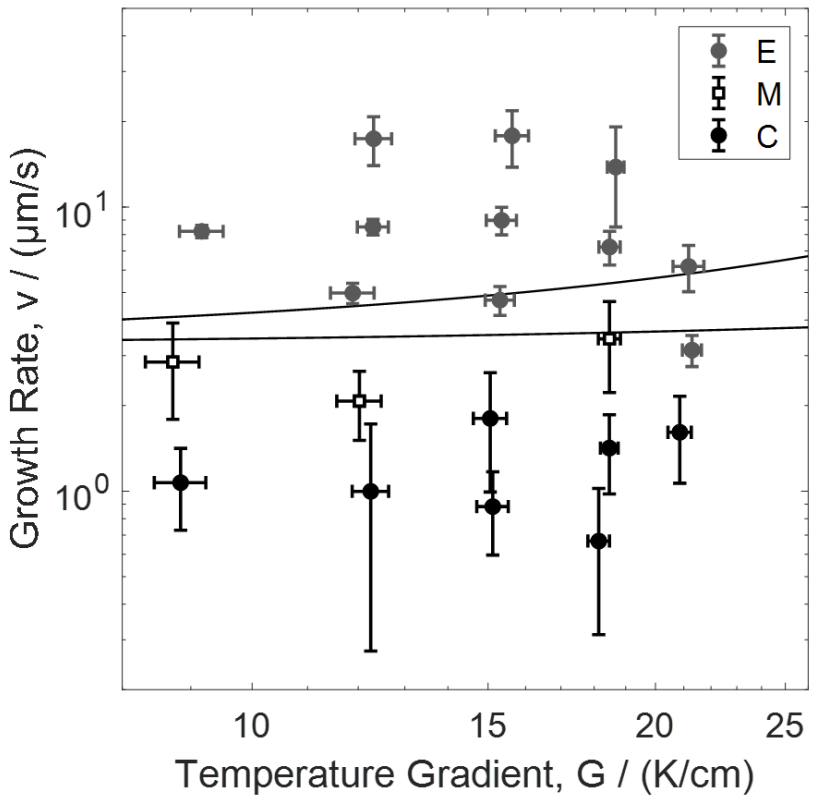

Figure A.3: Growth rate and temperature gradient map showing results of fully equiaxed (E), mixed columnar and equiaxed (M), and fully columnar (C), with hunt criterion (black line).